On the Origin of Cold Molecular Gas In Giant Elliptical Galaxies

by

Faerlin Pulido

A thesis
presented to the University of Waterloo
in fulfillment of the
thesis requirement for the degree of
Master of Science
in
Physics

Waterloo, Ontario, Canada, 2017

I hereby declare that I am the sole author of this thesis. This is a true copy of the thesis, including any required final revisions, as accepted by my examiners.

I understand that my thesis may be made electronically available to the public.

Abstract

We present an analysis of 55 giant elliptical galaxies residing in the centre of clusters and groups to investigate the origin of H_2 molecular gas centrally located in these galaxies. Using *Chandra* X-ray data and IRAM 30m CO line surveys, we report a sharp threshold for the detection of molecular gas when the central cooling time or entropy index of the hot atmosphere falls below $\sim$1 Gyr or $\sim$35 keV cm^2, respectively. This shows a direct relationship between the molecular gas and the local state of the intracluster gas, which is found to always exceed the amount of detected molecular gas within the field of view of the telescope. These findings point to thermal instability in the hot atmosphere as the origin of the observed molecular gas. We compare our results to the predictions of precipitation models where thermal instabilities are triggered when the minimum of the cooling to free-fall time ratio (t_{cool}/t_{ff}) is less than some constant. For our sample, we find this constant to be $\sim$25. We find these models to be inconsistent with observations as the effects of continual AGN outbursts on the ICM do not lead to the large fluctuations in central gas density and cooling time implied in these models. Consequently, we find that the t_{cool} threshold forecasts CO emission more reliably than the $\min(t_{cool}/t_{ff})$ criterion as applied in this study. We conclude with a discussion of the stimulated feedback model that includes the important physics of thermal instability and the uplift of low entropy gas by buoyantly rising X-ray cavities supported by a growing number of ALMA observations.

Acknowledgements

I would like to thank my supervisor Brian McNamara for his guidance, patience and for taking the chance to accept a student without any background in astronomy. His advice on readings and work ethic were instrumental to my maturity as an academic and a more responsible individual. I would also like to thank my committee members (James Taylor, Niayesh Afshordi, and Mike Hudson) for taking time out of their busy schedule to listen to my presentations. I am grateful also to Alastair Edge, Helen Russel, and Paul Nulsen for providing the data and tools for this thesis such as CO data, X-ray reduction scripts, mass models, insightful discussion and constructive criticisms on my writing to name just a few. Quoting Newton, "If I have seen further it is by standing on the shoulders of Giants".

Just as important, I would like to thank my office mates: Adrian Vantyghem, for helping me considerably with technical issues and for having the patience to answer all of my questions; Mike Hogan for introducing me to radio astronomy and for the opportunity to work on the mass models from which I learned a lot, and Iurii Babyk for his humor.

Finally, I would like to thank my love ones: my parents who have supported me in numerous ways for which I sometimes take for granted, and Lucy who is always there for me and for inspiring me to be a better person. Thank you God, for the strength to persevere.

Table of Contents

List of Tables vii

List of Figures viii

1 Introduction 1

1.1 Clusters of Galaxies . . . 4

1.1.1 Basic Properties . . . 4

1.1.2 Cluster Scaling Relations . . . 5

1.1.3 Intracluster Medium . . . 5

1.1.4 Cooling Flow Problem . . . 7

1.1.5 Heating Mechanisms . . . 8

1.2 Origin of Cold Gas . . . 10

1.2.1 Thermal Instability . . . 10

1.2.2 Precipitation Models . . . 11

1.2.3 Uplift Models . . . 14

1.3 Objectives of this Thesis . . . 16

2 Analysis 17

2.1 Sample . . . 17

2.2 Cluster X-ray Properties . . . 19

2.2.1 Data Reduction and Spectra Extraction . . . 19

2.2.2 Spectral Fitting and Modeling the ICM . . . 20
2.2.3 Gas Properties of the ICM . . . 21
2.2.4 Deprojection Algorithm . . . 21
2.3 Molecular Gas Mass . . . 23
2.4 Mass Profiles . . . 25
2.4.1 Mass Profile Model . . . 25
2.4.2 Inferred Velocity Dispersion From 2MASS Isophotal Magnitudes . . . 27
2.4.3 Spectral Fitting and Mass Profile . . . 28
2.5 Cavity Energetics . . . 28
2.6 Star Formation Rate . . . 30

3 Discussion **31**
3.1 Cooling Time and Molecular Gas Mass . . . 31
3.2 Entropy and Molecular Gas Mass . . . 35
3.3 Thermal Instability In the Hot Atmosphere . . . 36
3.4 Ratio of Cooling Time Over Free-Fall Time and Molecular Gas Mass . . . 38
3.5 The Effect of AGN Feedback On ICM Properties . . . 41
3.6 AGN Feedback and Molecular Gas . . . 45
3.7 Cooling and Uplift Models . . . 47

4 Conclusion **51**
4.1 Summary . . . 51
4.2 Future Work . . . 52

Bibliography **53**

APPENDICES **71**

A Tables **72**

B Other Contributions **80**

List of Tables

2.1 ALMA Observations Compared with IRAM Results 24

A.1 Data Sample 72
A.2 Molecular Gas Mass Compilation 74
A.3 X-ray Observation Properties 76
A.4 Mass Parameters 77
A.5 Cavity Power and Star Formation Rate 79

List of Figures

1.1 Chandra X-ray images showing AGN and ICM interaction 9
1.2 Cooling Time and Entropy Thresholds 12
1.3 Molecular Gas Trailing X-ray Cavities 15
1.4 Low velocity dispersion of molecular gas in PKS0745-191 15

2.1 Molecular gas mass vs. Hα luminosity 18
2.2 Mass Profile of Hydra-A 26

3.1 Cooling Time Threshold for CO Emission 32
3.2 Central Cooling Time vs. Mean Radius of Innermost Region 33
3.3 Histogram of Cooling Times at 10 kpc and Molecular Gas Mass vs. Redshift 34
3.4 Molecular Gas Mass and X-ray Properties 35
3.5 Molecular Gas Mass vs. Hot Gas Mass 37
3.6 Cooling to Free-fall Time Ratio 39
3.7 Cavity power vs. Cooling time and entropy at 10 kpc 41
3.8 Cooling Time and Gas Density Profiles 42
3.9 Comparison between simulated and observed gas density profiles 43
3.10 Cavity power vs. X-ray luminosity 44
3.11 Molecular gas mass vs. AGN Mechanical Power 46
3.12 Molecular Gas Mass vs. Star Formation Rate 47
3.13 Entropy Profiles of Cool Core Clusters 50

Chapter 1

Introduction

Understanding the origin and fate of molecular gas in elliptical galaxies (ETGs) is vital to our understanding of star formation, which is a major factor in driving the evolution of galaxies. Large galaxy surveys such as the Sloan Digital Sky Survey (SDSS) (York et al., 2000) firmly established the bimodality in the color distribution of local galaxies which can be approximated as the sum of two Gaussians representing the so-called "blue cloud" and "red sequence" (Baldry et al., 2004). The blue cloud generally consists of star-forming spiral galaxies while the red sequence is mostly made up of non-star-forming elliptical galaxies (Strateva et al., 2001). Several studies have explained this bi-modality as a result of the rapid transition of galaxies from the blue cloud to the red sequence attributed to an abrupt cessation of star formation (Baldry et al., 2004; Faber et al., 2007; Thomas et al., 2005). Star forming regions in galaxies have been observed to correlate precisely with regions of abundant molecular H_2 (Leroy et al., 2008), and the lack of star formation is generally believed to be largely due to the lack of its primary fuel, molecular gas. Thus, the story of galaxy evolution from the blue cloud to red sequence is, to a large degree, a story of what happened to the molecular gas in galaxies.

Among the largest reservoirs of molecular gas are found in the most massive elliptical galaxies known. These giant ellipticals, known as brightest cluster galaxies (BCGs), occupy a unique position at the center of the gravitational potential well of galaxy clusters. BCGs situated in clusters with atmospheres that have central cooling times significantly less than the Hubble time would be expected to accumulate cold gas in a process called "cooling flow" (Fabian, 1994). Several early studies searched for molecular gas in cluster cooling flows resulting in H_2 upper limits of $\sim 10^{8-10}$ $M_\odot$ (Bregman and Hogg, 1988; Grabelsky and Ulmer, 1990; McNamara and Jaffe, 1994; O'Dea et al., 1994) and one detection in NGC1275 of the Perseus cluster (Lazareff et al., 1989; Mirabel et al., 1989). Using the IRAM 30m

and JCMT 15m telescopes and a selection of newly discovered optically luminous systems found by the ROSAT ALL-Sky Survey (Crawford et al., 1999), a breakthrough came about in the detection of molecular gas in the central galaxy of sixteen (Edge, 2001) and four (Salomé and Combes, 2003) cooling flow clusters. Since the publication of those papers, a number of clusters with molecular gas have also been observed (e.g Edge priv.comm, 2016, Salomé et al., 2011). Although the reservoirs of molecular gas observed in BCGs are massive, they account for less than 10% of the mass expected from unsuppressed cooling (Edge and Frayer, 2003). Therefore, cooling must be regulated by heating processes, and observations show that radio-mechanical feedback from the active galactic nuclei (AGN) hosted by the BCG is the most plausible heating mechanism. In response to the cooling of the ICM, the AGN launches radio jets that inflate buoyantly rising cavities, which dissipate heat back to the surrounding atmosphere via sound waves and shocks resulting to a long-lived heating/cooling balance (see reviews McNamara and Nulsen, 2007a, 2012; Fabian, 2012). Essential to this balance is the potential role that accretion of molecular gas plays in the formation of the AGN feedback loop, as it directly connects the ICM with the AGN outburst responsible for quenching its cooling (Pizzolato and Soker, 2005; Gaspari et al., 2012). More recently, with the Atacama Large Millimeter Array (ALMA) interferometer, observations of molecular gas within BCGs now resolve their spatial and velocity structure revealing their clumpy distributions (McNamara et al., 2014; Russell et al., 2014; David et al., 2014; Russell et al., 2016a,b; Vantyghem et al., 2016). With a growing sample of objects observed with telescopes with higher sensitivity and resolution, the future prospect in understanding the nature of molecular gas in galaxies looks promising.

In this thesis, we investigate the origin of molecular gas in giant ellipticals centrally located in clusters of galaxies. Several studies have shown that cold gas in cluster cores is highly correlated with the properties of the intracluster medium (ICM). Systems with nebular emission and recent star formation have been preferentially detected with low central cooling time ($\lesssim 1$ Gyr) and entropy index ($\lesssim 30$ keV cm^2) (Cavagnolo et al., 2008; Rafferty et al., 2008; Voit and Donahue, 2015). While a convincing theoretical explanation for these thresholds remains elusive, a possibility that has recently been gaining support is thermal instability in the hot atmosphere that occurs when the cooling to free-fall time ratio (t_{cool}/t_{ff}) falls below $\sim$1 (Cowie et al., 1980; Nulsen, 1986; McCourt et al., 2012). Broadly referred to as "precipitation models", these models proposed that thermal instability is breached when $\min(t_{cool}/t_{ff}) \leq 10$ (McCourt et al., 2012; Gaspari et al., 2013; Singh and Sharma, 2015; Prasad et al., 2015). Alternatively, this threshold may lie in the range $\sim$4-20 (Voit and Donahue, 2015) or $\sim$1-20 (Li et al., 2015). These models predict the condensation of hot gas when $\min(t_{cool}/t_{ff})$ falls below a certain threshold where some of this cold gas sink toward the black hole fueling AGN feedback, while others might form

stars and molecular clouds (Pizzolato and Soker, 2005; Gaspari et al., 2012; Li et al., 2015). Motivated by recent ALMA observations of CO emissions (McNamara et al., 2014; Russell et al., 2014; David et al., 2014; Russell et al., 2016a,b; Vantyghem et al., 2016) revealing molecular gas that are either being lifted, or condensing, in the wakes of rising X-ray bubbles, McNamara et al. (2016) proposed an alternative model where low entropy gas becomes thermally unstable when it is lifted to an altitude where its cooling time is much shorter than its infall time, $t_{cool}/t_I \lesssim 1$.

Motivated by these considerations, we present an analysis of 55 giant elliptical galaxies situated in the cores of clusters and groups from which 33 are detected with molecular gas. We investigate the plausibility of thermal instability as the origin of cold molecular gas observed in cluster cores. Throughout this paper, we have assumed a standard ΛCDM cosmology with $\Omega_m = 0.3$, $\Omega_\Lambda = 0.7$, and $H_0 = 70$ km s^{-1} Mpc^{-1}.

1.1 Clusters of Galaxies

In the concordance model (ΛCDM) for cosmology, a rapid exponential expansion of space in the early universe amplified primordial quantum fluctuations from which the large scale structures of the cosmos we observe today originated. With baryonic matter following the gravitational potential of dark matter, regions of differing densities developed structures hierarchically leading to the formation of the *cosmic web*: a vast-foam like structure composed of sheets, walls, and filaments separated by immense voids. In the nodes of this cosmic web, virialised galaxy clusters constitute the largest objects observed.

This section reviews the key properties of galaxy clusters. Section 1.1.1 discusses the main components of clusters. Section 1.1.2 describes self-similar scaling relations that provides baseline expectations for various properties of a cluster. I then discuss the cluster hot atmosphere in Section 1.1.3. A brief discussion regarding the deficit of cold gas expected from classical cooling flow models is given in Section 1.1.4, and the heating mechanisms that alleviates the symptoms presented by the cooling flow problem in Section 1.1.5.

1.1.1 Basic Properties

Forming the largest gravitationally bound structures in the Universe, galaxy clusters have total masses ranging from 10^{14} to greater than 10^{15} $M_\odot$ and contain roughly hundreds of galaxies spread over a region of a few Mpc across. Velocity dispersion measurements of these galaxies imply mass that only accounts for roughly 3% of the mass needed to keep the galaxies gravitationally bound together. A single luminous galaxy with mass greater than 10^{12} $M_\odot$, called the brightest cluster galaxy (BCG), is often found in the minimum of the cluster potential.

Referred to as the intracluster medium (ICM) the space between the cluster galaxies is filled with hot, dilute plasma that accounts for roughly 13% of the total cluster mass. The mass of this hot atmosphere ranges from 10^{13} to 10^{14} $M_\odot$ and emits most of its energy in the X-ray at luminosities in the range $10^{43} - 10^{46}$ erg s^{-1}. X-ray emission from galaxy clusters were first detected via rocket and balloon-based detectors and then with the Uhuru X-ray satellite (Gursky et al., 1972). Since then, hundreds of galaxy clusters have been observed by a long line of satellites: *Einstein*, *ROSAT*, *ASCA*, *XMM-Newton*, and *Chandra* to name a few. The ICM is emitting X-rays that is thermal in origin with temperatures at $10^7 - 10^8$ K. The hot gas forms a hydrostatic atmosphere when the temperature and density distribution reflect the gravitating mass.

The bulk of the cluster mass budget is composed of dark matter. It accounts for 84% of the cluster total mass and non-baryonic in composition according to the Big Bang nucleosynthesis theory, which requires the fraction of baryonic matter to be roughly 10% of the total gravitating mass in the Universe.

1.1.2 Cluster Scaling Relations

Self-similar models for clusters refers to descriptions of cluster properties if cluster formation is driven entirely of dark matter, gravity, and dissipationless collapse from cosmological initial conditions in an expanding universe. These models provide baseline expectations for various properties of a cluster from which we can compare with observations. Starting with the self-similar assumption for the density profiles of dark matter and intracluster gas, the following relations are obtained (Voit, 2005):

$$\begin{aligned} &\rho \propto \frac{M}{r^3} \\ &T \propto \frac{M}{r} \\ &\rho_g \propto \rho \\ &M_g \propto M \\ &L_X \propto \rho_g M_g T^{1/2} \end{aligned} \qquad \Longrightarrow \qquad \begin{aligned} &T \propto M^{2/3}\rho^{1/3} \\ &M_g \propto T^{3/2}\rho^{-1/2} \\ &L_X \propto T^2\rho^{1/2} \end{aligned} \tag{1.1}$$

for dark matter density ρ, cluster mass M, scale radius r, characteristic temperature T, gas density ρ_g, gas mass M_g, and X-ray luminosity L_X.

1.1.3 Intracluster Medium

The hierarchical structure formation in the Universe suggests that in the evolution of the intracluster medium, 25% of the gas originated from the stars of the member galaxies while the remaining 75% is primordial intergalactic gas accreted by the cluster. The intracluster plasma consists primarily of hydrogen and helium that is almost entirely ionized (Mushotzky and Loewenstein, 1997). Heavier elements, at $\sim$1/3 of solar abundance, contribute roughly 1% of the total mass of the ICM. At virial temperatures of $10^7 - 10^8$ K, the intracluster gas is almost entirely ionized. Moreover, the temperature is consistent with measurements of galaxy velocities such that T $\propto \sigma_{\rm v}^2$ where $\sigma_{\rm v}$ is the line of sight galaxy velocity dispersion (Mushotzky et al., 1978).

The ICM radiates primarily in the X-rays. The dominant continuum emission mechanism is thermal bremsstrahlung (free-free) emission at X-ray wavelengths. Thermal bremsstrahlung emission is produced when a free electron is accelerated in the Coulomb field of an ion. Below temperatures of 3×10^7 K, X-ray emission from the hot gas is dominated by the recombination lines of iron, oxygen, silicon, and other elements. For example, two important discrete line emissions that significantly alter the shape of the X-ray spectrum are the Fe K and L lines at 6-7 keV and 1 keV, respectively. The total power radiated by the ICM is given by

$$\mathrm{L} = \int \mathrm{n}_e \mathrm{n}_H \Lambda(\mathrm{T,Z})\ \mathrm{dV} \tag{1.2}$$

where n_e and n_H are the electron and hydrogen densities and Λ(T,Z) is the cooling function, which incorporates the contribution of the important processes of X-ray emission mentioned above.

The ICM can be assumed to be in hydrostatic equilibrium. The sound crossing time in the hot atmosphere is $\sim 10^8$ yr for a typical cluster with virial radius of 1 Mpc and virial temperature of 10^8 K. This is significantly less than the age of the cluster, which can be estimated to be roughly the Hubble time. Since the sound-crossing time defines the time-scale on which deviations from the pressure equilibrium are evened out, the gas can be in hydrostatic equilibrium where the temperature and density distributions reflect the gravitational potential. In a spherically symmetric system, hydrostatic equilibrium is given by

$$\frac{1}{\rho_\mathrm{g}} \frac{\mathrm{dP}}{\mathrm{dR}} = -\frac{\mathrm{GM}(< \mathrm{R})}{\mathrm{R}^2} \tag{1.3}$$

for gas density ρ_g, pressure P, and mass M($<$ R) enclosed within the radius R of the intracluster gas. The gas pressure can be related to the gas density using the ideal gas law

$$\mathrm{P} = \mathrm{nk_B T} = \frac{\rho_\mathrm{g} \mathrm{k_B T}}{\mu \mathrm{m_H}} \tag{1.4}$$

where n is the number density of gas particles and μ is the average mass of gas particles in the units of protons. Under these assumptions, the gravitating cluster mass can be calculated using

$$\mathrm{M}(< \mathrm{r}) = -\frac{\mathrm{k_B T r}^2}{\mathrm{G}\mu \mathrm{m_p}} \left(\frac{\mathrm{d\ ln}\ \rho_\mathrm{g}}{\mathrm{dr}} + \frac{\mathrm{d\ ln}\ T}{\mathrm{dr}} \right) \tag{1.5}$$

That is, total cluster mass can be computed by measuring the radial profiles of temperature and gas density.

1.1.4 Cooling Flow Problem

The hot gas at the center of clusters are radiatively cooling in X-rays. Absent a heating mechanism to compensate this continual loss of energy, it is radiated on a timescale of

$$t_{cool} = \frac{E_{thermal}}{L_X} = \frac{3}{2}\frac{nk_BT}{n_e n_H \Lambda(T,Z)}$$

This is the thermal energy of the gas divided by the energy lost per unit volume. Within the central ∼100 kpc region, gas density rises from 0.01 to 0.1 cm^{-3}. At these densities, the cooling time in the central regions can drop below 1 Gyr. This is much less than the age of the cluster leading to a "cooling flow", where gas slowly flows inwards to maintain the central pressure as the energy is radiated away (Fabian, 1994). As the gas radiatively lose energy by cooling, its density increases to maintain pressure balance with the surrounding. This results to a slow inward flow of material as the overlying gas replenish the condensing gas at rates of 100-1000 $M_\odot$ yr^{-1}. Therefore, over the lifetime of the cluster, the central cooling region of galaxy clusters should be teeming with newly formed stars or harbor large reservoirs of cooled gas. However, observations in the optical and UV wavelengths reveal star formation rates of only 1-100 $M_\odot$ yr^{-1} (Johnstone et al., 1987). Similarly, evidence found for cooled gas in cluster cores fall orders of magnitude below the expected quantities. The search for cooled gas covered a broad range of temperatures:

- soft X-ray emission (Peterson et al., 2003).
- ionized gas at $10^{5.5}$ K (OVI in UV ; Bregman et al. (2006)).
- ionized gas at 10^4 K (Hα in optical ; Crawford et al. (1999)).
- neutral gas at 10^3 K (21 cm hydrogen line ; O'Dea et al. (1998)).
- warm ($1000-2500$ K) molecular hydrogen (NIR vibrational lines ; Edge et al. (2002)).
- cold ($20-40$ K) molecular gas (CO lines ; Edge (2001); Salomé and Combes (2003)).

Among these gas components, it was found that cold molecular gas, with masses of $10^9 - 10^{11}$ $M_\odot$ far outweighs all others. Nonetheless, observations of star formation and cooled gas did not find quantities anywhere near the levels predicted by unimpeded cooling flow. Therefore, there must be a heating source that is balancing the radiative losses of the intracluster gas. The most promising means of such a heating mechanism has emerged to be the central active galactic nucleus (AGN) residing in the cluster core.

1.1.5 Heating Mechanisms

The lack of evidence for the predicted levels of classical cooling flow in cluster cores suggests a source of heating to suppress the observed rates of ICM cooling. Any successful heating mechanism must be sufficient to offset the cooling flow losses, which are on average $10^{43} - 10^{44}$ erg s^{-1}. Several heating mechanisms such as mergers and supernova explosions may contribute to heating but have been found to be too feeble to balance cooling losses in general. Thermal conduction, the transfer of heat by collisions of particles from the hot outer to the cold inner regions, may be able to prevent radiative cooling for clusters with cooling time above 1 Gyr (Voigt and Fabian, 2004; Voit and Donahue, 2015). Thermal instability; however, cannot explain the large fraction of clusters with very short cooling times. Chandra and XMM-Newton observatories have shown that active galactic nucleus (AGN) residing at the center of galaxy clusters are pouring large quantities of energy into the hot atmosphere. In the standard picture, radio jets from the central AGN inflate buoyantly-rising cavities into X-ray atmosphere, which subsequently drive turbulence, weak shocks, and sound waves in the intracluster gas (see review McNamara and Nulsen, 2007a).

Figure 1.1 shows the interaction of the central AGN on the surrounding hot atmosphere of four systems. The AGNs in these systems operates under a radiatively inefficient feedback and is referred to as mechanical mode, emitting most of their energy kinetically in the form of radio jets, which inflates bubbles in the atmosphere. The kinetic power in the jets can be estimated from the work done inflating the cavities, which is the product of the volume of the cavity and the surrounding pressure divided by the age of cavity (refer to Section 2.5 for more details). Measured cavity power ranges from 10^{42} to 10^{46} erg s^{-1}, which has been found to scale roughly linearly with the luminosity of cluster cooling regions, suggesting the sufficiency of AGN output to balance ICM radiative cooling (Rafferty et al., 2006; Fabian, 2012). The duty cycle, which is the fraction of time that a system possess cavities inflated by its central AGN, has been observed to be at least 60-70% (Dunn and Fabian, 2006; Bîrzan et al., 2012). This suggests that atmospheres of cooling clusters are undergoing almost non-stop energy injection by the AGN.

While accretion from the hot phase is able to provide enough fuel on average to power low-luminosity radio jets (Allen et al., 2006), it is insufficient to power the most powerful jets (Rafferty et al., 2006; Hardcastle et al., 2007; McNamara et al., 2011). Instead, accretion from the cold phase can provide enough fuel for powerful outbursts (Pizzolato and Soker, 2005). Under this framework, the product of residual cooling of the ICM is connected with the energetic outburst of the AGN.

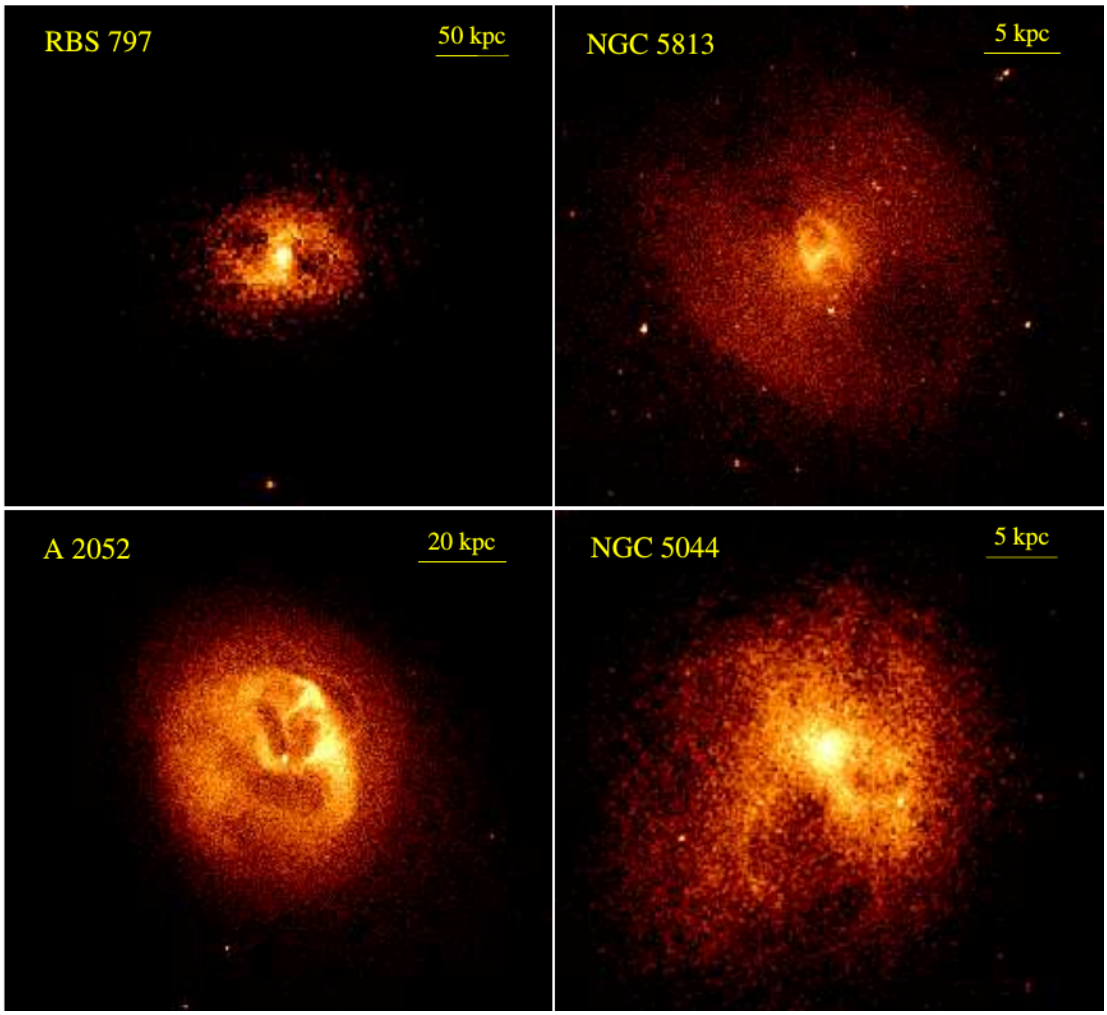

Figure 1.1: Chandra X-ray images showing the cavities on the intracluster atmosphere inflated by the central AGN. Image is adopted from Fabian (2012).

1.2 Origin of Cold Gas

1.2.1 Thermal Instability

In this section, we briefly describe the motions of gas parcels in a stratified atmosphere to begin our discussion of thermal instability as the origin of cold in the intracluster atmosphere.

In a hydrostatic atmosphere, take a parcel of gas at radius r away from the cluster center and denote its gas density as ρ(r). If this parcel is incompressible and is displaced to a lower height r − h where the ambient density is ρ(r - h), then it feels a buoyancy force equal to

$$\mathrm{F_{buoyancy}} = \mathrm{g}[\rho(\mathrm{r}-\mathrm{h}) - \rho(\mathrm{r})]\mathrm{V} \tag{1.6}$$

where V is the volume of the gas parcel. By Newton's second law (force is equals to mass times acceleration) applied on this parcel of gas and Taylor expansion to approximate the density difference on the right side of the equation, we obtain

$$\begin{aligned} \mathrm{F_{buoyancy}} &= \rho(\mathrm{r})V\frac{\mathrm{d}^2h}{\mathrm{dt}^2} \\ \frac{\mathrm{d}\rho}{\mathrm{dr}} &\approx \frac{\rho(\mathrm{r}-\mathrm{h}) - \rho(\mathrm{r})}{h} \end{aligned} \tag{1.7}$$

Using the equations in 1.7, equation 1.6 simplifies to a second order differential equation,

$$\frac{\mathrm{d}^2h}{\mathrm{dt}^2} - \frac{g}{\rho_0}\frac{\mathrm{d}\rho}{\mathrm{dr}}h = 0 \tag{1.8}$$

where the initial density ρ(r) was relabeled as ρ_0 assuming that the gas is incompressible. In hydrostatic equilibrium, pressure decreases with height with the rate of decrease being in proportion to density. In other words, $\mathrm{d}\rho/\mathrm{dr} < 0$ from which equation 1.8 has an oscillatory solution with frequency ν given by

$$\nu = \sqrt{-\frac{g}{\rho_0}\frac{\mathrm{d}\rho}{\mathrm{dz}}} \tag{1.9}$$

What this means physically is that when an incompressible parcel of gas is displaced downwards in a hydrostatic atmosphere, its density is lower than the surrounding and feels an upward force to maintain the pressure-gravity equilibrium. As it rises upward, its inertia causes is to go beyond the equilibrium level upon which it becomes surrounded by

lower density gas. It then feels a downward force, and the parcel of gas oscillates about the equilibrium level with frequency N, called the stratification or Brunt-Väisälä frequency.

The intracluster atmosphere can be assumed to be in a state of quasi-hydrostatic equilibrium. By the discussion above, density perturbations in the intracluster atmosphere should then oscillate about their equilibrium position, where density perturbation is zero, at the Brunt-Väisälä frequency. However, in contrast to the discussion above, gas in the intracluster atmosphere are compressible. A parcel of gas cools on a timescale of t_{cool} and free-falls on a timescale of t_{ff}. As it loses energy by cooling, its density increases and falls towards the center of the gravitational potential and seek a level from it can maintain the pressure-gravity balance with its surrounding. If t_{cool} is significantly less than the t_{ff}, it is cooling much faster than gravity is able to move it to its equilibrium level. By the time it reaches an equilibrium level corresponding to its density when it was just about to fall, it would have cooled significantly and raised its density higher requiring an equilibrium level deeper into the cluster's gravitational potential. On the contrary, when t_{cool} is significantly greater than t_{ff}, density perturbations in the hot atmosphere oscillate about their equilibrium at the Brunt-Väisälä frequency, and runaway cooling is expected not to occur.

As shown by the arguments of Nulsen (1986) and simulations of McCourt et al. (2012), thermal instability is guaranteed when the ratio of the cooling to free-fall time satisfies $t_{cool}/t_{ff} \lesssim 1$. When the thermal instability criterion is breached, density perturbations form overdense blobs that cools to low temperatures and decouple from the hot atmosphere, some of which may form stars or molecular gas (Cowie et al., 1980; Nulsen, 1986; Pizzolato and Soker, 2005).

1.2.2 Precipitation Models

Tracers of cold gas have been shown to be highly correlated with the properties of the surrounding hot atmosphere. In Figure 1.2, color gradient (an indicator of on-going star formation) and Hα luminosity (indicator of ionized gas at 10^4 K) are plotted against the central cooling time and entropy index of the surrounding hot gas, respectively. Systems with cold gas is preferentially observed in systems when the central cooling time falls below 1 Gyr (Rafferty et al., 2006) or when the central entropy index is less than 30 keV cm^2 (Cavagnolo et al., 2008). These thresholds show that cold gas is directly related to the local state of the surrounding hot gas suggesting that its origin involves the cooling of the hot atmosphere. This points to thermal instability as the origin of the cold gas.

A set of models called "precipitation models" have proposed that thermal instability in a cooling atmosphere occur when the cooling to free-fall time ratio is less than $\sim$10.

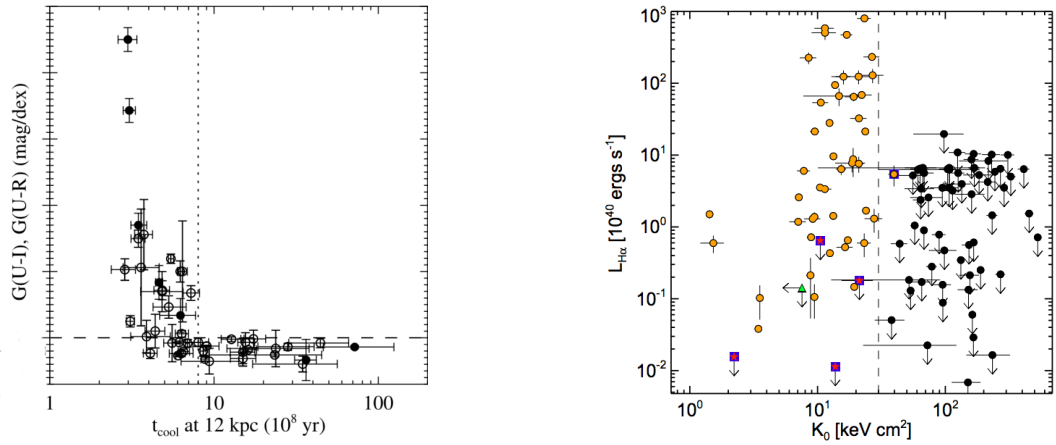

Figure 1.2: *Left*: Color gradient vs. cooling time at 12 kpc (Rafferty et al., 2006). *Right*: Hα luminosity vs. central entropy (Cavagnolo et al., 2008).

When $\min(t_{cool}/t_{ff}) \leq 10$, cold gas condenses and increases the accretion rate of the AGN. A large accretion rate causes the AGN to release strong jets and overheat the surrounding atmosphere driving $\min(t_{cool}/t_{ff})$ above 10. This heating phase suppresses the condensation of cold gas without eliminating the molecular gas completely. This slows down condensation of cold gas causing the accretion rate of the AGN to fall. Subsequently, the hot atmosphere slowly cools, restarting the cycle of cooling and heating. The interaction between the ICM and AGN described above exhibit a "hysteresis cycle".

In general, a system with hysteresis is characterized by two aspects: "lagging" and path-dependence (Morris and et al., 2017). Lagging refers to the delayed output of a system in response to its input. Path-dependence refers to the state of the system being independent of its input alone. That is, in order to determine the state of the system, we must also look at the history of the input (the path the input followed before it reached its current value). A brief example will illustrate these concepts more clearly. Consider a thermostat that controls a furnace. The furnace is either on or off. The thermostat allows us to set the temperature (input) and the thermostat will turn the furnace on or off (output). The thermostat is programmed such that when we set the target temperature to T_{target}, the thermostat turns the furnace on when the temperature drops below $T_{target} - 2°$ C and off when it exceeds $T_{target} + 2°$ C. Suppose we wish to maintain a comfortable room temperature of $T_{target} = 20°$ C. Then whenever the temperature of the room is $< 18°$ C or $> 22°$ C, the thermostat will turn furnace on or off, respectively, causing it to cycle between heating and cooling. There is a delay in changing the state of the furnace in response to the current temperature as the thermostat is only programmed to switch the furnace on or

off when it is outside the range of 18° C < T < 22° C. Suppose we know that the current temperature is 19° C. Will this be sufficient to determine whether the furnace is on or off? The temperature can arrive at 19° C following two different paths. If the temperature in the immediate past was <19° C, then the furnace must be on for the temperature to arrive at 19° C. However, if the temperature in the immediate past was >19° C, then the furnace must be off for the temperature to arrive at 19° C. That is, just knowing the instantaneous value of the input is not sufficient to predict the instantaneous output. In general, for a given input to a system with hysteresis, there is a spread of possible output.

In precipitation models, when the cooling of the ICM is suppressed (characterized by an increase in t_{cool}/t_{ff}), there is a delay of 1-2 Gyr before molecular gas is depleted by star formation ((Li et al., 2015)). Consequently, some systems with $\min(t_{cool}/t_{ff}) > 10$ are observed with cold gas. Moreover, at a given value of $\min(t_{cool}/t_{ff})$, it is not possible to determine whether the systems is in a cooling or heating phase. For example, the system could arrive at $\min(t_{cool}/t_{ff}) = 15$ through a heating phase as a result of a strong AGN outburst fueled by cold gas whose condensation was made possible when $\min(t_{cool}/t_{ff}) < 10$ in the immediate past. Alternatively, the system could arrive at $\min(t_{cool}/t_{ff}) = 15$ through a cooling phase after a strong AGN outburst that drove $\min(t_{cool}/t_{ff}) > 15$ in the immediate past.

As a result of the hysteresis cycle, instead of a sharp threshold, systems with cold gas is preferentially observed when the ratio of cooling to free-fall time is within a range of values: $4 \lesssim \min(t_{cool}/t_{ff}) \lesssim 20$ (Voit and Donahue, 2015) and $1 \lesssim \min(t_{cool}/t_{ff}) \lesssim 20$ (Li et al., 2015).

1.2.3 Uplift Models

In the previous sections, the observed correlation between cold gas in cluster cores and the properties of the surrounding hot atmosphere has pointed to rapid cooling of the hot intracluster gas as the origin of this cold gas. However, new observations of molecular gas in the center of galaxy clusters taken with the Atacama Large Millimeter Array (ALMA) suggest a more complex picture than rapid cooling in the hot atmosphere. Motivated by these observations, (McNamara et al., 2016) proposed the "stimulated feedback" model where cold gas condenses from lower entropy gas that is lifted outward from the cluster core by X-ray cavities. In this model, a parcel of gas is lifted to an environment where it is prone to thermal instability; that is, an altitude where its cooling time is shorter than its infall time, $t_{cool}/t_I \lesssim 1$.

ALMA observations at the cores of PKS0745-191 (Russell et al., 2016b) and 2A0335+096 (Vantyghem et al., 2016) reveal molecular gas distributed in long filaments. These filaments trail X-ray cavities as shown in Figure 1.3, suggesting an outflow of gas in the wakes of the cavities. In addition, the observed line-widths of these cold gas are narrow as shown in Figure 1.4, implying that these cold gas clouds have not had enough time to respond to their gravitational environments and instead formed largely in-situ (Russell et al., 2016b). Molecular gas with narrow observed line-widths appearing to trail X-ray cavities have also been observed in a growing sample of BCGS observed with ALMA (David et al., 2014; McNamara et al., 2014; Russell et al., 2014, 2016a; Tremblay et al., 2016). These observations are consistent with the molecular gas condensing in the wakes of X-ray cavities.

Alternatively, Voit et al. (2016) have proposed a model that divides the hot atmosphere into two regions in which thermal instability can ensure to produce cold gas. One region is situated in the center of the cluster and extends out to where the minimum of the cooling to free-fall ratio occurs. In this region, the entropy is constant and the hot atmosphere is prone to cooling instabilities. Outside this region, hot gas needs to be lifted to higher altitudes for thermal instabilities to occur, consistent with the stimulated feedback model.

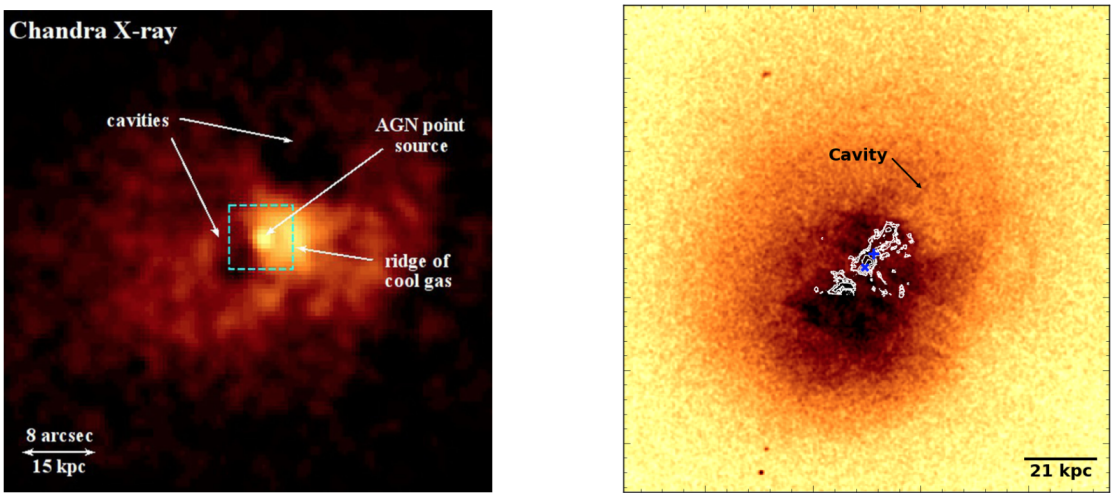

Figure 1.3: *Left*: Chandra X-ray image of the hot atmosphere of PKS07451-191. The box corresponds to the region covered by CO emission detecting molecular gas. *Right*: Chandra X-ray image of 2A0335+096 overlaid with white contours showing Hα emission, the ionized skins of molecular gas. Images are adopted from Russell et al. (2016b) and Vantyghem et al. (2016).

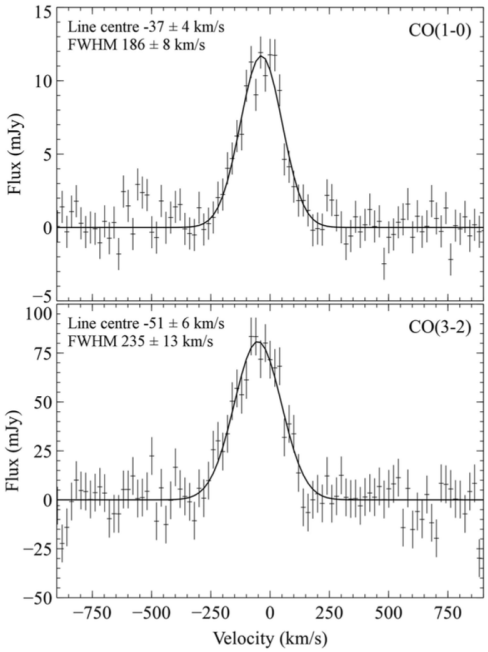

Figure 1.4: Total spectra of PKS0745-191 in CO(1-0) and CO(3-2) for 6 arcsec × 6 arcsec and 4 arcsec × 4 arcsec regions, respectively. Image is adopted from Russell et al. (2016b).

1.3 Objectives of this Thesis

In this thesis, we investigate the origin of molecular gas observed in giant elliptical galaxies centrally located in galaxy clusters. Previous studies have pointed to the cooling of the hot atmosphere as a plausible origin of cold gas by utilizing observational tracers of cold gas such as blue excess emission (indicator of star formation) and Hα emission (indicator of ionized gas at 10^4 K). However, as discussed in Section 1.1.4, the amount of cold molecular gas far outweighs all other gas components detected at temperatures below 10^6 K combined. Moreover, cold molecular gas can be related to important properties of a cluster core. Cold molecular gas is the primary fuel for star formation (McNamara et al., 2011; O'Dea et al., 2008). If accretion from the cold phase fuels the AGN in cluster cores, then cold molecular gas plays an important role in AGN outburst. Thus, a scenario in which cold molecular gas originates from the cooling of the hot atmosphere connects the cooling ICM and the AGN.

This thesis will investigate the plausibility of thermal instability and precipitation models using CO emission as an observational indicator for cold molecular gas. CO emission is the most accessible and widely used tracer for molecular gas. The bulk of the cold molecular gas is composed of H_2. Because it is a diatomic molecular with identical nuclei, it possesses no permanent dipole. Meaning that for all practical purposes, the cold molecular hydrogen is invisible to emission. Fortunately, cold molecular gas in these environment contains heavier elements at the level of a few atoms per 10^4 Hydrogen nucleon. The most abundant of these are Carbon and Oxygen, which combine to form CO under the conditions prevalent in molecular clouds. Unlike, molecular hydrogen, CO has a weak permanent dipole moment. It's ground rotational transition has a low excitation energy (5.53 K), which makes it easily excited even in cold molecular clouds.

We present an analysis of 55 giant elliptical galaxies situated in the cores of clusters and groups from which 33 are detected with molecular gas. Chapter 2 describes the sample and the steps taken in the analysis of Chandra X-ray data to measure properties of the ICM and derive cluster mass profiles. Literature sources of molecular gas mass estimates and other relevant quantities such star formation rates and cavity energetics are also discussed. Section 3.1 and 3.2 explores the cooling time and entropy threshold for the observation of molecular gas. Section 3.3 points to thermal instability as the consequence of these thresholds. Section 3.4 and 3.5 compares our results with predictions of precipitation models by examining the reliability of the $\min(t_{cool}/t_{ff})$ criterion for thermal instability and investigating the effects of AGN outburst on ICM properties. Section 3.6 discusses the connection between AGN feedback and molecular gas. We conclude with a discussion of uplift models motivated by ALMA observations in Section 3.7.

Chapter 2

Analysis

To investigate cooling of the hot atmosphere as a plausible origin of cold molecular gas in cluster cores, properties of the intracluster gas needs to be measured. Section 2.1 describes the data sample. Section 2.2 describes the steps taken to reduce and analyze Chandra X-ray data to measure properties of the X-ray emitting intracluster medium. Sources of molecular gas mass measurements and how raw CO line intensities are converted to mass are described in Section 2.3. To investigate the viability of precipitation models, free-fall times are measured from mass profiles as shown in Section 2.4. Finally, cavity energetics and star formation rates are taken from literature and described in Section 2.5 and 2.6, respectively.

2.1 Sample

The sample comprises of 55 central dominant galaxies for which we have obtained CO surveys from three sources: Edge (2001), Salomé and Combes (2003), and a number of clusters that were observed since the publication of those papers (Edge priv.comm, 2016). Samples in these publications were based on systems that have been observed for Hα emission or have substantial mass cooling rates. From these sources, the sample was constructed by choosing systems with available X-ray data from the *Chandra* Data Archive. Our final sample consists of 33 systems detected with CO emission and 22 without detection. The derived molecular gas mass of our sample is in the range $\sim 10^{8-11}$ $M_\odot$. It has been found that molecular gas mass observed in BCGs is correlated with Hα luminosity (Edge, 2001; Salomé and Combes, 2003), and is evident in our sample as shown in Figure 2.1. In the figure, note that all systems detected in CO are also shining in Hα. However, detection in

Hα does not guarantee detection in CO. The inferred molecular gas were derived mostly from the observed CO(1-0) transition with exception of three systems (A85, A1991 and Cygnus-A) derived from CO(2-1) and the upper limit for RXJ1347.5-1145 derived from CO(3-2). Cluster and BCG coordinates were taken from Hogan et al. (2015) and are summarized in Table A.1. Furthermore, properties of the X-ray observations are shown in Table A.3.

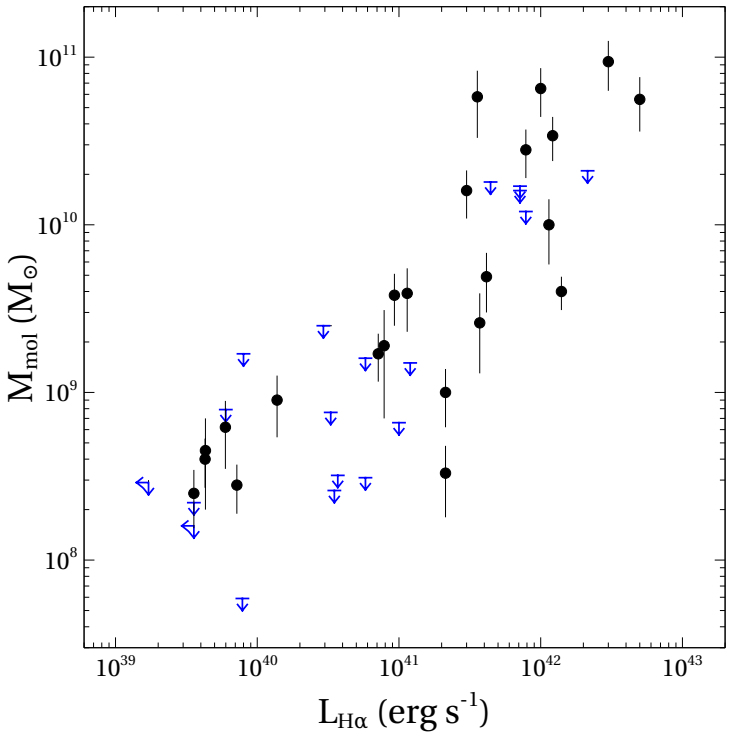

Figure 2.1: Molecular gas mass vs. Hα luminosity for our sample. Black symbols denote systems observed with CO emission while blue symbols denote upper limits.

2.2 Cluster X-ray Properties

We begin with the X-ray analysis of our sample in Section 2.2.1 by applying the data processing steps recommended by the Chandra X-ray Center (CXC). In Section 2.2.2 we use projected profiles to quantify gas temperature, electron density, metallicity, and flux. In Section 2.2.3 we compute pressure, entropy, luminosity, cooling time, and other derived quantities. To better describe the properties of the gas in the cluster centre, the same analysis is performed using deprojected profiles. A description of the algorithm used to deproject the extracted spectra is found in Section 2.2.4.

2.2.1 Data Reduction and Spectra Extraction

All of the clusters in our sample have been observed with the Chandra X-ray Observatory (CXO). In order to derive the X-ray properties required in our analysis, spectra must be extracted from these observations. As recommended by the CXC, the event data must be reprocessed before spectra are extracted to ensure that the newest software and calibration updates are applied. In this section, we outline the steps taken in our data reduction and spectra extraction pipeline.

All systems in our sample were observed with Chandra's Advanced CCD Imaging Spectrometer (ACIS) detector, and the event data for all observations were obtained from the Chandra Data Archive (CDA). Table A.3 summarizes these observations and their exposure times. Each observation was reprocessed with CIAO version 4.7. The CHANDRA_REPRO script automates the recommended data processing steps which entails applying the latest gain and charge transfer ineficiency correction to the level 1 event files. Photons detected with bad grades were then removed subsequently and the new level 2 event files were created.

Background light curves were extracted from the level 2 event files, and were filtered using the LC_CLEAN routine of M. Markevitch to identify and remove time intervals affected by flares. By following these steps, we obtained calibrated event 2 files ready for analysis. We need to account for the background in our observations. Blank-sky backgrounds were extracted using CALDB version 4.6.7 for each observation and reprocessed identically to the events files. The reprocessed blank-sky backgrounds were then normalized to match the 9.5-12.0 keV in the data set.

For each system, its calibrated event 2 files (and blank-sky backgrounds) were reprojected to match the position of the observation with the highest clean exposure time. An image for each system was produced by summing the event files of its observations in

the energy range 0.5 - 7.0 keV. This summed image for each system served two purposes. Firstly, it was used to identify point sources using WAVDETECT (Freeman et al., 2002), which were visually inspected and then excluded for further analysis. Secondly, it was used for creating concentric annuli for spectra extraction. Multiple definitions exist for the cluster centre. George et al. (2012) studied a sample of 129 massive groups and found that the massive galaxy closest to the X-ray centroid is the best tracer of dynamical centre out of the 8 tracers considered. With this in consideration, we have taken the location of the BCG as the centre for our concentric annuli. To ensure that the temperature could be measured accurately in deprojection, annuli were created with a minimum of ∼3000 projected counts (excluding background counts) with growing number of counts per annulus with increasing distance from the centre. For low-temperature systems, emission lines make their temperature easier to measure, so fewer source counts are required.

Once the concentric annuli have been created, spectra were extracted in CIAO, and were binned to a minimum of 30 counts per channel. For each spectrum, weighted redistribution matrix files (RMFs) and weighted auxiliary response files (ARFs) were created using the MKACISRMF and MKWARF, respectively. The RMF maps energy space into detector pulse height space. That is, it gives the probability that a photon detected in a given instrument channel has a given energy. The ARF gives the combined effective area and quantum efficiency as a function of energy averaged over time. Lastly, the loss of area as a result of chip gaps and excluding point sources need to be corrected. An exposure map for each observation was created using MKEXPMAP in CIAO. The mean value of this exposure map within the region of extraction was taken as the appropriate area correction, and was applied to the spectrum (and its background) by setting the AREASCAL keyword in its header. The product of the steps outlined above is a set of spectra ready for model fitting and analysis.

2.2.2 Spectral Fitting and Modeling the ICM

There are many publicly available codes that fit and model the X-ray emission of the intracluster medium. In this thesis, we use an absorbed single temperature PHABS(MEKAL) model (Mewe et al., 1985, 1986; Kaastra, 2015; Liedahl et al., 1995; Balucinska-Church and McCammon, 1994) in XSPEC version 12.8.2 (Arnaud, 1996) where we have set the solar abundances to the values of Anders and Grevesse (1989). The hydrogen column density N_H was frozen to the value of Kalberla et al. (2005) unless the best fit value was found to be significantly different. Running the fit on the PHABS(MEKAL) model yields fitted values for the gas temperature, metallicity, and normalization,

$$norm = \frac{10^{-14}}{4\pi \left(\mathrm{D_A}(1+\mathrm{z})\right)^2} \int \mathrm{n_e n_H}\ \mathrm{dV} \tag{2.1}$$

where z is redshift, $\mathrm{D_A}$ is the angular distance to the source, $\mathrm{n_e}$ and $\mathrm{n_H}$ are the electron and hydrogen number densities, respectively. Another gas property of interest is luminosity. Augmenting the previous model to PHABS*CFLUX(MEKAL) to integrate the unabsorbed thermal model between $0.1 - 100$ keV, we obtain the bolometric X-ray luminosity $\mathrm{L_X}$.

In summary, the following gas properties were measured: temperature kT, metallicity Z, normalization *norm*, and bolometric X-ray luminosity $\mathrm{L_X}$ from which we compute more gas properties relevant to our analysis in the next section.

2.2.3 Gas Properties of the ICM

We compute gas properties that will give us additional insight to the cluster environment using the quantities measured from the previous section. The electron density is computed from the normalization of the MEKAL model. Assuming hydrogen and helium mass fractions of $\mathrm{X} = 0.75$ and $\mathrm{Y} = 0.24$, we get $\mathrm{n_e} = 1.2\mathrm{n_H}$ (Anders and Grevesse, 1989). Taking $\mathrm{n_e}$ and $\mathrm{n_H}$ to be constant within an annulus of volume V, the electron density is computed from equation 2.1. Pressure and entropy index are computed as $\mathrm{P} = 2\mathrm{n_e kT}$ and $\mathrm{K} = \mathrm{kTn}^{-2/3}$, respectively. The cooling time of the ICM is computed as

$$\mathrm{t_{cool}} = \frac{3}{2}\frac{\mathrm{P}}{\mathrm{n_e n_H}\Lambda(\mathrm{Z,T})} = \frac{3}{2}\frac{\mathrm{PV}}{\mathrm{L_X}} \tag{2.2}$$

where L_X is the bolometric luminosity, V is the volume of the annulus, and Λ(T,Z) is the cooling function defined in Section 1.1.3.

2.2.4 Deprojection Algorithm

In order to relate the properties of the intracluster gas to the AGN feedback, we need a method for determining the core gas properties. In Section 2.2.2 we have extracted spectra from regions of cylindrical shells on the sky and assumed that temperatures, densities, and luminosities are constant in a shell. Since the emission at any point on the sky is a superposition of emission from all points along the line of sight through the cluster, the extracted spectra need to be "deprojected" to subtract off the superimposed contribution

from the outer layers of the cluster. Projected spectra skew the measured temperature, densities, and luminosities of the gas to higher values. That is, the extracted spectra need to be deprojected to determine the true radial profiles (Russell et al., 2008).

There are many publicly available codes that implement the deprojection routine – the most common one being PROJCT in XSPEC (Arnaud, 1996). However, PROJCT has been found to produce oscillating profiles that are not caused by any physical changes. In this thesis, we use a model-independent deprojection routine called DSDEPROJ described in the appendix of Sanders and Fabian (2007) and Russell et al. (2008).

We now provide a brief description of the method employed by DSDEPROJ to implement deprojection. Suppose we have N spectra (with their corresponding blank-sky background) extracted from N annuli. Let us denote the spectrum extracted from the i-th annulus as spectrum$[i]$ for $i = 1, 2, ..., N$. That is, spectrum$[i]$ holds information about the count rates of annulus i as a function of energy channel. We assume that the spectrum from the outermost annulus is uncontaminated. That is,

$$\text{spectrum}_{\text{deproj}}[N] = \text{spectrum}[N] \tag{2.3}$$

where $\text{spectrum}_{\text{deproj}}[i]$ denotes the deprojected i-th spectrum. To determine the deprojected spectrum of the next innermost annulus, we calculate the count rate per unit volume of the N-th annulus, scale it by the volume projected onto the next innermost shell, and subtract it from count rate of that annulus. That is,

$$\text{spectrum}_{\text{deproj}}[N-1] = \text{spectrum}[N-1] - \frac{V_{\text{proj}}[N, N-1]}{V_{\text{total}}[N]}\text{spectrum}_{\text{deproj}}[N] \tag{2.4}$$

where $V_{\text{total}}[i]$ is the total volume of i-th annulus and $V_{\text{proj}}[j, i]$ is the projected volume of the j-th annulus onto the i-th annulus. We move inwards shell by shell, subtracting each of the calculated contributions from outer shells. Starting from the outer annulus, we perform the deprojection as follows:

$$\begin{aligned} \text{spectrum}_{\text{deproj}}[N] &= \text{spectrum}[N] \\ \text{spectrum}_{\text{deproj}}[i] &= \text{spectrum}[i] - \sum_{j=i+1}^{N} \frac{V_{\text{proj}}[j, i]}{V_{\text{total}}[j]}\text{spectrum}_{\text{deproj}}[j] \end{aligned} \tag{2.5}$$

for $i = N-1, N-2, ..., 1$ in order. This produces a set of deprojected spectra that can then be fitted by models. Applying the same analysis discussed in Section 2.2.2 and 2.2.3, we obtain deprojected radial profiles for our spectra.

2.3 Molecular Gas Mass

All objects in our sample have been observed by the IRAM 30m telescope. Table A.2 summarizes the molecular gas mass inferred from these observations for our sample. The molecular gas mass for several objects in our sample were taken from Edge (2001) and Salomé and Combes (2003). Raw CO line intensities from observations made since those publications were also used to infer the molecular gas mass for a number of objects in our sample. Below, we describe how molecular gas masses were derived from these intensities and how the values taken from Edge (2001) were recomputed for a cosmology with $H_0 = 70$ km s^{-1} Mpc^{-1}.

Raw CO line intensity I_{CO} is detected in CO(1-0), CO(2-1), or CO(3-2) for 26 objects in our sample. Line intensity is determined from the measured antenna temperature and velocity width obtained by taking the FWHM of the CO spectrum fitted with a Gaussian. This is converted to integrated flux density $S_{CO}\Delta\nu$ using the following for IRAM (Edge, 2001)

$$S_{CO}\Delta\nu(\text{Jy km s}^{-1}) = [6.8(1+z)^{-1/2}\ \text{Jy K}^{-1}]I_{CO} \tag{2.6}$$

where I_{CO} is units of K km s^{-1} and z is redshift of the source. Integrated flux density in CO(2-1) or CO(3-2) is converted to an equivalent flux density in CO(1-2) using the flux ratios CO(2-1)/CO(1-0) = 3.2 (David et al., 2014) and CO(3-2)/CO(1-0) = 7.0 (Russell et al., 2016b). To translate integrated flux density in CO(1-0) directly to molecular gas mass, we use (Bolatto et al., 2013)

$$M_{mol} = 1.05\times10^4 \left(\frac{X_{CO}}{2\times10^{20}\frac{\text{cm}^{-2}}{\text{K km s}^{-1}}}\right)\frac{S_{CO}\Delta\nu D_L^2}{(1+z)} \tag{2.7}$$

where X_{CO} is the galactic CO-to-H_2 conversion factor, D_L is the luminosity distance in Mpc, and z is the redshift. Molecular gas mass is sensitive to the value of the galactic conversion factor and is not observed to be universal. A wide range of measurements yield $X_{CO} \approx 2-8$ cm^{-2} (K km s^{-1})$^{-1}$, with scatter greater than about a factor of two in which the uncertainties are related to the dynamical state of the molecular clouds and the environmental dependence of dust properties (Bolatto et al., 2013). We take the conservative approach and adopt $X_{CO} = 2\times10^{20}$ cm^{-2} (K km s^{-1})$^{-1}$ with $\pm30\%$ uncertainty as previous

studies of BCGs in cool core clusters have used (Edge, 2001; Salomé and Combes, 2003; Russell et al., 2014; McNamara et al., 2014; Russell et al., 2016b; Vantyghem et al., 2016). This X_{CO} value can be approximately applied down to metallicities of $\sim 0.5 Z_{\odot}$ (Bolatto et al., 2013). The mean metallicity measured for the innermost regions of the objects in our sample is 0.66 ± 0.38 $Z_{\odot}$.

The quantities in Edge (2001) were derived assuming a cosmology with $H_0 = 50$ km s^{-1} Mpc^{-1}. For consistency with our assumed cosmology, we recompute the molecular gas mass taken from Edge (2001) for a cosmology with $H_0 = 70$ km s^{-1} Mpc^{-1}. We translate molecular gas mass to integrated flux density $S_{CO}\Delta\nu$ using the following relation used in Edge (2001)

$$M_{mol} = (1.18 \times 10^4) S_{CO} \Delta\nu d^2_{Mpc} \tag{2.8}$$

where d_{Mpc} is the luminosity distance where $H_0 = 50$ km s^{-1} Mpc^{-1}. Molecular gas is then inferred from the flux density derived above using equation 2.7 where the luminosity distance is computed using our assumed cosmology. The resulting molecular gas masses is a factor of about 2.5 lower than the values cited in Edge (2001).

Recently, observations with the Atacama Large Millimeter Array (ALMA) have resolved the spatial and velocity structure of a small list of sample of BCGs in CO. The molecular gas mass derived from IRAM and ALMA observations are consistent as shown in Table 2.1.

Table 2.1: ALMA Observations Compared with IRAM Results

System	transition	IRAM $M_{\odot}$	ALMA $M_{\odot}$
2A0335+096	CO(1-0)	17 ± 5	11.3 ± 1.5
A1664	CO(1-0)	280 ± 90	110 ± 10
A1835	CO(1-0)	650 ± 210	490 ± 20
A2597	CO(1-0)	26 ± 13	-
	CO(2-1)	14 ± 5	18 ± 2
NGC5044	CO(1-0)	2.3 ± 0.8	-
	CO(2-1)	0.61 ± 0.2	0.51
PKS0745-191	CO(1-0)	40 ± 9	46 ± 9
Phoenix	CO(3-2)	-	210 ± 30

Notes: References for ALMA observations: 2A0335+096-Vantyghem et al. (2016), A1664-Russell et al. (2014) A1835-McNamara et al. (2014), A2597-Tremblay et al. (2016), NGC5044-David et al. (2014), PKS0745-191-Russell et al. (2016b), Phoenix-Russell et al. (2016a). Note that an alternative name for 2A0335+096 is RXCJ0338.6+0958.

2.4 Mass Profiles

In this section, we generate the mass profiles of our systems, which are then used to determine gravitational free-fall times and total cluster mass. We used the procedure outlined in Hogan et al. (2016) in which the authors used a small sample of galaxy clusters (A85,A496,A780,A2029,A2199) with deep Chandra observations and reliable ancillary tracers of their gravitating mass to develop a method for determining mass profiles that extend over a wide range of radii.

2.4.1 Mass Profile Model

An attractive feature of the procedure by Hogan et al. (2016) is that it produces a mass profile that is in good agreement with observed total cluster mass measurements and observed velocity dispersion measurements of the cluster core. Figure 2.2 shows the mass profile of A780 (Hydra-A) that is directly taken from Hogan et al. (2016). The mass inferred by Hamer et al. (2014) and from three velocity dispersions presented in the HyperLeda database agrees well with the derived mass profile at smaller radii. At larger radii, we see agreement with the total cluster mass measurement by Main et al. (2015) from X-ray analysis, as well as, with the weak-lensing derived mass profile of Okabe et al. (2015).

The agreement of the derived mass profile with observations at both small and large radii is primarily due to the two components of the gravitational potential used in this procedure: NFW potential and a cored isothermal potential,

$$\begin{aligned} \Phi_{\rm NFW} &= -4\pi {\rm G}\rho_0 {\rm r_s^2} \frac{\ln\left(1+{\rm r}/{\rm r_s}\right)}{{\rm r}/{\rm r_s}} \\ \Phi_{\rm ISO} &= \sigma^2 \ln\left(1+({\rm r}/{\rm r_I})^2\right) \end{aligned} \tag{2.9}$$

where ρ_0 is the characteristic density, $\rm r_s$ is the scale radius of the NFW potential, σ is the velocity dispersion, and $\rm r_I$ is the scale radius of the isothermal potential. The NFW profile (Navarro et al., 1997) has been found to capture the total gravitating mass of the cluster on large scales very accurately (e.g Main et al., 2015; Vikhlinin et al., 2006; Pointecouteau et al., 2005; Schmidt and Allen, 2007; Gitti et al., 2007). However, the NFW profile alone underestimates the inferred mass from the observed velocity dispersion of cluster cores (Fisher et al., 1995; Lauer et al., 2014). This is also evident in Figure 2.2 where the blue curve (mass predicted by NFW profile alone) underestimates the green curve (total mass profile). To account for this missing mass that is mainly due to the stellar mass of the

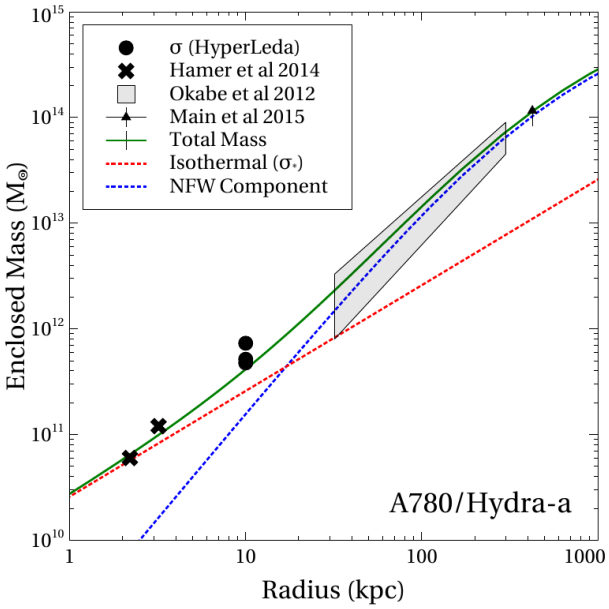

Figure 2.2: Mass profile of A780 taken directly from Hogan et al. (2016) derived using the procedure outlined in that paper. The green curve (derived mass profile) agrees well with measurements inferred by Hamer et al. (2014) and from HyperLeda for small radii, as well as, with total cluster mass measurements by Main et al. (2015) and Okabe et al. (2015) at larger radii.

central galaxy, Hogan et al. (2016) includes the cored isothermal component in their mass profile analysis.

This combined NFW and cored isothermal potential, dubbed ISONFWMASS, is implemented as an extension in a XSPEC package called CLMASS (Nulsen et al., 2010). X-ray spectra derived from *Chandra* data is fitted with this model, which assumes that the cluster is spherically symmetric and that the X-ray emitting gas is in hydrostatic equilibrium (refer to Section 2.2.1 for details on X-ray spectra extraction). To obtain a stable fit, Hogan et al. (2016) set the r_I parameter to an arbitrarily small but non-zero value and the σ parameter frozen to an inferred stellar velocity dispersion σ_* derived from 2-Micron All Sky Survey (2MASS) measurements as discussed in the next section.

2.4.2 Inferred Velocity Dispersion From 2MASS Isophotal Magnitudes

We estimate stellar velocity dispersions of central dominant galaxies from their 2MASS K-band (2.17 μm) magnitudes. Using near-infrared (NIR) observations for our purposes offer many advantages: insensitivity of mass-to-light ratios in the NIR to galaxy or stellar type (Bell and de Jong, 2001), independence of K-corrections in the K-band from galaxy type (Mannucci et al., 2001), and dust is much less of a problem in the NIR than in the optical (Maller et al., 2009). In brief, the NIR light is a good tracer of the total stellar mass in a galaxy.

To obtain a reliable measurement of the light within a certain radius, we use the 2MASS isophotal magnitude (m_{k20}) in the K-band within the isophotal radius (r_{k20}) defined as the apparent magnitude at which the surface brightness reaches 20 mag/sq.". We apply the following corrections to this apparent magnitude: galactic extinction (Schlegel et al., 1998), evolution and K-correction (Poggianti, 1997). We apply galactic extinction correction to take into account the absorption and scattering by dust and gas in the interstellar medium of the Milky Way. Evolutionary and K-corrections are applied to take into account redshift effects and changes in a galaxy's luminosity and color between the time the light was emitted and today. We determine a K-band luminosity L_K from this corrected m_{k20} using our assumed cosmology and redshifts listed in Table A.1. The enclosed stellar mass M_* within r_{k20} is then calculated using (Bell et al., 2003):

$$\log \frac{M_*}{L_K} = -0.206 + 0.135(B - V) \tag{2.10}$$

where we have taken a color of $B - V = 1.0$ that is appropriate for BCGs. Using this M_* and r_{k20}, we compute the equivalent stellar velocity dispersion σ_* assuming the potential of a cored singular isothermal sphere in equation 2.9 which yields the expression

$$M(< r) = \frac{2r}{1 + (r_I/r)^2} \frac{\sigma^2}{G} \tag{2.11}$$

As discussed more in detail by Hogan et al. (2016), this equivalent stellar velocity dispersion σ_* is the inferred velocity dispersion that would be measured at r_{k20} if the BCG consisted only of its stars.

2.4.3 Spectral Fitting and Mass Profile

We run a fit using the ISONFWMASS in XSPEC model to determine the parameters of the cluster NFW potential (ρ_0 and r_s) where we account for the stellar mass of the cluster core by freezing the isothermal velocity dispersion to our inferred σ_* and r_I to an arbitrarily small but non-zero value. The radial run of our mass profile is then the sum of the isothermal and NFW components:

$$\begin{aligned} M_{NFW} &= 4\pi\rho_0 r_s^3 \left[\log\left(\frac{r_s + r}{r_s}\right) - \frac{r}{r_s + r}\right] \\ M_{SIS} &= \frac{2\sigma_*^2 r}{G} \end{aligned} \tag{2.12}$$

To determine the uncertainties of these quantities, we have utilized the CHAIN command in XSPEC to generate a chain of sets of parameters via a Markov Chain Monte Carlo (MCMC). A chain length of 5000 and was produced from which we adopted the standard deviation as the uncertainty of ρ_0, r_s, and mass profiles. Table A.4 shows the fitted parameters for our mass profiles. The free-fall times t_{ff} and total cluster mass proxy (M_Δ) are then computed as follows:

$$t_{ff} = \sqrt{\frac{2r}{g}} \tag{2.13}$$

$$M_\Delta = \frac{4\pi R_\Delta^3}{3}\Delta\rho_c \tag{2.14}$$

where g is the acceleration due to gravity and $\Delta = 2500$. The values of M_{2500} and R_{2500} were determined from the combined NFW profile and SIS profile by numerically solving equation 2.14.

2.5 Cavity Energetics

The radio-emitting jets from the central AGN are understood to inflate bubbles in the ICM doing work against the surrounding medium. These bubbles are seen in the X-ray surface brightness profile as cavities, and allow a direct measurement of the mechanical energy output of the AGN. Assuming the cavities are in pressure balance with the surrounding

atmosphere, the energy input from the inflation of the cavity is the sum of the cavity's internal energy and the work done

$$E_{cav} = \frac{1}{\gamma - 1} PV + PdV \approx \frac{\gamma}{\gamma - 1} PV \tag{2.15}$$

where P is the pressure surrounding the cavity, V is the volume of the cavity, and γ is the mean adiabatic index of the fluid in the cavity. For a relativistic gas, $\gamma = 4/3$, and the energy input is 4PV. We assume this value for γ as the cavities are inflated by radio synchrotron emitting jets, and therefore must be filled with relativistic gas. The mean jet power required to create a cavity is then

$$P_{cav} = \frac{E_{cav}}{t_{age}} \tag{2.16}$$

where t_{age} is the age of the cavity. We have taken our cavity power measurements from various sources in literature listed in the notes of Table A.5. These sources have estimated cavity age using the cavity's buoyancy time t_{buoy}, the time required for the cavity to rise buoyantly at its terminal velocity. In total, we find cavity power measurements for 27 systems in our sample. These measurements depend on only a few well-understood quantities and is the most reliable available.

A less reliable method for probing the mechanical output of an AGN is to use a correlation between its radio luminosity and cavity power. We derive cavity power inferred from the AGN's radio luminosity using (Bîrzan et al., 2008)

$$\log P_{mech} = (0.48 \pm 0.07) \log L_{radio} + (2.32 \pm 0.09) \tag{2.17}$$

where the total radio luminosity was calculated by integrating the flux between $\nu_1 = 10$ MHz and $\nu_2 = 5000$ MHz as

$$L_{rad} = 4\pi D_L^2 S_{\nu_0} \int_{\nu_1}^{\nu_2} (\nu/\nu_0)^{-\alpha} d\nu \tag{2.18}$$

following Bîrzan et al. (2004). We used a spectral index of $\alpha \approx 0.75$ assuming a power-law spectrum $S_\nu \sim \nu^{-\alpha}$. We have taken the ν_0 =1400 MHz flux reported in the NRAO VLA Sky Survey (NVSS) Catalog (Condon et al., 2002).

2.6 Star Formation Rate

Observations of nebular emission lines and infrared emission are commonly used to estimate star formation rates. We take two different measures of star formation rates using these two observables. We use optical line luminosities $L_{H\alpha}$ and calculate star formation rates using (Kennicutt, 1998a)

$$SFR(M_\odot\ yr^{-1}) = 7.9 \times 10^{-42}\ L_{H\alpha}(erg\ s^{-1}) \tag{2.19}$$

where $L_{H\alpha}$ is obtained from Edge (2001), Salomé and Combes (2003), and the ACCEPT database (Donahue et al., 2006; Cavagnolo et al., 2009). This is corrected for reddening using $2.7 \times SFR^{1.3}$ (Kewley et al., 2002). We take the star formation rates reported in O'Dea et al. (2008) derived from infrared luminosities using the equation (Bell, 2003)

$$SFR(M_\odot\ yr^{-1}) = A \left(\frac{L_{IR}}{L_\odot}\right) \left(1 + \sqrt{10^9 L_\odot / L_{IR}}\right) \tag{2.20}$$

where $A = 1.57 \times 10^{-10}$ for $L_{IR} > 10^{11} L_\odot$ and A= 1.17×10^{-10} at lower luminosities. For convenience, we denote $SFR_{H\alpha}$ and SFR_{IR} as the star formation rates derived from optical and infrared emissions, respectively.

Chapter 3

Discussion

3.1 Cooling Time and Molecular Gas Mass

In this section, we investigate whether the cooling time of the ambient gas is related to the molecular gas mass found in the central galaxies of cooling-flow clusters. We plot the molecular gas mass found in BCGs against the central cooling times of the hot atmosphere in Figure 3.1. Because we have more than one molecular gas mass estimate for some of the systems in our sample as shown in Table A.2, we plot the estimates derived from Edge (priv. comm, 2016) when available; otherwise, we plot the recomputed estimates from Edge (2001) or those taken from Salomé and Combes (2003). It needs to be noted that the X-ray spectra extracted for the systems in our sample have different bin sizes for their innermost regions because they vary greatly in redshift.

The effect of having different innermost bin sizes is seen in Figure 3.2 which plots the central cooling time against the mean radius of the innermost region, $R_{mid} = (R_{inner} + R_{outer})/2$. Note that the lowest cooling times are observed in nearby objects, and that there is a tendency to measure lower central cooling times with smaller R_{mid}. To take this resolution effect into account, we also plot on the right panel of Figure 3.1 the cooling time at a single physical radius of 10 kpc. We used linear interpolation of the profiles in log-log space. For systems whose innermost regions have $R_{mid} > 10$ kpc, we extrapolate their cooling time at 10 kpc. Note that when cooling times are plotted at 10 kpc as in the right panel of Figure 3.1, cooling times below 2×10^8 yr are not observed.

It is evident from Figure 3.1 that CO detections, which are indications of molecular gas, preferentially occur in systems with central cooling times below $\sim$1 Gyr. Furthermore, the

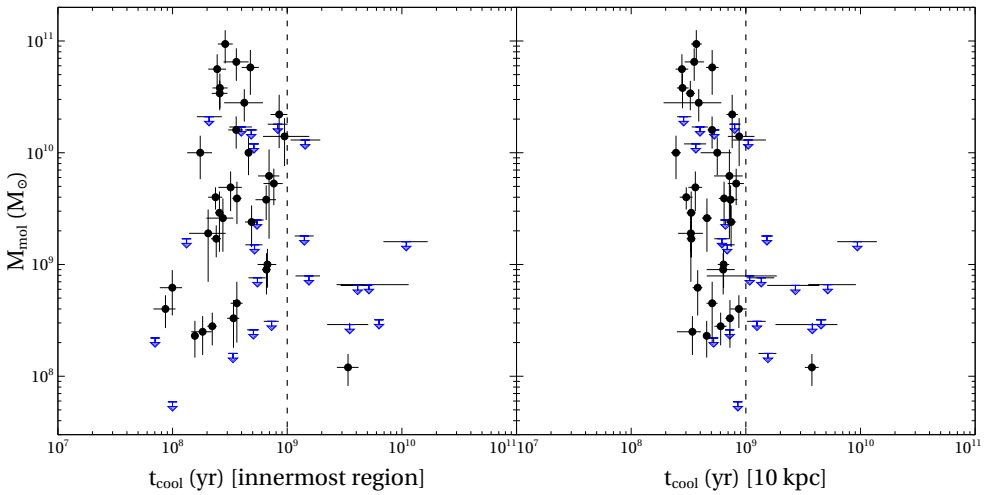

Figure 3.1: Molecular gas mass vs. cooling time measured at the mean radius of the innermost region (left panel) and the cooling time measured at 10 kpc (right panel). Black symbols denote systems observed with CO emission while blue symbols denote upper limits.

spread of the cooling time distribution below ∼1 Gyr is narrow with a mean and coefficient of variation[1] of $\mu \approx 0.50$ Gyr and $c_v \approx 0.38$ for detections only. This threshold suggests that the presence of molecular gas depends critically on the presence of cooling gas with short cooling times. This supports the hypothesis that molecular clouds in BCGs likely form from the cooling of the hot intracluster medium. We take this as our working hypothesis for the remainder of the section, which will be discussed in more detail in Section 3.3.

In the histogram of central cooling times shown in the left panel of Figure 3.3, we observe two types of outliers for the cooling time threshold at 1 Gyr: (1) The system A1060 with a long central cooling time nevertheless observed with molecular gas, and (2) Eleven systems with short central cooling times but no detected molecular gas. The latter type imply that a short cooling time does not guarantee the detection of molecular gas via CO emission as the tracer. We consider these exceptions below.

The cluster A1060 is classified as having a weak cool core (1 Gyr $< t_{cool} <$ 7.7 Gyr) (Mittal et al., 2009). With a central cooling time of about 4 Gyr, A1060 is observed to harbor molecular gas mass of $1.4 \pm 0.2 \times 10^8$ $M_\odot$ within an observed volume of radius about 6 kpc. This outlier appear to violate the sharp cooling time threshold observed in Fig 3.1; however, the core of A1060 can be attributed to having a small corona (Sun, 2009)

[1]Coefficient of variation $c_v = \sigma/\mu$ shows the extent of variability in relation to the mean μ where σ is the standard deviation.

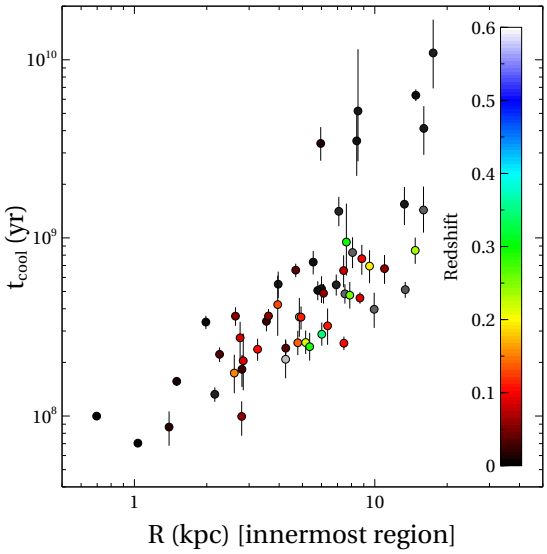

Figure 3.2: Cooling time in the innermost region plotted against the mean radius of the innermost region. The tendency of the cooling time to increase with size of the innermost region is easily observed in this figure.

which may provide fuel for the condensation of molecular gas despite its long cooling time. Because of its long central cooling time, we would expect it to have an environment that is not conducive to star formation or molecular gas condensation. While X-ray coronae of early-type galaxies in hot clusters are thought not to survive due to processes such as ICM stripping, evaporation, rapid cooling, and powerful AGN outburst, they have been found to be very common. Moreover, coronae of central dominant galaxies embedded in the hot ICM of clusters (e.g Coma, A1060, A3267,A1367,A576,A3376 and A3558) have been detected (Sun et al., 2007). These include the two coronae associated with the central dominant galaxies NGC 3311 and NGC 3309 of A1060 as reported by Yamasaki et al. (2002). Sun et al. (2007) describes these coronae of central dominant galaxies as mini-versions of group and cluster cooling cores where the cooling of the coronal gas may provide fuel for the central SMBH and nuclear star formation in a weak cool core environment (1 Gyr $< t_{cool} <$ 7.7 Gyr). If this is the case, then it would not be implausible for the condensation of molecular gas to occur in A1060 fueled by the cooling gas of its corona making it consistent with our working hypothesis.

Next, we address systems with short cooling times but no detection in CO. In the left panel of Figure 3.3, it appears that the distribution of non-detections (blue) below the threshold of 1 Gyr are drawn from the same distribution as detections (grey). A

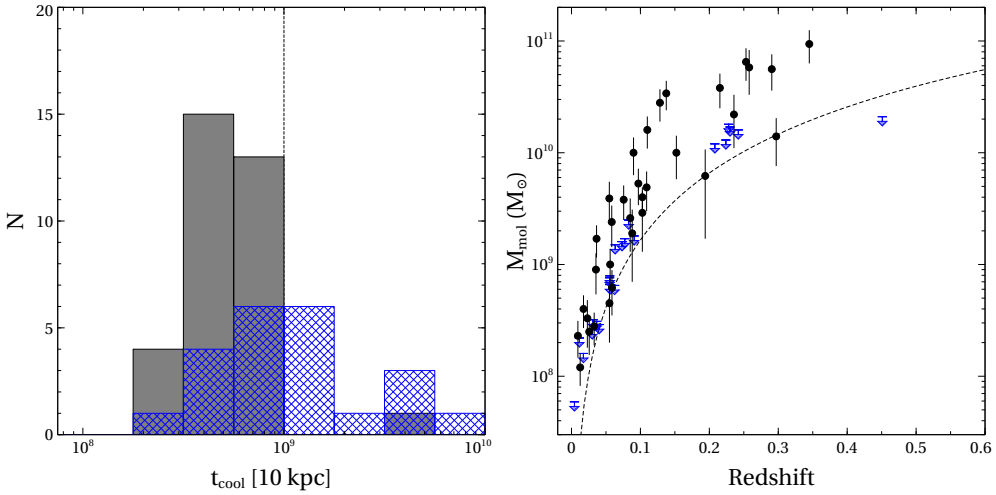

Figure 3.3: *Left:* Histogram of the cooling times at 10 kpc. Grey bars denote clusters detected in CO while blue bars denote non-detection. *Right:* Molecular gas mass vs. redshift. The dashed curve represents the molecular mass limit that can be derived from CO(1-0) observations with the IRAM 30m telescope assuming a typical 300 km s^{-1} linewidth and a temperature detection limit of 0.5 mK. The molecular gas mass for the two systems below this curve were derived from CO(3-2) observations. Black symbols denote systems observed with CO emission while blue symbols denote upper limits.

Kolmogorov-Smirnov (K-S) test gives a p-value of 0.22, which is too large to reject the null hypothesis that they are drawn from the same parent distribution. It is possible that molecular gas is present but its radiation is below the detection limit of the IRAM 30m telescope.

The right panel of Figure 3.3 shows molecular gas mass plotted against redshift. The dashed line represents the molecular mass limit that can be derived from CO(1-0) observations with the IRAM 30 m telescope. Due to this detection limit, molecular clouds with CO(1-0) line emission below this curve will not be visible. On the other hand, the molecular gas may not be present at all. With short cooling times, condensation from the ICM onto the central dominant galaxy should be occurring; however, the absence of a cooling by-product such as molecular gas suggests that some mechanism suppressing its formation must be present. Edge (2001), Salomé and Combes (2003), and Rafferty et al. (2008) had considered AGN feedback as the mechanism responsible for suppressing molecular gas and star formation. We explore this possibility for our sample in Section 3.6.

In summary, we show that systems with molecular gas are preferentially observed when $t_{cool} \lesssim 1$ Gyr and this points to the cooling of the hot atmosphere as its origin. This is consistent with the cooling time threshold at $\sim$1 Gyr observed by Rafferty et al. (2008)

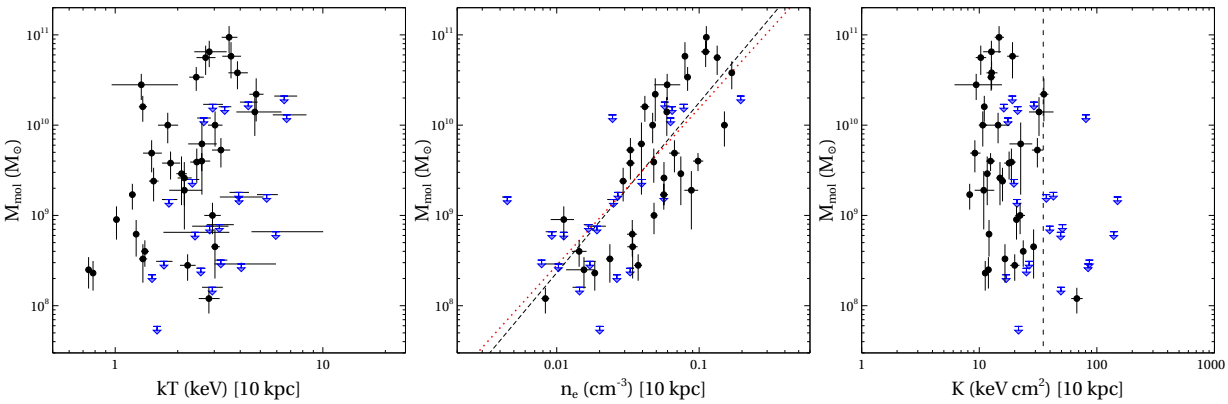

Figure 3.4: Molecular gas mass vs. temperature, density, and entropy derived at 10 kpc. Black symbols denote systems observed with CO emission while blue symbols denote upper limits. In the middle panel, the dotted red line is a fit to the entire sample while the dashed black line is a fit only to the systems with CO detection.

for the onset of star formation. One would expect that with shorter cooling time, more hot gas will condense; however, instead of a negative correlation between molecular gas mass and cooling time, we observe a threshold. Below this threshold, we observe a narrow spread of cooling time (1 decade) yielding a wide span (3 decades) of detected molecular gas mass.

3.2 Entropy and Molecular Gas Mass

Understanding the connection of the ICM with the presence of molecular gas is one of the goals of this project. To this end, we also investigated the dependence of molecular gas with properties of the ICM other than its cooling time: temperature, density, and entropy. In Figure 3.4, we show the plot of molecular gas mass against each of these properties. We plot the values of these properties at 10 kpc to account for resolution effect just like in the previous section.

While we find no obvious correlation between molecular gas mass and temperature, molecular gas mass and density appear to be strongly correlated. Using an ordinary least squares regression, we find the best fit between these two quantities for the entire sample ($\sigma^2 = 0.59$) to be

$$\log M_{mol} = (1.74 \pm 0.39) \log n_e + (11.93 \pm 0.57) \tag{3.1}$$

while the best fit for the systems with CO detections only ($\sigma^2 = 0.60$) is given by

$$\log M_{mol} = (1.90 \pm 0.51) \log n_e + (12.15 \pm 0.70) \tag{3.2}$$

Higher molecular gas mass appears to be situated in higher density ICMs. No threshold on molecular gas mass is found when it is plotted against temperature (kT) or density (n_e); however, when plotted against entropy ($K = kTn_e^{-2/3}$), it is evident in the third panel of Figure 3.4 that the observations of molecular gas occur only in systems with entropy below $\sim$ 35 keV cm^2 with the exception of the same outlier as in the previous section (A1060). This is consistent with the entropy threshold at $\sim$30 keV cm^2 observed by Cavagnolo et al. (2009) for the onset of Hα emission observed in cluster cores. Evidently, low entropy does not guarantee the observation of molecular gas as several systems with entropy $\lesssim$ 35 keV cm^2 do not have CO detection. Furthermore, the spread of the entropy distribution below $\sim$35 keV cm^2 for systems with CO detection is narrow ($\mu \approx 16.8$ keV cm^2 and $c_v \approx 0.42$). Within a narrow range of entropy ($\sim 7 - 35$ keV cm^2), we observe three decades of molecular gas mass.

Summarizing the results from the previous two sections, the $M_{mol}-t_{cool}$ and the $M_{mol}-K$ relations suggest thresholds at $\sim$1 Gyr and $\sim$ 35 keV cm^2, respectively, for the detection of molecular gas mass in cluster cores.

3.3 Thermal Instability In the Hot Atmosphere

Several studies have shown that cold gas in cluster cores is highly correlated with the properties of the intracluster medium. For example, systems with Hα emission and blue excess emission have been preferentially detected with low central cooling time ($\lesssim$ 1 Gyr) and entropy index ($\lesssim$ 30 keV cm^2) (Cavagnolo et al., 2008; Rafferty et al., 2008; Voit and Donahue, 2015). While Hα and blue excess emission serve as tracers for the cold 10^4 K ionized gas and recent star formation in cluster cores, respectively, CO line emissions represents the most accessible tracer for the molecular component of the ICM. The 10^4 K ionized gas component of cold gas in cluster cores weighs in at about 10^4 M$_\odot$ (Böhringer et al., 2007) while the molecular component weighs in at about 10^{8-11} M$_\odot$ (Salomé and Combes, 2003; Edge, 2001), making molecular hydrogen the bulk of the cold gas. This makes CO emission a powerful tracer for the presence of significant cooling in cluster cores.

We have found that molecular gas is preferentially observed in cluster cores when central cooling time or entropy index drops below $\sim$1 Gyr or $\sim$35 keV cm^2, respectively. This shows

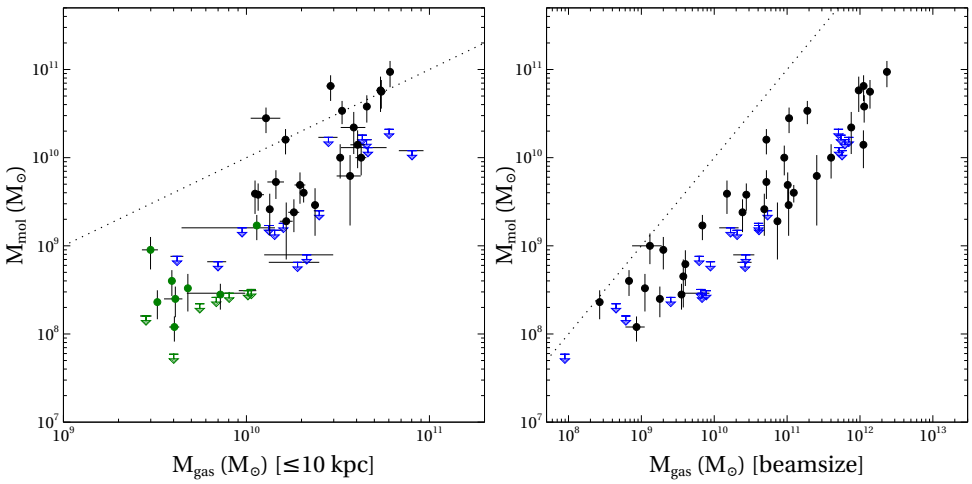

Figure 3.5: Molecular gas mass vs. surrounding hot gas mass enclosed within 10 kpc from the cluster centre (Left) and within the beam of the IRAM 30m telescope (Right). The average beam size used when the systems in our CO sample was observed by the IRAM30m telescope is about 24 arcseconds (Edge, 2001; Salomé and Combes, 2003). The dotted line shows equality of the quantities. Circles denote systems observed with CO emission while arrows denote upper limits. Green symbols represent objects with redshifts ≤0.042 and IRAM beams smaller than 10 kpc in radius.

that molecular gas is directly related to the local state of the intracluster gas suggesting that its origin involves the cooling of the intracluster medium. This points to thermal instability in the hot atmosphere as the source of cold gas (Cowie et al., 1980; Nulsen, 1986; Pizzolato and Soker, 2005). Under this framework, when the atmosphere becomes thermally unstable, overdense blobs formed by perturbations cool to low temperatures ($< 10^4$ K), decouple from the hot atmosphere, and may form stars or molecular gas.

In the left panel of Figure 3.5, we plot molecular gas mass against the mass of the surrounding hot gas within a radius of 10 kpc. Note that there are several systems that lie above the line of equality in the figure. To explore this issue, we plot the systems with redshifts $z \leq 0.042$ and an IRAM beam smaller than 10 kpc in radius as green symbols in the same figure. Consequently, we find that the lower molecular gas mass values in this figure is a result of the IRAM beam not covering all the cooling region and the higher ones relating to systems where the cooling region is larger than 10 kpc. This motivates a plot between molecular gas mass and surrounding hot gas observed within the IRAM beam as shown in the right panel of Figure 3.5. It is evident from this plot that that the surrounding hot atmosphere offer a vast reservoir of hot gas to fuel the observed molecular gas.

As shown by the arguments of Nulsen (1986) and simulations of McCourt et al. (2012), thermal instability is guaranteed when the ratio of the cooling to free-fall time satisfies $t_{cool}/t_{ff} \lesssim 1$. In the next section, we explore the $\min(t_{cool}/t_{ff})$ quantity as a criterion for thermal instability in cluster cores as applied to our CO sample.

3.4 Ratio of Cooling Time Over Free-Fall Time and Molecular Gas Mass

Precipitation models have concluded that when the ratio of the cooling time to free-fall time (t_{cool}/t_{ff}) falls below a certain threshold, condensation of hot gas ensues fueling the development of the cold phase (McCourt et al., 2012; Singh and Sharma, 2015; Gaspari et al., 2012; Li et al., 2015; Voit et al., 2015; Voit and Donahue, 2015; Prasad et al., 2015; Lakhchaura et al., 2016). In this section, we explore this thermal instability criterion for our sample.

The left panel of Figure 3.6a shows molecular gas mass found in the cluster core plotted against the minimum ratio of the cooling to free-fall time as a function of radius. It is apparent in the figure that systems with molecular gas is preferentially observed when the cooling to free-fall time ratio falls below ∼25. Studies have reported a series of values for the threshold upon which the $\min(t_{cool}/t_{ff})$ quantity divides cluster cores that exhibit multiphase gas from those that do not. Simulations have reported this threshold to be ∼1 in a plane-parallel geometry with idealized heating (McCourt et al., 2012), ∼10 in a spherical geometry with heating provided by AGN Feedback (Singh and Sharma, 2015; Gaspari et al., 2012; Prasad et al., 2015), and the range $1 \lesssim \min(t_{cool}/t_{ff}) \lesssim 20$ when employing AGN and stellar feedback as the source of heating (Li et al., 2015). Using observed radial profiles of t_{cool}/t_{ff} for a number of clusters, this threshold is reported to be ∼10 (McCourt et al., 2012; Lakhchaura et al., 2016) and the range $4 \lesssim \min(t_{cool}/t_{ff}) \lesssim 20$ (Voit et al., 2015; Voit and Donahue, 2015). The difference in the approach of how t_{cool}/t_{ff} is computed in these studies is evident in the wide range of these reported thresholds. In this and the following section, we discuss the contrast between our results and that of some of the studies mentioned above to evaluate the robustness of the $\min(t_{cool}/t_{ff})$ criterion for thermal instability as a proxy for the condensation of cold gas.

Similar to our approach, both McCourt et al. (2012) and Voit and Donahue (2015) examined this criterion by measuring the ratio of the average cooling time in radial bins and dividing by an estimate of the free-fall time from a given radius. These two studies used ICM profiles from the ACCEPT catalog (Cavagnolo et al., 2009) to derive the cooling

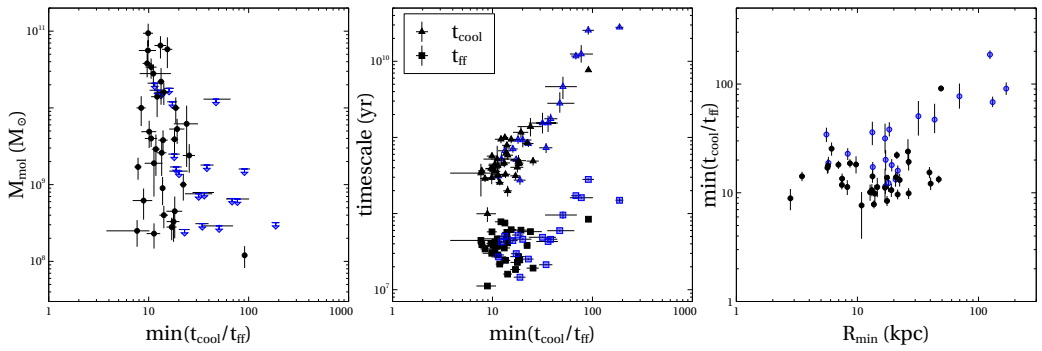

(a) Plots for our sample

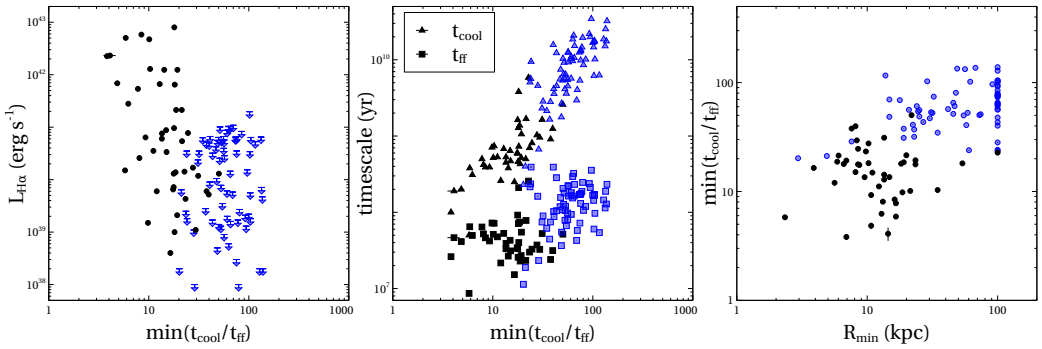

(b) Data from Voit and Donahue (2015)

Figure 3.6: *Left panel*: Cold gas tracer (M_{mol} or $L_{H\alpha}$) vs. minimum cooling to free-fall time ratio. *Middle panel*: Minimum cooling to free-fall time plotted against its numerator and denominator. *Right panel*: R_{min} is the radius at which $\min(t_{cool}/t_{ff})$ occurs. Black symbols denote systems observed with CO emission while blue symbols denote upper limits.

time in radial bins. The difference in their reported threshold is largely due to the approach they have taken to estimate the free-fall time. While both used smoothed pressure P(r) and temperature T(r) profiles to calculate t_{ff}, only Voit and Donahue (2015) took into account the dominance of the central galaxy's stellar mass to the gravitational potential at the inner radii of $\sim$ 10 kpc (Li and Bryan, 2012). This would bias the t_{ff} values measured by McCourt et al. (2012) higher and consequently the t_{cool}/t_{ff} values lower. This could explain the higher threshold of $\sim$20 reported by Voit and Donahue (2015) compared to $\sim$10 reported by McCourt et al. (2012). From this comparison, we find that the influence of the central galaxy's stellar mass made a factor of two difference in the reported $\min(t_{cool}/t_{ff})$ threshold. This motivated us to account for the stellar mass of the central galaxy in our estimation of t_{ff} using an approach that improves upon the one used by Voit and Donahue

(2015). Unlike their approach, where a velocity dispersion floor of 250 km s^{-1} for the central galaxy was taken, we inferred stellar velocity dispersion for each system in our sample using 2MASS isophotal magnitudes (see Section 2.4.2). Our mass profile is then made up two components: a SIS profile reflecting the inferred velocity dispersion and an NFW profile fitted from the system's X-ray emission. While the NFW component describes the mass of the system accurately in large radii, the SIS component accurately account for the gravitating mass contributed by the stars of the central galaxy (e.g Fisher et al., 1995).

We measure a similar range of t_{ff} to that of Voit and Donahue (2015) as evident in the middle panels of Figure 3.6a and 3.6b. We find that systems with molecular gas are preferentially observed when $10 \lesssim \min(t_{cool}/t_{ff}) \lesssim 25$. Contrast this to the findings of Voit and Donahue (2015) and Li et al. (2015), where they have found $\min(t_{cool}/t_{ff})$ as low as $\sim$4 and $\sim$1, respectively. It is possible that the lack of systems with $\min(t_{cool}/t_{ff})$ below $\sim$10 in our observation may just be due to a difference in sample. Nonetheless, that $\min(t_{cool}/t_{ff})$ criterion exhibit a range of threshold is evident in both observation and simulation and has been attributed by Voit and Donahue (2015) as a result of swings around the simulation-derived value of $\sim$10 (Singh and Sharma, 2015; Gaspari et al., 2012). In precipitation models, this "hysteresis effect" is a result of cold mode feedback. When $\min(t_{cool}/t_{ff})$ falls below $\sim$10 in a cooling atmosphere, condensation ensues, and a fraction of the resulting cold gas fuels the AGN. This leads to a sudden enhancement in the accretion rate of the SMBH causing the AGN to release strong jets and overheat the surrounding atmosphere such that $\min(t_{cool}/t_{ff}) \gtrsim 10$. This suppresses the condensation of cold gas slowing down the SMBH accretion rate, which allows the hot atmosphere to cool once again and restart the cycle. These large fluctuations in central density and cooling time in lockstep with the SMBH accretion rate is consistent with the findings of Li et al. (2015) in their simulations. How much does the AGN contribute to the scatter in central density and cooling time? We consider this question in the next section by exploring the effects of AGN feedback on ICM properties.

No relationship was found between the cooling to free-fall time ratio and the radius R_{min} at which the minimum of the ratio occurs as shown in the right panels of Figure 3.6. For both our sample and the sample from Voit and Donahue (2015), the figures show a scatter for the plots of these two quantities. Thus, we do not observe R_{min} to be related to any of the physical quantities we have analyzed.

To summarize, while the cooling time and entropy thresholds ($t_{cool} \lesssim 1$ Gyr and $K \lesssim 35$ keV cm^2) successfully divide the systems in our sample from those with and without CO emission, the $\min(t_{cool}/t_{ff}) \lesssim 10$ criterion derived from simulations (Singh and Sharma, 2015; Gaspari et al., 2012; Prasad et al., 2015) does not. The range of $\min(t_{cool}/t_{ff})$ for which we observe CO emission is within the range observed by Voit and Donahue (2015)

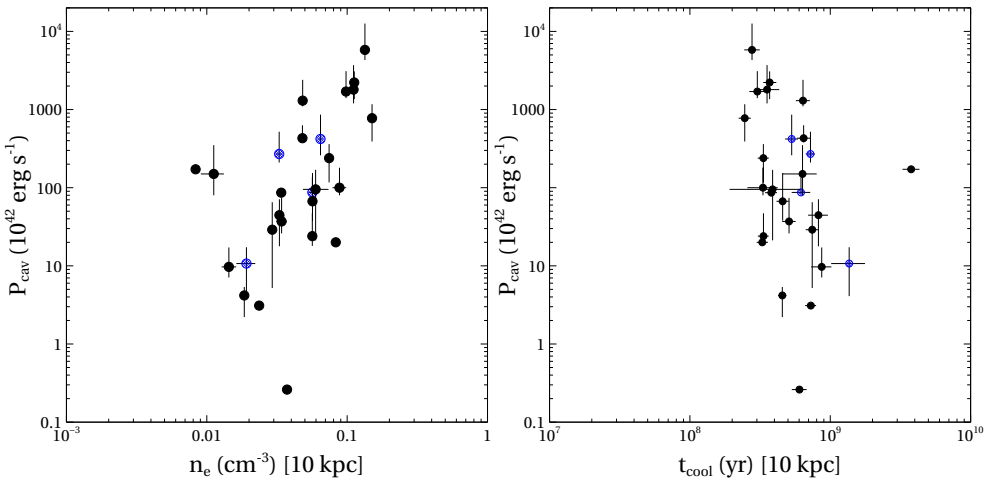

Figure 3.7: Cavity power plotted against electron density (Left) and cooling time (Right) at 10 kpc. Black symbols denote systems observed with CO emission while blue symbols denote non-detection.

and simulated by Li et al. (2015). Evident on the middle panels of Figure 3.6, which plots the numerator and denominator of the observed values of $\min(t_{cool}/t_{ff})$ for the sample in this thesis and Voit and Donahue (2015), the numerator is more strongly correlated than the denominator with the ratio. In other words, what's driving the value of $\min(t_{cool}/t_{ff})$ is primarily cooling time. Thus, the cooling time and entropy index thresholds forecasts the onset of CO emission just as well (if not better) than the $\min(t_{cool}/t_{ff})$ criterion in our sample of BCGs.

3.5 The Effect of AGN Feedback On ICM Properties

Active galactic nuclei at the center of galaxy clusters have emerged as the most promising means powerful enough to prevent significant amounts of cooling in the intracluster medium (Bîrzan et al., 2004; Rafferty et al., 2006). In this section, we wish to find to what extent does the AGN outburst disrupt the surrounding hot atmosphere in the aim of extending our discussion of thermal instability and the $\min(t_{cool}/t_{ff})$ criterion from the previous section.

Several studies have claimed that the hot atmosphere experiences large fluctuations in gas density and cooling time in response to AGN power output over a span of several Gyr. For example, Voit and Donahue (2015) reasons that fluctuations in SMBH cold accretion lead to fluctuation in the AGN feedback without necessarily eradicating all of the cold gas. This fluctuation in AGN power causes gas density and cooling time swings

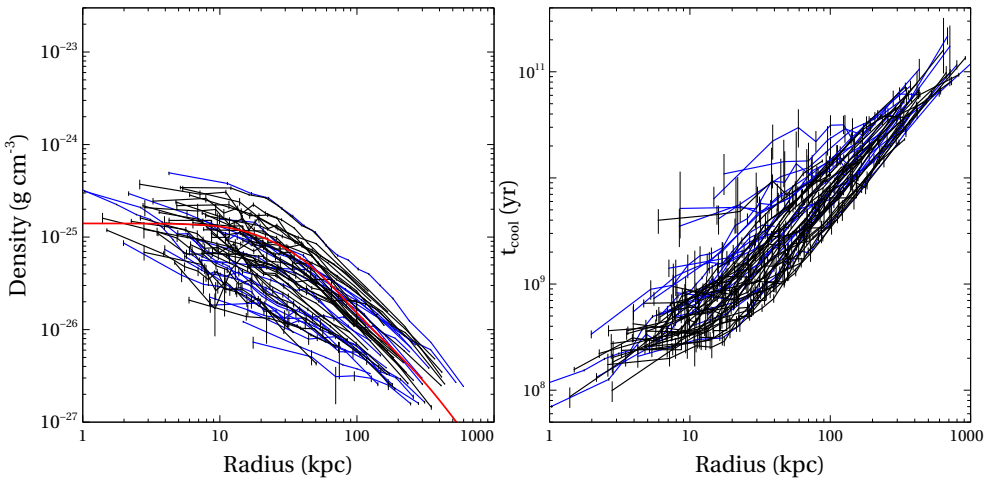

Figure 3.8: *Left:* Deprojected gas density profiles of our sample. The solid red line profile shows the gas density of the Perseus cluster (Mathews et al., 2006); the gas density profiles in the simulation of Li et al. (2015) bounce around this profile. *Right:* Deprojected cooling time profiles of our sample. Black symbols denote systems observed with CO emission while blue symbols denote non-detection.

that are sufficiently large to explain the observed range of $4 \lesssim \min(t_{cool}/t_{ff}) \lesssim 20$. This is consistent with the simulations of Li et al. (2015) where they find large fluctuations in central gas density, minimum cooling time, and amount of cold gas in lockstep with the SMBH accretion rate over a span of 6.5 Gyr. Over this length of time, the simulated cluster goes through three cycles of heating (AGN and stellar feedback) and cooling with t $\approx$ 1.5, 4.3, and 6.0 Gyr marking the end of each cycle in their standard run. The majority of systems in our CO sample are found in the redshift z $\leq$ 0.4, which corresponds to a lookback time of $\leq$ 4.28 Gyr. This means that if the simulations of Li et al. (2015) are representative of a cluster's evolution, then on average, our sample is probing the lifetime of a cluster over two of its most recent cycles of heating and cooling. With this in consideration, we can use our sample to investigate the effect of hysteresis on cluster cores by comparing our results to that of Li et al. (2015).

We begin by comparing the AGN mechanical power simulated in Li et al. (2015) and the observed cavity powers for our sample. For each cycle of the simulated cluster, the instantaneous SMBH accretion rate shows very large variations, but with an average of $\dot{M}_{SMBH} \approx 5.0\ M_\odot\ yr^{-1}$ (see Figure 2 of Li et al., 2015). This is equivalent to about 1.4×10^{46} erg s^{-1} of kinetic power of the jet using

$$\dot{E}_{kinetic} = f_{kinetic} \epsilon \dot{M}_{SMBH} c^2 \tag{3.3}$$

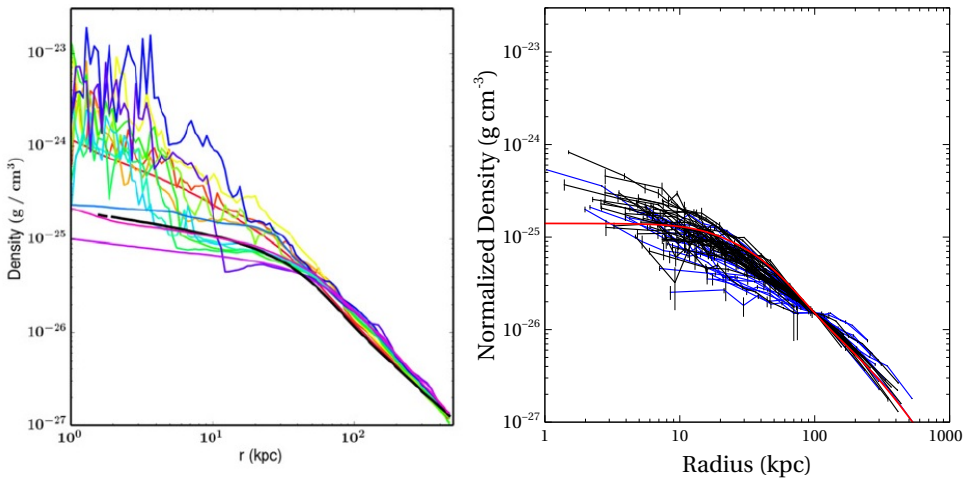

Figure 3.9: *Left*: Simulated gas density profiles in the standard run of Li et al. (2015). *Right*: Gas density profiles of our sample normalized over the gas density of Perseus (Mathews et al., 2006).

where the jet was assumed to be 50% thermalized ($f_{\rm kinetic} = 0.5$) and a feedback efficiency of $\epsilon = 1\%$ (Li et al., 2015). Similarly, the systems in our sample exhibit a wide range of AGN mechanical power ($\sim 10^{42-46}$ erg s^{-1}) as shown in Figure 3.7 where we obtained cavity powers from the literature for 27 out of 55 systems of our sample. Despite the wide range (five decades) of AGN mechanical power released into the hot atmosphere, the gas densities and cooling times at 10 kpc span a narrow range of roughly a decade. Furthermore, the gas density and cooling time profiles (Figure 3.8) of our sample have similar shapes. In contrast, the gas density of the simulated cluster in Li et al. (2015) bounces around the initial condition shown as a solid black line in the left panel of Figure 3.9. This solid black line is the density profile of the Perseus cluster taken from Mathews et al. (2006) and we denote it as $\rho_{\rm Perseus}$. To take into account the variance among our sample, we normalize our gas density profiles to this solid black line at 100 kpc such that $\rho_{\rm normalized} = \rho \times (\rho_{\rm Perseus,100\ kpc}/\rho_{100\ \rm kpc})$. The resulting normalized density profiles are shown in the right panel of Figure 3.9 and suggests that the large fluctuation in gas density as a result of variability in the strength of AGN outbursts exhibited in simulations are not observed.

Furthermore, we find that AGNs are energetically able to balance radiative losses from the ICM for the systems in our sample. The left panel of Figure 3.10 shows cavity power (heating rate) versus the bolometric X-ray luminosity (cooling rate) of the ICM within the cooling radius for our sample. We have taken the cooling radius defined as the radius at which the cooling time is ≤ 3 Gyr, consistent with previous studies (Dunn and Fabian,

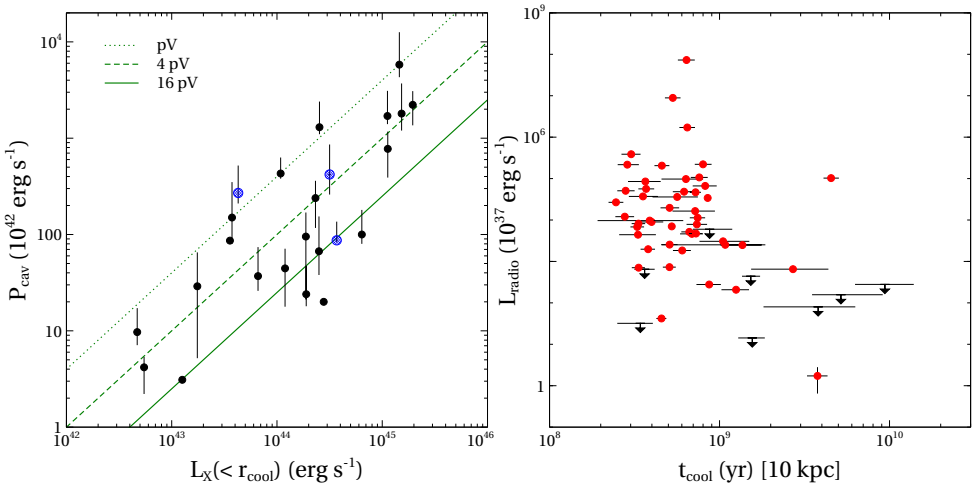

Figure 3.10: *Left*: Cavity power vs. X-ray luminosity within the cooling radius. Here we define the cooling radius as the radius at which the cooling time is $\lesssim$3 Gyr consistent with previous studies (Dunn and Fabian, 2006; Panagoulia et al., 2014b). *Right*: Radio luminosity vs. cooling time at 10 kpc.

2006; Panagoulia et al., 2014b). Most sources in the figure lie between the PV and 16PV lines indicating the sufficiency of the AGN jet power to quench the cooling flow to the observed levels. Note that plotted in this figure are cavity measurements for only 27 out of 55 systems of our sample. However, 49 of these systems are bright in 1400 MHz radio emission ($L_{radio} \geq 10^{37}$ erg s^{-1} ; right panel of Figure 3.10), which are only present in cooling flows and used as a tracer for AGN outbursts (Bîrzan et al., 2012). This is consistent with a duty cycle of at least 70% for radio-mode feedback (Dunn and Fabian, 2006; Bîrzan et al., 2012). That is, cooling flows spends most of their time with cavities in their hot atmospheres undergoing almost non-stop energy injection from the central AGN. This fairly continuous input of energy from the AGN favors a relatively gentle and self-regulated AGN feedback, rather than one that is sudden and violent (Bîrzan et al., 2012; Panagoulia et al., 2014b). In conclusion, a strong AGN outburst can turn off a cooling flow in the outer regions while maintaining the cooling time short in the inner regions even after the shock propagates through the cluster (Soker et al., 2001). Indeed, the effects of continual AGN outbursts on the ICM is gentle as it is immune to large swings in central gas density and cooling time (McNamara and Nulsen, 2012).

3.6 AGN Feedback and Molecular Gas

Heating and cooling in clusters of galaxies involves a relatively close balance between the strength of AGN outbursts and cooling of the ICM as shown in Figure 3.10 of the previous section. Crucial to this balance is the accretion mechanism of the SMBH to form a feedback loop with the ICM. While accretion from the hot phase of the ICM has been found to be sufficient to power low-luminosity radio sources (Allen et al., 2006), it is too feeble to fuel powerful AGNs (Rafferty et al., 2006; Hardcastle et al., 2007; McNamara et al., 2011). Instead, the SMBH accretes cold gas connecting the by-product of ICM cooling with the outburst from the AGN (Pizzolato and Soker, 2005; Gaspari et al., 2012; Li and Bryan, 2014; Prasad et al., 2015). If this is the case, a correlation between molecular gas mass and AGN power in central cluster galaxies would be expected in our CO sample. However, no correlation is seen between these two quantities as shown in Figure 3.11. For systems with roughly equal available molecular gas, we observe a three decade scatter in cavity power or radio luminosity. Considering the magnitude of these cavity power, only a small fraction of the observed molecular gas is needed to fuel them. This is consistent with the observations of McNamara et al. (2011) and O'Dea et al. (2008) who suggested that most of the cold gas is consumed by star formation rather than accreted by the SMBH. To determine a depletion timescale for the molecular gas observed in our sample, we plot molecular gas mass against star formation rate in Figure 3.12. The ratio of molecular gas mass to star formation rate yields a *median* depletion timescale of $\sim$1 Gyr. This timescale is roughly constant over the range of molecular gas mass and star formation rates observed for our sample. Note that these star formation rates are instantaneous values. This value is consistent with the findings of O'Dea et al. (2008) for a sample of BCGs while Kennicutt (1998a) finds a median depletion timescale of $\sim$2.1 Gyr in a study of 61 normal spiral galaxies. Observation of cosmic star formation rate increases as a function of redshift until it reaches its peak at $z \approx 2-3$, after which it decreases by an order of magnitude (Hopkins and Beacom, 2006). So this depletion timescale should be viewed as an instantaneous value. Note that the left and right panels of Figure 3.12 is a reworking of Figure 8 in O'Dea et al. (2008) and equivalent to Figure 9 in Edge (2001), respectively.

Analytical models (Pizzolato and Soker, 2005) and high resolution simulations (Gaspari et al., 2012; Li and Bryan, 2014; Prasad et al., 2015; Li et al., 2015) of cool core clusters may offer an additional insight: Considering that only a small fraction of the detected molecular gas is needed to produce the observed AGN power, the molecular gas that is not accreted onto the SMBH may settle into a rotating disc. That is, dense cold gas decouples from the hot ICM phase down onto the central regions of the core, forming a cold rotating torus and in part feeding the SMBH. Cold molecular gas disks have been

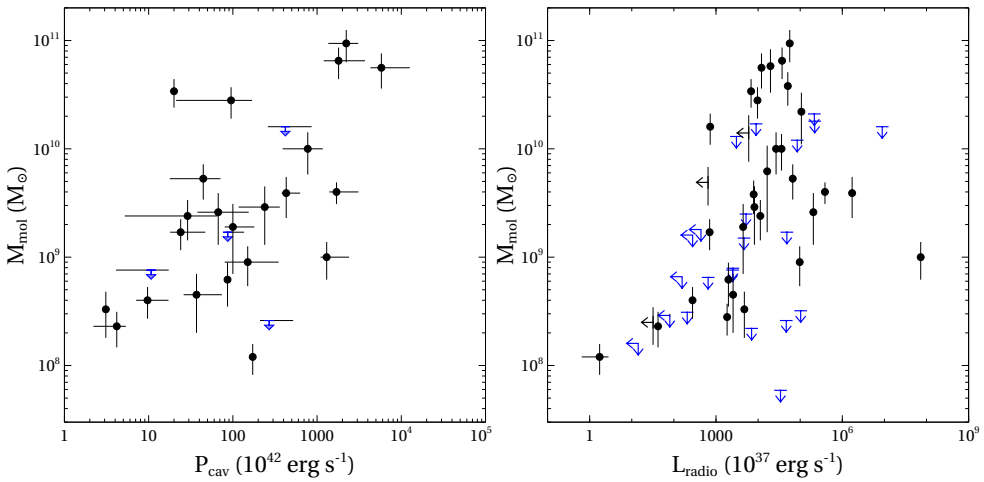

Figure 3.11: Molecular gas mass vs. cavity power (Left) and radio luminosity (Right). Black symbols denote systems observed with CO emission while blue symbols denote upper limits.

observed in some BCGs: the ∼5 kpc rotating disc of molecular gas located in the core of the Hydra-A cluster (Hamer et al., 2014) and the molecular gas disk observed in the central kiloparsec of NGC383 and NGC1275 (Wilman et al., 2005; Okuda et al., 2005). Molecular gas forms cold rotating torus that is in part feeding the SMBH and mostly consumed by star formation resulting to the large scatter observed between the total molecular gas and AGN power (Prasad et al., 2015).

Results from recent ALMA observations of molecular gas in central galaxies of clusters offer an interesting insight to the dynamics of the molecular gas. Resolving the spatial and velocity structure of the cold molecular gas using ALMA, Russell et al. (2016b) observed that the molecular gas in the PKS0745-191 BCG is distributed along three narrow filaments (3-5 kpc in length) with velocity dispersion significantly less than the typical stellar velocity dispersion of such a massive BCG. Low velocities have been observed in a growing sample of BCGs observed with ALMA such as NGC5044 (David et al., 2014), A1835 (McNamara et al., 2014), A1664 (Russell et al., 2014), Phoenix (Russell et al., 2016a), 2A0335+096 (Vantyghem et al., 2016), and A2597 (Tremblay et al., 2016), indicating that molecular cloud velocities well below the stellar dispersion are common among BCGs. Instead of finding molecular gas that have settled into the gravitational potential well as one would expect in the cold accretion framework discussed above (Gaspari et al., 2012) where molecular gas form a rotationally supported torus that provides most of the fuel for the AGN, we find molecular clouds that are dynamically young. A few of these ALMA observations ascribe these low velocity molecular clouds to be in disks. McNamara et al.

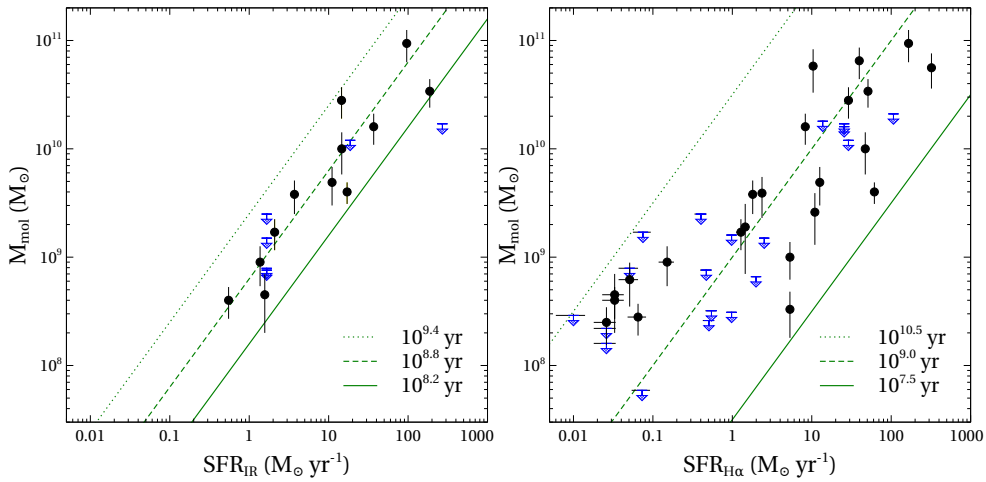

Figure 3.12: Molecular gas mass vs. star formation derived using Hα (Left) and IR (Right) luminosity. Black symbols denote systems observed with CO emission while blue symbols denote upper limits. The green lines are computed assuming gas depletion timescales posted in the figure legends.

(2014) suggested the possibility that the slow inner cloud velocities of A1835 are rotationally supported in a disk viewed in the plane of the sky. Russell et al. (2016a) observed that the central compact emission peak in CO(3-2) in the Phoenix cluster has a velocity structure that is consistent with ordered emission peak around the nucleus, but the authors also clarified that higher spatial resolution observations would be required to determine if this is a disk. Russell et al. (2014) detected molecular gas in A1664 that appears to be consistent with a flattened disk-like structure rotating in the rest frame of the BCG similar to the rotating disk in Hydra A (Hamer et al., 2014), but the radial velocity profile was not clear. Evidently, higher spatial resolution observations of a larger sample is required to test the molecular disk hypothesis.

3.7 Cooling and Uplift Models

Harboring molecular gas in the range $\sim 10^{9-11}$ $M_\odot$, BCGs host molecular gas roughly two orders of magnitude higher than is observed in typical elliptical galaxies. These giant elliptical galaxies then serve as good targets for CO surveys for detecting molecular gas and investigating their origins. While it is often claimed that mergers may explain most or all of the cold gas and dust in elliptical galaxies (Mathews and Brighenti, 2003), the acquisition of molecular gas through mergers should be rare in giant elliptical galaxies centrally located

in clusters. The high velocity dispersion among the cluster members decreases the merger rate. Similarly, ram pressure stripping of molecular gas by the hot atmosphere from a galaxy passing by a BCG is also not likely to happen as molecular gas would be more difficult to remove from cluster galaxies than atomic gas (Young et al., 2011). When a sizable sample of BCGs are found to host CO emission, then we must invoke a mechanism that appeals to properties shared by these galaxies instead of infrequent mergers. The results of this thesis are consistent with an internal origin for the molecular gas found in BCGs. The prevalence of short central cooling time or low central entropy index points to cooling of the hot atmosphere as the origin of the cold gas (Section 3.1 and 3.2). Cold gas condenses from the hot atmosphere when the condition for thermal instability is breached (Section 3.3) where the cooling time threshold predicted the onset of CO emission just as well (if not better) than the $\min(t_{cool}/t_{ff})$ criterion (Section 3.4) for our sample of BCGs.

New observations of molecular gas in BCGs made with the Atacama Large Millimeter Array (ALMA) suggest a more complex picture than rapid cooling in the hot atmosphere. Two important results revealed in these observations indicate that these molecular clouds are moving remarkably slow with respect to the stellar velocity dispersion in these massive galaxies and are either lifted out by, or condensing along the wakes of radio-inflated X-ray cavities in the hot atmosphere (David et al., 2014; McNamara et al., 2014; Russell et al., 2014, 2016a,b; Vantyghem et al., 2016; Tremblay et al., 2016). Motivated by these observations, McNamara et al. (2016) proposed a model where molecular gas condenses in the wakes of buoyantly-rising X-ray cavities. For gas to achieve thermal instability, low entropy gas caught in the updraft of rising X-ray bubbles is lifted from the cluster centre to an altitude where its cooling time is shorter than its infall time, $t_{cool}/t_I \lesssim 1$. While the time it takes for a parcel of gas to fall towards cluster core due to gravity alone is measured by its free-fall time, its infall time considers the environmental effects that may slow it down. The low velocities of molecular clouds found by ALMA show that the infall timescale is significantly longer than the free-fall timescale. In this model, a parcel of gas lifted by an X-ray bubble will have a significantly lower t_{cool}/t_I ratio in a higher altitude than t_{cool}/t_{ff} ratio in its original location, promoting thermal instability. ALMA observations have revealed evidence for outflowing and inflowing molecular gas returning to the galaxy centre. Russell et al. (2016b) observed the molecular gas in the BCG of PKS0745-191 to be distributed in three filaments extending 3-5 kpc in length, two of which are oriented toward the X-ray bubbles with the bulk of the molecular gas flowing outward. The molecular gas in NGC5044 (David et al., 2014) and A2597 (Tremblay et al., 2016) have been observed with narrow redshifted CO absorption lines indicating these clouds to be falling toward the cluster centre, and are possibly in the process of being accreted by the central black hole. These observations suggest that molecular clouds in BCGs that condensed in the wakes of

X-ray bubbles will sooner or later return to the galaxy centre in a circulating flow. In this model, we expect systems with CO emission to have X-ray cavities. In our sample, only 26 out of 35 systems detected with molecular gas are observed with X-ray cavities. However, there are many factors that makes it difficult to detect X-ray cavities such as low photon count, resolution and projection effects, and cavity detection techniques. For example, Dunn and Fabian (2006) reported X-ray cavities in A2029, but Shin et al. (2016) did not. The difference in their conclusion is due to the difference in the procedures they adopted to detect X-ray cavities. Dunn and Fabian (2006) used single exposures per target without combining all available exposures, and the β-modeling analysis performed by Shin et al. (2016) classified A2029 as false detection. On the other hand, among the 22 systems in our sample detected without CO emission, 15 of them are reported to have no X-ray cavities. However, five (4C+55.16, A2029, A2199, M87, RXJ0439.0+0520) out of the seven systems reported with X-ray cavities but observed without CO emission have central cooling time below the 1 Gyr threshold. In Section 3.1, such systems are observed to follow the same distribution of central cooling times as systems observed with molecular gas. That is, we suggest that molecular gas in these systems are likely missed due to the detection limit of the IRAM 30 telescope. With deeper CO and X-ray observations, stimulated feedback is a testable model.

An alternative model that includes the conceptually important thermal instability and uplift of ambient gas by galactic outflows is described in an analytical framework by Voit et al. (2016). In this model, there are two regions in which thermal instability can ensue to produce cold gas: a central isentropic region that extends out to where the minimum of the cooling to freefall ratio occurs and the region outside where the entropy of the hot gas is better described by a power-law. In the central isentropic region, the hot atmosphere is prone to cooling instabilities leading to gas condensation. Outside this region, low entropy gas need to be lifted to higher altitudes for cold gas condensation to occur, consistent with the stimulated feedback model (McNamara et al., 2016). Thus, this model implies an entropy profile described by a power law distribution approaching a constant entropy in the core.

In Figure 3.13, we plot the entropy profiles of 45 systems in our sample with cool cores – systems with central cooling times lower than 1 Gyr. If the thermodynamics of the ICM is only affected by gravitational processes associated with infalling gas, shock heating, and adiabatic compression, the entropy profile of clusters would exhibit a featureless power law in the form $K \propto R^{1.1}$ (Tozzi and Norman, 2001) where R denotes radius. This relation is overplotted as a green dashed line in Figure 3.13 and is consistent with the entropy profiles on large radii beyond the cluster core. Inside the cluster core, observations indicate that non-gravitational processes such as supernovae, stellar winds, AGN activity, and radiative

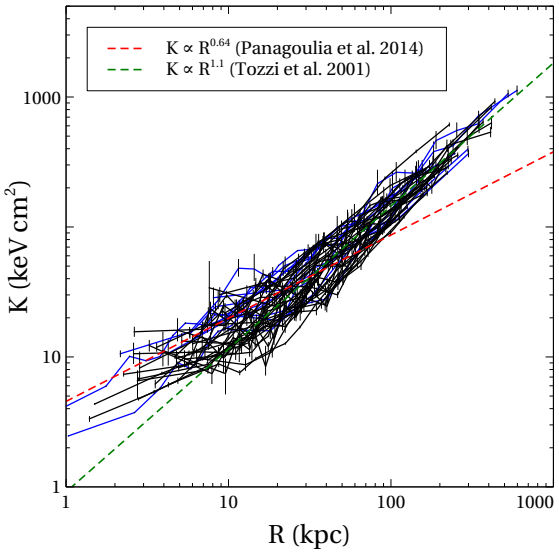

Figure 3.13: Deprojected entropy profiles of systems in our sample with cooling time at 10 kpc is less than 1 Gyr. Black symbols denote systems observed with CO emission while blue symbols denote non-detection.

cooling results in an excess entropy with respect to that produced by purely gravitational processes. This excess entropy has been reported to take the form of an "entropy floor" (David et al., 1996; Ponman et al., 2003; Morandi and Ettori, 2007; Cavagnolo et al., 2009; Voit et al., 2016). On the other hand, a number of studies have reported not finding evidence for such a floor at radii as small as ∼1 kpc from the cluster centre (McCarthy et al., 2004; Piffaretti et al., 2005; Pratt et al., 2006; Panagoulia et al., 2014a). The radial profile of the entropy becomes less steep ($K \propto R^{0.64}$) in the core, but does not approach a minimum entropy (Panagoulia et al., 2014a). This relation is overplotted in Figure 3.13 as a red dashed line. In general, this is relation is consistent with the entropy profiles in the figure within ∼10 kpc from the cluster centre. While a few of our entropy profiles may exhibit an apparent flattening in the cluster centre, such flattening may be brought about by observational effects discussed by Panagoulia et al. (2014a) such as: resolution effects where large central spectral bin leads to a higher measured central entropy, not taking into account deprojection effects, and the presence of a complex temperature structure in the core where a two-temperature model as oppose to a single-temperature model may be more appropriate. Consistent with the entropy profiles of a sample of clusters with Hα emission in Hogan et al. (2017), our entropy profiles are best described by a double power law.

Chapter 4

Conclusion

We have presented an analysis of 55 giant elliptical galaxies centrally located in galaxy clusters to investigate the origin of molecular gas found in these massive galaxies. Our work focuses mainly on IRAM CO and Chandra X-ray observation data; nevertheless, we have also utilized NVSS L-band fluxes and obtained Hα and IR data from literature, which allows us to study the connection between cold gas, the intracluster medium, and the central active galactic nucleus. In this chapter, we summarize our main results.

4.1 Summary

Understanding the origin of cold gas in giant elliptical galaxies is important for our understanding of galaxy evolution and AGN feedback loop. Molecular gas makes up the bulk of cold gas found in these massive galaxies. CO line emission is the most accessible and widely used tracer of molecular gas.

We show that the detection of CO emission, indicative of the presence of molecular gas, depends critically on the presence of gas with short cooling time or low entropy. Molecular gas is preferentially observed in the BCGs in our sample with central ICM cooling times below a threshold of $\sim$1 Gyr or with central entropies below $\sim$35 keV cm^2. The equivalent threshold for the cooling to free-fall time ratio found for our sample is $\min(t_{cool}/t_{ff}) \lesssim 25$. These thresholds point to the cooling of the hot intracluster atmosphere as the origin of molecular gas in giant elliptical galaxies centrally located in galaxy clusters. Under this framework, when the atmosphere becomes thermally unstable, overdense blobs formed by perturbations cool to low temperatures ($< 10^4$ K), decouple from the hot atmosphere, and

may form stars or molecular gas (Cowie et al., 1980; Nulsen, 1986; Pizzolato and Soker, 2005).

We do not find evidence for the "hysteresis effect" implied in existing precipitation models. In these models, cold gas condenses out of the hot atmosphere when $\min(t_{cool}/t_{ff})$ falls below $\sim$10 and a fraction of it fuels the AGN. The AGN releases strong jets that overheats the surrounding atmosphere such that $\min(t_{cool}/t_{ff}) \gtrsim 10$. This slows down the accretion rate of the SMBH as the AGN injects heat back to the atmosphere suppressing the condensation of cold gas. As shown in Figure 3.9, this cycle of overheating and cooling characterized by large swings in central density and cooling time is not evident in our sample of BCGs. For a wide range (five decades) of AGN mechanical power released into the hot atmosphere, we observe a narrow range of roughly a decade of scatter in the central gas densities and cooling times of our sample. The AGN favors a relatively gentle and self-regulated AGN feedback, rather than one that is sudden and violent (Bîrzan et al., 2012; Panagoulia et al., 2014b).

As accretion from the hot phase is generally unable to fuel powerful AGNs, several studies have highlighted the importance of cold mode accretion in forming a feedback loop that connects the cooling by-products of the ICM with AGN outbursts (Pizzolato and Soker, 2005; Gaspari et al., 2012; Li and Bryan, 2014). However, we do not find a correlation between molecular gas mass and AGN mechanical power for our sample of BCGs. This is consistent with the observations of McNamara et al. (2011) and simulations of Prasad et al. (2015). If most of the molecular gas in BCGs is consumed by star formation, then we find a depletion timescale of $\sim$1 Gyr implying that molecular clouds in BCGs are long-lived. This is inconsistent with the dynamically young ages of molecular clouds observed in a small but growing sample of BCGs with ALMA (David et al., 2014; McNamara et al., 2014; Russell et al., 2014, 2016a,b; Vantyghem et al., 2016; Tremblay et al., 2016).

In conclusion, our results point to thermal instability in the hot atmosphere as the origin of molecular gas in giant elliptical galaxies centrally located in clusters of galaxies.

4.2 Future Work

It is clear from this work that multi-wavelength observation of cluster cores can improve our understanding of AGN feedback. Several interesting topics can be explored by continuing this work which we discuss below.

We have provided evidence for the origin of molecular gas mass to be a result of cooling from the hot atmosphere via thermal instability. One such piece of evidence is the

prevalence of systems detected with CO emission when their central cooling falls below $\sim$1 Gyr. It is unfortunate that there are few data points in our plots with cooling times greater than 1 Gyr. Only 12 out 55 of such objects can be found in our sample. This work can be improved by extending the study sample such that there are roughly equal number of systems on either side of the $\sim$1 Gyr cooling time threshold. Deeper CO observations probing the area below the CO(1-0) limit of IRAM as shown in right panel of Figure 3.3 would also be an interesting extension to the study sample.

The outlier A1060 to the cooling time threshold of $\sim$1 Gyr is interesting. It harbors molecular gas mass that is low relative to those found in BCGs, but typical of normal elliptical galaxies. An intriguing project would be to perform the same analysis done on this work to normal elliptical galaxies.

A small list of BCGs have been observed using ALMA resolving the spatial and velocity structure of their molecular clouds (David et al., 2014; McNamara et al., 2014; Russell et al., 2014, 2016a,b; Vantyghem et al., 2016; Tremblay et al., 2016). While a number of important and surprising discoveries have been revealed individually be these studies, a sufficiently large sample where an analysis is performed similar to this work would be interesting.

Bibliography

Allen, S. W., Dunn, R. J. H., Fabian, A. C., Taylor, G. B., and Reynolds, C. S. (2006). The relation between accretion rate and jet power in X-ray luminous elliptical galaxies. *mnras*, 372:21–30.

Anders, E. and Grevesse, N. (1989). Abundances of the elements - Meteoritic and solar. *gca*, 53:197–214.

Arnaud, K. A. (1996). XSPEC: The First Ten Years. In Jacoby, G. H. and Barnes, J., editors, *Astronomical Data Analysis Software and Systems V*, volume 101 of *Astronomical Society of the Pacific Conference Series*, page 17.

Baldry, I. K., Glazebrook, K., Brinkmann, J., Ivezić, Ž., Lupton, R. H., Nichol, R. C., and Szalay, A. S. (2004). Quantifying the Bimodal Color-Magnitude Distribution of Galaxies. *apj*, 600:681–694.

Balucinska-Church, M. and McCammon, D. (1994). VizieR Online Data Catalog: Photoelectric absorption cross-sections (Balucinska-Church+, 1992). *VizieR Online Data Catalog*, 6062.

Bell, E. F. (2003). Estimating Star Formation Rates from Infrared and Radio Luminosities: The Origin of the Radio-Infrared Correlation. *apj*, 586:794–813.

Bell, E. F. and de Jong, R. S. (2001). Stellar Mass-to-Light Ratios and the Tully-Fisher Relation. *apj*, 550:212–229.

Bell, E. F., McIntosh, D. H., Katz, N., and Weinberg, M. D. (2003). The Optical and Near-Infrared Properties of Galaxies. I. Luminosity and Stellar Mass Functions. *apjs*, 149:289–312.

Best, P. N., von der Linden, A., Kauffmann, G., Heckman, T. M., and Kaiser, C. R. (2007). On the prevalence of radio-loud active galactic nuclei in brightest cluster galaxies: implications for AGN heating of cooling flows. *mnras*, 379:894–908.

Bîrzan, L., McNamara, B. R., Nulsen, P. E. J., Carilli, C. L., and Wise, M. W. (2008). Radiative Efficiency and Content of Extragalactic Radio Sources: Toward a Universal Scaling Relation between Jet Power and Radio Power. *apj*, 686:859–880.

Bîrzan, L., Rafferty, D. A., McNamara, B. R., Wise, M. W., and Nulsen, P. E. J. (2004). A Systematic Study of Radio-induced X-Ray Cavities in Clusters, Groups, and Galaxies. *apj*, 607:800–809.

Bîrzan, L., Rafferty, D. A., Nulsen, P. E. J., McNamara, B. R., Röttgering, H. J. A., Wise, M. W., and Mittal, R. (2012). The duty cycle of radio-mode feedback in complete samples of clusters. *mnras*, 427:3468–3488.

Boehringer, H., Voges, W., Fabian, A. C., Edge, A. C., and Neumann, D. M. (1993). A ROSAT HRI study of the interaction of the X-ray-emitting gas and radio lobes of NGC 1275. *mnras*, 264:L25–L28.

Böhringer, H., Pratt, G. W., Finoguenov, A., and Schuecker, P., editors (2007). *Heating versus Cooling in Galaxies and Clusters of Galaxies*.

Bolatto, A. D., Wolfire, M., and Leroy, A. K. (2013). The CO-to-H_2 Conversion Factor. *araa*, 51:207–268.

Braine, J. and Dupraz, C. (1994). Deep CO observations of dominant cluster galaxies with reported cooling flows. *aap*, 283:407–416.

Bregman, J. N., Fabian, A. C., Miller, E. D., and Irwin, J. A. (2006). On VI Observations of Galaxy Clusters: Evidence for Modest Cooling Flows. *apj*, 642:746–751.

Bregman, J. N. and Hogg, D. E. (1988). A search for CO emission in cooling flows. *aj*, 96:455–457.

Canning, R. E. A., Sun, M., Sanders, J. S., Clarke, T. E., Fabian, A. C., Giacintucci, S., Lal, D. V., Werner, N., Allen, S. W., Donahue, M., Edge, A. C., Johnstone, R. M., Nulsen, P. E. J., Salomé, P., and Sarazin, C. L. (2013). A multiwavelength view of cooling versus AGN heating in the X-ray luminous cool-core of Abell 3581. *mnras*, 435:1108–1125.

Carilli, C. L., Perley, R. A., and Harris, D. E. (1994). Observations of Interaction Between Cluster Gas and the Radio Lobes of Cygnus-A. *mnras*, 270:173.

Cavagnolo, K. W., Donahue, M., Voit, G. M., and Sun, M. (2008). An Entropy Threshold for Strong Hα and Radio Emission in the Cores of Galaxy Clusters. *apjl*, 683:L107.

Cavagnolo, K. W., Donahue, M., Voit, G. M., and Sun, M. (2009). Intracluster Medium Entropy Profiles for a Chandra Archival Sample of Galaxy Clusters. *apjs*, 182:12–32.

Cavagnolo, K. W., McNamara, B. R., Nulsen, P. E. J., Carilli, C. L., Jones, C., and Bîrzan, L. (2010). A Relationship Between AGN Jet Power and Radio Power. *apj*, 720:1066–1072.

Condon, J. J., Cotton, W. D., Greisen, E. W., Yin, Q. F., Perley, R. A., Taylor, G. B., and Broderick, J. J. (2002). VizieR Online Data Catalog: 1.4GHz NRAO VLA Sky Survey (NVSS) (Condon+ 1998). *VizieR Online Data Catalog*, 8065.

Cowie, L. L., Fabian, A. C., and Nulsen, P. E. J. (1980). NGC 1275 and the Perseus cluster - The formation of optical filaments in cooling gas in X-ray clusters. *mnras*, 191:399–410.

Crawford, C. S., Allen, S. W., Ebeling, H., Edge, A. C., and Fabian, A. C. (1999). The ROSAT Brightest Cluster Sample - III. Optical spectra of the central cluster galaxies. *mnras*, 306:857–896.

Crawford, C. S., Hatch, N. A., Fabian, A. C., and Sanders, J. S. (2005). The extended Hα-emitting filaments surrounding NGC 4696, the central galaxy of the Centaurus cluster. *mnras*, 363:216–222.

David, L. P., Jones, C., and Forman, W. (1996). ROSAT PSPC Observations of Cool Rich Clusters. *apj*, 473:692.

David, L. P., Lim, J., Forman, W., Vrtilek, J., Combes, F., Salome, P., Edge, A., Hamer, S., Jones, C., Sun, M., O'Sullivan, E., Gastaldello, F., Bardelli, S., Temi, P., Schmitt, H., Ohyama, Y., Mathews, W., Brighenti, F., Giacintucci, S., and Trung, D.-V. (2014). Molecular Gas in the X-Ray Bright Group NGC 5044 as Revealed by ALMA. *apj*, 792:94.

Donahue, M., Horner, D. J., Cavagnolo, K. W., and Voit, G. M. (2006). Entropy Profiles in the Cores of Cooling Flow Clusters of Galaxies. *apj*, 643:730–750.

Dunn, R. J. H. and Fabian, A. C. (2006). Investigating AGN heating in a sample of nearby clusters. *mnras*, 373:959–971.

Dunn, R. J. H., Fabian, A. C., and Taylor, G. B. (2005). Radio bubbles in clusters of galaxies. *mnras*, 364:1343–1353.

Edge, A. C. (2001). The detection of molecular gas in the central galaxies of cooling flow clusters. *mnras*, 328:762–782.

Edge, A. C. and Frayer, D. T. (2003). Resolving Molecular gas in the Central Galaxies of Cooling Flow Clusters. *apjl*, 594:L13–L17.

Edge, A. C., Wilman, R. J., Johnstone, R. M., Crawford, C. S., Fabian, A. C., and Allen, S. W. (2002). A survey of molecular hydrogen in the central galaxies of cooling flows. *mnras*, 337:49–62.

Egami, E., Misselt, K. A., Rieke, G. H., Wise, M. W., Neugebauer, G., Kneib, J.-P., Le Floc'h, E., Smith, G. P., Blaylock, M., Dole, H., Frayer, D. T., Huang, J.-S., Krause, O., Papovich, C., Pérez-González, P. G., and Rigby, J. R. (2006). Spitzer Observations of the Brightest Galaxies in X-Ray-Luminous Clusters. *apj*, 647:922–933.

Faber, S. M., Willmer, C. N. A., Wolf, C., Koo, D. C., Weiner, B. J., Newman, J. A., Im, M., Coil, A. L., Conroy, C., Cooper, M. C., Davis, M., Finkbeiner, D. P., Gerke, B. F., Gebhardt, K., Groth, E. J., Guhathakurta, P., Harker, J., Kaiser, N., Kassin, S., Kleinheinrich, M., Konidaris, N. P., Kron, R. G., Lin, L., Luppino, G., Madgwick, D. S., Meisenheimer, K., Noeske, K. G., Phillips, A. C., Sarajedini, V. L., Schiavon, R. P., Simard, L., Szalay, A. S., Vogt, N. P., and Yan, R. (2007). Galaxy Luminosity Functions to z˜1 from DEEP2 and COMBO-17: Implications for Red Galaxy Formation. *apj*, 665:265–294.

Fabian, A. C. (1994). Cluster cooling flows. In Seitter, W. C., editor, *NATO Advanced Science Institutes (ASI) Series C*, volume 441 of *NATO Advanced Science Institutes (ASI) Series C*, pages 163–182.

Fabian, A. C. (2012). Observational Evidence of Active Galactic Nuclei Feedback. *araa*, 50:455–489.

Fisher, D., Illingworth, G., and Franx, M. (1995). Kinematics of 13 brightest cluster galaxies. *apj*, 438:539–562.

Freeman, P. E., Kashyap, V., Rosner, R., and Lamb, D. Q. (2002). A Wavelet-Based Algorithm for the Spatial Analysis of Poisson Data. *apjs*, 138:185–218.

Fujita, Y., Tosaki, T., Nakamichi, A., and Kuno, N. (2000). CO (J = 1-0) Observation of the cD Galaxy of AWM 7: Constraints on the Evaporation of Molecular Gas. *pasj*, 52:235.

Gaspari, M., Ruszkowski, M., and Oh, S. P. (2013). Chaotic cold accretion on to black holes. *mnras*, 432:3401–3422.

Gaspari, M., Ruszkowski, M., and Sharma, P. (2012). Cause and Effect of Feedback: Multiphase Gas in Cluster Cores Heated by AGN Jets. *apj*, 746:94.

George, M. R., Leauthaud, A., Bundy, K., Finoguenov, A., Ma, C.-P., Rykoff, E. S., Tinker, J. L., Wechsler, R. H., Massey, R., and Mei, S. (2012). Galaxies in X-Ray Groups. II. A Weak Lensing Study of Halo Centering. *apj*, 757:2.

Gitti, M., McNamara, B. R., Nulsen, P. E. J., and Wise, M. W. (2007). Cosmological Effects of Powerful AGN Outbursts in Galaxy Clusters: Insights from an XMM-Newton Observation of MS 0735+7421. *apj*, 660:1118–1136.

Grabelsky, D. A. and Ulmer, M. P. (1990). Search for cold gas in clusters with and without cooling flows. *apj*, 355:401–409.

Gursky, H., Solinger, A., Kellogg, E. M., Murray, S., Tananbaum, H., Giacconi, R., and Cavaliere, A. (1972). X-Ray Emission from Rich Clusters of Galaxies. *apjl*, 173:L99.

Hamer, S. L., Edge, A. C., Swinbank, A. M., Oonk, J. B. R., Mittal, R., McNamara, B. R., Russell, H. R., Bremer, M. N., Combes, F., Fabian, A. C., Nesvadba, N. P. H., O'Dea, C. P., Baum, S. A., Salomé, P., Tremblay, G., Donahue, M., Ferland, G. J., and Sarazin, C. L. (2014). Cold gas dynamics in Hydra-A: evidence for a rotating disc. *mnras*, 437:862–878.

Hardcastle, M. J., Evans, D. A., and Croston, J. H. (2007). Hot and cold gas accretion and feedback in radio-loud active galaxies. *mnras*, 376:1849–1856.

Hatch, N. A., Crawford, C. S., and Fabian, A. C. (2007). Ionized nebulae surrounding brightest cluster galaxies. *mnras*, 380:33–43.

Hlavacek-Larrondo, J., Allen, S. W., Taylor, G. B., Fabian, A. C., Canning, R. E. A., Werner, N., Sanders, J. S., Grimes, C. K., Ehlert, S., and von der Linden, A. (2013). Probing the Extreme Realm of Active Galactic Nucleus Feedback in the Massive Galaxy Cluster, RX J1532.9+3021. *apj*, 777:163.

Hogan, M. T., Edge, A. C., Hlavacek-Larrondo, J., Grainge, K. J. B., Hamer, S. L., Mahony, E. K., Russell, H. R., Fabian, A. C., McNamara, B. R., and Wilman, R. J. (2015). A comprehensive study of the radio properties of brightest cluster galaxies. *mnras*, 453:1201–1222.

Hogan, M. T., McNamara, B. R., and et al. (2017). An Observational Study into Gas Condensation From The Hot-Phase In Cool-Core Clusters.

Hogan, M. T., McNamara, B. R., Pulido, F., Nulsen, P. E. J., Russell, H. R., Vantyghem, A. N., Edge, A. C., and Main, R. A. (2016). Mass Distribution in Galaxy Cluster Cores. *ArXiv e-prints*.

Hopkins, A. M. and Beacom, J. F. (2006). On the Normalization of the Cosmic Star Formation History. *apj*, 651:142–154.

Hu, E. M., Cowie, L. L., and Wang, Z. (1985). Long-slit spectroscopy of gas in the cores of X-ray luminous clusters. *apjs*, 59:447–498.

Hudson, D. S., Mittal, R., Reiprich, T. H., Nulsen, P. E. J., Andernach, H., and Sarazin, C. L. (2010). What is a cool-core cluster? a detailed analysis of the cores of the X-ray flux-limited HIFLUGCS cluster sample. *aap*, 513:A37.

Jaffe, W. (1987). Limits on the cool gas content of NGC 1275 and M 87. *aap*, 171:378.

Jaffe, W., Bremer, M. N., and Baker, K. (2005). HII and H_2 in the envelopes of cooling flow central galaxies. *mnras*, 360:748–762.

Johnstone, R. M., Fabian, A. C., and Nulsen, P. E. J. (1987). The optical spectra of central galaxies in southern clusters Evidence for star formation. *mnras*, 224:75–91.

Johnstone, R. M., Hatch, N. A., Ferland, G. J., Fabian, A. C., Crawford, C. S., and Wilman, R. J. (2007). Discovery of atomic and molecular mid-infrared emission lines in off-nuclear regions of NGC 1275 and NGC4696 with the Spitzer Space Telescope. *mnras*, 382:1246–1260.

Kaastra, J. S. (2015). Atomic processes in optically thin plasmas. *IAU General Assembly*, 22:2249812.

Kalberla, P. M. W., Burton, W. B., Hartmann, D., Arnal, E. M., Bajaja, E., Morras, R., and Pöppel, W. G. L. (2005). The Leiden/Argentine/Bonn (LAB) Survey of Galactic HI. Final data release of the combined LDS and IAR surveys with improved stray-radiation corrections. *aap*, 440:775–782.

Kennicutt, R. C. and Evans, N. J. (2012). Star Formation in the Milky Way and Nearby Galaxies. *araa*, 50:531–608.

Kennicutt, Jr., R. C. (1998a). Star Formation in Galaxies Along the Hubble Sequence. *araa*, 36:189–232.

Kennicutt, Jr., R. C. (1998b). The Global Schmidt Law in Star-forming Galaxies. *apj*, 498:541–552.

Kewley, L. J., Geller, M. J., Jansen, R. A., and Dopita, M. A. (2002). The Hα and Infrared Star Formation Rates for the Nearby Field Galaxy Survey. *aj*, 124:3135–3143.

Kirkpatrick, C. C., McNamara, B. R., Rafferty, D. A., Nulsen, P. E. J., Bîrzan, L., Kazemzadeh, F., Wise, M. W., Gitti, M., and Cavagnolo, K. W. (2009). A Chandra X-Ray Analysis of Abell 1664: Cooling, Feedback, and Star Formation in the Central Cluster Galaxy. *apj*, 697:867–879.

Kormendy, J. and Bender, R. (1996). A Proposed Revision of the Hubble Sequence for Elliptical Galaxies. *apjl*, 464:L119.

Laganá, T. F., Lovisari, L., Martins, L., Lanfranchi, G. A., Capelato, H. V., and Schellenberger, G. (2015). A metal-rich elongated structure in the core of the group NGC 4325. *aap*, 573:A66.

Lakhchaura, K., Saini, T. D., and Sharma, P. (2016). Decoding X-ray observations from centres of galaxy clusters using MCMC. *mnras*, 460:2625–2647.

Lauer, T. R., Postman, M., Strauss, M. A., Graves, G. J., and Chisari, N. E. (2014). Brightest Cluster Galaxies at the Present Epoch. *apj*, 797:82.

Lazareff, B., Castets, A., Kim, D.-W., and Jura, M. (1989). Discovery of CO emission from NGC 1275. *apjl*, 336:L13–L15.

Lees, J. F., Knapp, G. R., Rupen, M. P., and Phillips, T. G. (1991). Molecular gas in elliptical galaxies. *apj*, 379:177–215.

Leroy, A. K., Walter, F., Brinks, E., Bigiel, F., de Blok, W. J. G., Madore, B., and Thornley, M. D. (2008). The Star Formation Efficiency in Nearby Galaxies: Measuring Where Gas Forms Stars Effectively. *aj*, 136:2782–2845.

Li, Y. and Bryan, G. L. (2012). Simulating the Cooling Flow of Cool-core Clusters. *apj*, 747:26.

Li, Y. and Bryan, G. L. (2014). Modeling Active Galactic Nucleus Feedback in Cool-core Clusters: The Balance between Heating and Cooling. *apj*, 789:54.

Li, Y., Bryan, G. L., Ruszkowski, M., Voit, G. M., O'Shea, B. W., and Donahue, M. (2015). Cooling, AGN Feedback, and Star Formation in Simulated Cool-core Galaxy Clusters. *apj*, 811:73.

Liedahl, D. A., Osterheld, A. L., and Goldstein, W. H. (1995). New calculations of Fe L-shell X-ray spectra in high-temperature plasmas. *apjl*, 438:L115–L118.

Lim, J., Ao, Y., and Dinh-V-Trung (2008). Radially Inflowing Molecular Gas in NGC 1275 Deposited by an X-Ray Cooling Flow in the Perseus Cluster. *apj*, 672:252–265.

Lim, J., Leon, S., Combes, F., and Dinh-V-Trung (2000). Molecular Gas in the Powerful Radio Galaxies 3C 31 and 3C 264: Major or Minor Mergers? *apjl*, 545:L93–L97.

Main, R., McNamara, B., Nulsen, P., Russell, H., and Vantyghem, A. (2015). AGN Feedback, Host Halo Mass and Central Cooling Time: Implications for Galaxy Formation Efficiency and $M\_BH - \sigma$. *ArXiv e-prints*.

Maller, A. H., Berlind, A. A., Blanton, M. R., and Hogg, D. W. (2009). The Intrinsic Properties of SDSS Galaxies. *apj*, 691:394–406.

Mannucci, F., Basile, F., Poggianti, B. M., Cimatti, A., Daddi, E., Pozzetti, L., and Vanzi, L. (2001). Near-infrared template spectra of normal galaxies: k-corrections, galaxy models and stellar populations. *mnras*, 326:745–758.

Mathews, W. G. and Brighenti, F. (2003). Hot Gas in and around Elliptical Galaxies. *araa*, 41:191–239.

Mathews, W. G., Faltenbacher, A., and Brighenti, F. (2006). Heating Cooling Flows with Weak Shock Waves. *apj*, 638:659–667.

McCarthy, I. G., Balogh, M. L., Babul, A., Poole, G. B., and Horner, D. J. (2004). Models of the Intracluster Medium with Heating and Cooling: Explaining the Global and Structural X-Ray Properties of Clusters. *apj*, 613:811–830.

McCourt, M., Sharma, P., Quataert, E., and Parrish, I. J. (2012). Thermal instability in gravitationally stratified plasmas: implications for multiphase structure in clusters and galaxy haloes. *mnras*, 419:3319–3337.

McDonald, M., Veilleux, S., Rupke, D. S. N., and Mushotzky, R. (2010). On the Origin of the Extended Hα Filaments in Cooling Flow Clusters. *apj*, 721:1262–1283.

McNamara, B. R. and Jaffe, W. (1994). Sensitive limits on the molecular gas content of cluster cooling flows. *aap*, 281:673–680.

McNamara, B. R. and Nulsen, P. E. J. (2007a). Heating Hot Atmospheres with Active Galactic Nuclei. *araa*, 45:117–175.

McNamara, B. R. and Nulsen, P. E. J. (2007b). Heating Hot Atmospheres with Active Galactic Nuclei. *araa*, 45:117–175.

McNamara, B. R. and Nulsen, P. E. J. (2012). Mechanical feedback from active galactic nuclei in galaxies, groups and clusters. *New Journal of Physics*, 14(5):055023.

McNamara, B. R. and O'Connell, R. W. (1989). Star formation in cooling flows in clusters of galaxies. *aj*, 98:2018–2043.

McNamara, B. R. and O'Connell, R. W. (1992). Color gradients in cooling flows in clusters of galaxies. *apj*, 393:579–610.

McNamara, B. R., Rohanizadegan, M., and Nulsen, P. E. J. (2011). Are Radio Active Galactic Nuclei Powered by Accretion or Black Hole Spin? *apj*, 727:39.

McNamara, B. R., Russell, H. R., Nulsen, P. E. J., Edge, A. C., Murray, N. W., Main, R. A., Vantyghem, A. N., Combes, F., Fabian, A. C., Salome, P., Kirkpatrick, C. C., Baum, S. A., Bregman, J. N., Donahue, M., Egami, E., Hamer, S., O'Dea, C. P., Oonk, J. B. R., Tremblay, G., and Voit, G. M. (2014). A 10^{10} Solar Mass Flow of Molecular Gas in the A1835 Brightest Cluster Galaxy. *apj*, 785:44.

McNamara, B. R., Russell, H. R., Nulsen, P. E. J., Hogan, M. T., Fabian, A. C., Pulido, F., and Edge, A. C. (2016). A Mechanism for Stimulating AGN Feedback by Lifting Gas in Massive Galaxies. *apj*, 830:79.

McNamara, B. R., Wise, M., Nulsen, P. E. J., David, L. P., Sarazin, C. L., Bautz, M., Markevitch, M., Vikhlinin, A., Forman, W. R., Jones, C., and Harris, D. E. (2000). Chandra X-Ray Observations of the Hydra A Cluster: An Interaction between the Radio Source and the X-Ray-emitting Gas. *apjl*, 534:L135–L138.

Mewe, R., Gronenschild, E. H. B. M., and van den Oord, G. H. J. (1985). Calculated X-radiation from optically thin plasmas. V. *aaps*, 62:197–254.

Mewe, R., Lemen, J. R., and van den Oord, G. H. J. (1986). Calculated X-radiation from optically thin plasmas. VI - Improved calculations for continuum emission and approximation formulae for nonrelativistic average Gaunt factors. *aaps*, 65:511–536.

Mirabel, I. F., Sanders, D. B., and Kazes, I. (1989). Molecular gas in the powerful radio galaxies Perseus A and 4C 12.50. *apjl*, 340:L9–L12.

Mittal, R., Hudson, D. S., Reiprich, T. H., and Clarke, T. (2009). AGN heating and ICM cooling in the HIFLUGCS sample of galaxy clusters. *aap*, 501:835–850.

Morandi, A. and Ettori, S. (2007). Entropy profiles in X-ray luminous galaxy clusters at z ¿ 0.1. *mnras*, 380:1521–1532.

Morris, K. A. and et al. (2017). What is Hysteresis. *ASME Applied Mechanics Reviews*.

Mushotzky, R. F. and Loewenstein, M. (1997). Lack of Evolution in the Iron Abundance in Clusters of Galaxies and Implications for the Global Star Formation Rate at High Redshift. *apjl*, 481:L63–L66.

Mushotzky, R. F., Serlemitsos, P. J., Boldt, E. A., Holt, S. S., and Smith, B. W. (1978). OSO 8 X-ray spectra of clusters of galaxies. I - Observations of twenty clusters: Physical correlations. *apj*, 225:21–39.

Navarro, J. F., Frenk, C. S., and White, S. D. M. (1997). A Universal Density Profile from Hierarchical Clustering. *apj*, 490:493–508.

Nulsen, P. E. J. (1986). Thermal instability in cooling flows. *mnras*, 221:377–392.

Nulsen, P. E. J., Powell, S. L., and Vikhlinin, A. (2010). Model-independent X-ray Mass Determinations. *apj*, 722:55–64.

Ocaña Flaquer, B., Leon, S., Combes, F., and Lim, J. (2010). TANGO I: Interstellar medium in nearby radio galaxies. Molecular gas. *aap*, 518:A9.

O'Dea, C. P., Baum, S. A., Maloney, P. R., Tacconi, L. J., and Sparks, W. B. (1994). Constraints on molecular gas in cooling flows and powerful radio galaxies. *apj*, 422:467–479.

O'Dea, C. P., Baum, S. A., Privon, G., Noel-Storr, J., Quillen, A. C., Zufelt, N., Park, J., Edge, A., Russell, H., Fabian, A. C., Donahue, M., Sarazin, C. L., McNamara, B., Bregman, J. N., and Egami, E. (2008). An Infrared Survey of Brightest Cluster Galaxies. II. Why are Some Brightest Cluster Galaxies Forming Stars? *apj*, 681:1035–1045.

O'Dea, C. P., Payne, H. E., and Kocevski, D. (1998). An Arecibo Search for Broad 21 Centimeter Lines of Atomic Hydrogen in Clusters of Galaxies. *aj*, 116:623–633.

Okabe, N., Umetsu, K., Tamura, T., Fujita, Y., Takizawa, M., Matsushita, K., Fukazawa, Y., Futamase, T., Kawaharada, M., Miyazaki, S., Mochizuki, Y., Nakazawa, K., Ohashi, T., Ota, N., Sasaki, T., Sato, K., and Tam, S. (2015). Central Mass Profiles of the Nearby Cool-core Galaxy Clusters Hydra A and A478 (preprint).

Okuda, T., Kohno, K., Iguchi, S., and Nakanishi, K. (2005). Rotating Molecular Gas Associated with a Silhouette Disk at the Center of the Radio Galaxy 3C 31. *apj*, 620:673–679.

Oonk, J. B. R., Jaffe, W., Bremer, M. N., and van Weeren, R. J. (2010). The distribution and condition of the warm molecular gas in Abell 2597 and Sersic 159-03. *mnras*, 405:898–932.

Panagoulia, E. K., Fabian, A. C., and Sanders, J. S. (2014a). A volume-limited sample of X-ray galaxy groups and clusters - I. Radial entropy and cooling time profiles. *mnras*, 438:2341–2354.

Panagoulia, E. K., Fabian, A. C., Sanders, J. S., and Hlavacek-Larrondo, J. (2014b). A volume-limited sample of X-ray galaxy groups and clusters - II. X-ray cavity dynamics. *mnras*, 444:1236–1259.

Pandge, M. B., Vagshette, N. D., Sonkamble, S. S., and Patil, M. K. (2013). Investigation of X-ray cavities in the cooling flow system Abell 1991. *apss*, 345:183–193.

Peterson, J. R., Kahn, S. M., Paerels, F. B. S., Kaastra, J. S., Tamura, T., Bleeker, J. A. M., Ferrigno, C., and Jernigan, J. G. (2003). High-Resolution X-Ray Spectroscopic Constraints on Cooling-Flow Models for Clusters of Galaxies. *apj*, 590:207–224.

Pfrommer, C. and Enßlin, T. A. (2003). Probing the cosmic ray population of the giant elliptical galaxy M 87 with observed TeV gamma -rays. *aap*, 407:L73–L77.

Piffaretti, R., Jetzer, P., Kaastra, J. S., and Tamura, T. (2005). Temperature and entropy profiles of nearby cooling flow clusters observed with XMM-Newton. *aap*, 433:101–111.

Pizzolato, F. and Soker, N. (2005). On the Nature of Feedback Heating in Cooling Flow Clusters. *apj*, 632:821–830.

Poggianti, B. M. (1997). K and evolutionary corrections from UV to IR. *aaps*, 122.

Pointecouteau, E., Arnaud, M., and Pratt, G. W. (2005). The structural and scaling properties of nearby galaxy clusters. I. The universal mass profile. *aap*, 435:1–7.

Ponman, T. J., Helsdon, S. F., and Finoguenov, A. (1999). The Impact of Galaxy Evolution on Galaxy Systems. In Giuricin, G., Mezzetti, M., and Salucci, P., editors, *Observational Cosmology: The Development of Galaxy Systems*, volume 176 of *Astronomical Society of the Pacific Conference Series*, page 64.

Ponman, T. J., Sanderson, A. J. R., and Finoguenov, A. (2003). The Birmingham-CfA cluster scaling project - III. Entropy and similarity in galaxy systems. *mnras*, 343:331–342.

Prasad, D., Sharma, P., and Babul, A. (2015). Cool Core Cycles: Cold Gas and AGN Jet Feedback in Cluster Cores. *apj*, 811:108.

Pratt, G. W., Arnaud, M., and Pointecouteau, E. (2006). Structure and scaling of the entropy in nearby galaxy clusters. *aap*, 446:429–438.

Rafferty, D. A., McNamara, B. R., and Nulsen, P. E. J. (2008). The Regulation of Cooling and Star Formation in Luminous Galaxies by Active Galactic Nucleus Feedback and the Cooling-Time/Entropy Threshold for the Onset of Star Formation. *apj*, 687:899–918.

Rafferty, D. A., McNamara, B. R., Nulsen, P. E. J., and Wise, M. W. (2006). The Feedback-regulated Growth of Black Holes and Bulges through Gas Accretion and Starbursts in Cluster Central Dominant Galaxies. *apj*, 652:216–231.

Read, J. I. and Trentham, N. (2005). The baryonic mass function of galaxies. *Philosophical Transactions of the Royal Society of London Series A*, 363.

Russell, H. R., Fabian, A. C., Sanders, J. S., Johnstone, R. M., Blundell, K. M., Brandt, W. N., and Crawford, C. S. (2010). The X-ray luminous cluster underlying the bright radio-quiet quasar H1821+643. *mnras*, 402:1561–1579.

Russell, H. R., McDonald, M., McNamara, B. R., Fabian, A. C., Nulsen, P. E. J., Bayliss, M. B., Benson, B. A., Brodwin, M., Carlstrom, J. E., Edge, A. C., Hlavacek-Larrondo, J., Marrone, D. P., Reichardt, C. L., and Vieira, J. D. (2016a). ALMA observations of massive molecular gas filaments encasing radio bubbles in the Phoenix cluster. *ArXiv e-prints*.

Russell, H. R., McNamara, B. R., Edge, A. C., Nulsen, P. E. J., Main, R. A., Vantyghem, A. N., Combes, F., Fabian, A. C., Murray, N., Salomé, P., Wilman, R. J., Baum, S. A., Donahue, M., O'Dea, C. P., Oonk, J. B. R., Tremblay, G. R., and Voit, G. M. (2014). Massive Molecular Gas Flows in the A1664 Brightest Cluster Galaxy. *apj*, 784:78.

Russell, H. R., McNamara, B. R., Fabian, A. C., Nulsen, P. E. J., Edge, A. C., Combes, F., Murray, N. W., Parrish, I. J., Salomé, P., Sanders, J. S., Baum, S. A., Donahue, M., Main, R. A., O'Connell, R. W., O'Dea, C. P., Oonk, J. B. R., Tremblay, G., Vantyghem, A. N., and Voit, G. M. (2016b). ALMA observations of cold molecular gas filaments trailing rising radio bubbles in PKS 0745-191. *mnras*, 458:3134–3149.

Russell, H. R., Sanders, J. S., and Fabian, A. C. (2008). Direct X-ray spectral deprojection of galaxy clusters. *mnras*, 390:1207–1216.

Russell, P. A., Ponman, T. J., and Sanderson, A. J. R. (2007). Bayesian modelling of the cool core galaxy group NGC 4325. *mnras*, 378:1217–1228.

Salomé, P. and Combes, F. (2003). Cold molecular gas in cooling flow clusters of galaxies. *aap*, 412:657–667.

Salomé, P., Combes, F., Revaz, Y., Downes, D., Edge, A. C., and Fabian, A. C. (2011). A very extended molecular web around NGC 1275. *aap*, 531:A85.

Sanders, J. S. and Fabian, A. C. (2007). A deeper X-ray study of the core of the Perseus galaxy cluster: the power of sound waves and the distribution of metals and cosmic rays. *mnras*, 381:1381–1399.

Schawinski, K., Urry, C. M., Simmons, B. D., Fortson, L., Kaviraj, S., Keel, W. C., Lintott, C. J., Masters, K. L., Nichol, R. C., Sarzi, M., Skibba, R., Treister, E., Willett, K. W., Wong, O. I., and Yi, S. K. (2014). The green valley is a red herring: Galaxy Zoo reveals two evolutionary pathways towards quenching of star formation in early- and late-type galaxies. *mnras*, 440:889–907.

Schlegel, D. J., Finkbeiner, D. P., and Davis, M. (1998). Maps of Dust Infrared Emission for Use in Estimation of Reddening and Cosmic Microwave Background Radiation Foregrounds. *apj*, 500:525–553.

Schmidt, R. W. and Allen, S. W. (2007). The dark matter haloes of massive, relaxed galaxy clusters observed with Chandra. *mnras*, 379:209–221.

Schneider, P. (2015). *Extragalactic Astronomy and Cosmology: An Introduction*.

Schombert, J. M. (1986). The structure of brightest cluster members. I - Surface photometry. *apjs*, 60:603–693.

Sharma, P., McCourt, M., Quataert, E., and Parrish, I. J. (2012). Thermal instability and the feedback regulation of hot haloes in clusters, groups and galaxies. *mnras*, 420:3174–3194.

Shin, J., Woo, J.-H., and Mulchaey, J. S. (2016). A systematic search for X-ray cavities in galaxy clusters, groups, and elliptical galaxies. *ArXiv e-prints*.

Singh, A. and Sharma, P. (2015). The cold mode: a phenomenological model for the evolution of density perturbations in the intracluster medium. *mnras*, 446:1895–1906.

Smith, S. (1936). The Mass of the Virgo Cluster. *apj*, 83:23.

Soker, N. (2008). Entropy Limit and the Cold Feedback Mechanism in Cooling Flow Clusters. *apjl*, 684:L5.

Soker, N., White, III, R. E., David, L. P., and McNamara, B. R. (2001). A Moderate Cluster Cooling Flow Model. *apj*, 549:832–839.

Strateva, I., Ivezić, Ž., Knapp, G. R., Narayanan, V. K., Strauss, M. A., Gunn, J. E., Lupton, R. H., Schlegel, D., Bahcall, N. A., Brinkmann, J., Brunner, R. J., Budavári, T., Csabai, I., Castander, F. J., Doi, M., Fukugita, M., Győry, Z., Hamabe, M., Hennessy, G., Ichikawa, T., Kunszt, P. Z., Lamb, D. Q., McKay, T. A., Okamura, S., Racusin, J., Sekiguchi, M., Schneider, D. P., Shimasaku, K., and York, D. (2001). Color Separation of Galaxy Types in the Sloan Digital Sky Survey Imaging Data. *aj*, 122:1861–1874.

Sun, M. (2009). Every BCG with a Strong Radio Agn has an X-Ray Cool Core: Is the Cool Core-Noncool Core Dichotomy Too Simple? *apj*, 704:1586–1604.

Sun, M., Jones, C., Forman, W., Vikhlinin, A., Donahue, M., and Voit, M. (2007). X-Ray Thermal Coronae of Galaxies in Hot Clusters: Ubiquity of Embedded Mini-Cooling Cores. *apj*, 657:197–231.

Tan, J. C., Beuther, H., Walter, F., and Blackman, E. G. (2008). A Search for Molecular Gas in the Nucleus of M87 and Implications for the Fueling of Supermassive Black Holes. *apj*, 689:775–781.

Thomas, D., Maraston, C., Bender, R., and Mendes de Oliveira, C. (2005). The Epochs of Early-Type Galaxy Formation as a Function of Environment. *apj*, 621:673–694.

Tozzi, P. and Norman, C. (2001). The Evolution of X-Ray Clusters and the Entropy of the Intracluster Medium. *apj*, 546:63–84.

Tremblay, G. R., Oonk, J. B. R., Combes, F., Salomé, P., O'Dea, C. P., Baum, S. A., Voit, G. M., Donahue, M., McNamara, B. R., Davis, T. A., McDonald, M. A., Edge, A. C., Clarke, T. E., Galván-Madrid, R., Bremer, M. N., Edwards, L. O. V., Fabian, A. C., Hamer, S., Li, Y., Maury, A., Russell, H. R., Quillen, A. C., Urry, C. M., Sanders, J. S., and Wise, M. W. (2016). Cold, clumpy accretion onto an active supermassive black hole. *nat*, 534:218–221.

Vantyghem, A. N., McNamara, B. R., Russell, H. R., Hogan, M. T., Edge, A. C., Nulsen, P. E. J., Fabian, A. C., Combes, F., Salome, P., Baum, S. A., Donahue, M., Main, R. A., Murray, N. W., O'Connell, R. W., O'Dea, C. P., Oonk, J. B. R., Parrish, I. J., Sanders, J. S., Tremblay, G., and Voit, G. M. (2016). Molecular Gas Along a Bright H-alpha Filament in 2A 0335+096 Revealed by ALMA. *ArXiv e-prints*.

Vantyghem, A. N., McNamara, B. R., Russell, H. R., Main, R. A., Nulsen, P. E. J., Wise, M. W., Hoekstra, H., and Gitti, M. (2014). Cycling of the powerful AGN in MS 0735.6+7421 and the duty cycle of radio AGN in clusters. *mnras*, 442:3192–3205.

Vikhlinin, A., Kravtsov, A., Forman, W., Jones, C., Markevitch, M., Murray, S. S., and Van Speybroeck, L. (2006). Chandra Sample of Nearby Relaxed Galaxy Clusters: Mass, Gas Fraction, and Mass-Temperature Relation. *apj*, 640:691–709.

Voigt, L. M. and Fabian, A. C. (2004). Thermal conduction and reduced cooling flows in galaxy clusters. *mnras*, 347:1130–1149.

Voit, G. M. (2005). Expectations for evolution of cluster scaling relations. *Advances in Space Research*, 36:701–705.

Voit, G. M., Cavagnolo, K. W., Donahue, M., Rafferty, D. A., McNamara, B. R., and Nulsen, P. E. J. (2008). Conduction and the Star Formation Threshold in Brightest Cluster Galaxies. *apjl*, 681:L5.

Voit, G. M. and Donahue, M. (2015). Cooling Time, Freefall Time, and Precipitation in the Cores of ACCEPT Galaxy Clusters. *apjl*, 799:L1.

Voit, G. M., Donahue, M., Bryan, G. L., and McDonald, M. (2015). Regulation of star formation in giant galaxies by precipitation, feedback and conduction. *nat*, 519:203–206.

Voit, G. M., Meece, G., Li, Y., O'Shea, B. W., Bryan, G. L., and Donahue, M. (2016). A Global Model For Circumgalactic and Cluster-Core Precipitation. *ArXiv e-prints*.

von Hoerner, S. (1974). *Galactic and Extra-Galactic Radio Astronomy*. G. L. Verschuur and K. I. Kellermann (eds), New York.

Wilman, R. J., Edge, A. C., and Johnstone, R. M. (2005). The nature of the molecular gas system in the core of NGC 1275. *mnras*, 359:755–764.

Yamasaki, N. Y., Ohashi, T., and Furusho, T. (2002). Chandra Observation of the Central Galaxies in the A1060 Cluster of Galaxies. *apj*, 578:833–841.

York, D. G., Adelman, J., Anderson, Jr., J. E., Anderson, S. F., Annis, J., Bahcall, N. A., Bakken, J. A., Barkhouser, R., Bastian, S., Berman, E., Boroski, W. N., Bracker, S., Briegel, C., Briggs, J. W., Brinkmann, J., Brunner, R., Burles, S., Carey, L., Carr, M. A., Castander, F. J., Chen, B., Colestock, P. L., Connolly, A. J., Crocker, J. H., Csabai, I., Czarapata, P. C., Davis, J. E., Doi, M., Dombeck, T., Eisenstein, D., Ellman, N., Elms, B. R., Evans, M. L., Fan, X., Federwitz, G. R., Fiscelli, L., Friedman, S., Frieman, J. A., Fukugita, M., Gillespie, B., Gunn, J. E., Gurbani, V. K., de Haas, E., Haldeman, M., Harris, F. H., Hayes, J., Heckman, T. M., Hennessy, G. S., Hindsley, R. B., Holm, S., Holmgren, D. J., Huang, C.-h., Hull, C., Husby, D., Ichikawa, S.-I., Ichikawa, T., Ivezić, Ž., Kent, S., Kim, R. S. J., Kinney, E., Klaene, M., Kleinman, A. N., Kleinman, S., Knapp, G. R., Korienek, J., Kron, R. G., Kunszt, P. Z., Lamb, D. Q., Lee, B., Leger, R. F., Limmongkol, S., Lindenmeyer, C., Long, D. C., Loomis, C., Loveday, J., Lucinio, R., Lupton, R. H., MacKinnon, B., Mannery, E. J., Mantsch, P. M., Margon, B., McGehee, P., McKay, T. A., Meiksin, A., Merelli, A., Monet, D. G., Munn, J. A., Narayanan, V. K., Nash, T., Neilsen, E., Neswold, R., Newberg, H. J., Nichol, R. C., Nicinski, T., Nonino, M., Okada, N., Okamura, S., Ostriker, J. P., Owen, R., Pauls, A. G., Peoples, J., Peterson, R. L., Petravick, D., Pier, J. R., Pope, A., Pordes, R., Prosapio, A., Rechenmacher, R., Quinn, T. R., Richards, G. T., Richmond, M. W., Rivetta, C. H., Rockosi, C. M., Ruthmansdorfer, K., Sandford, D., Schlegel, D. J., Schneider, D. P., Sekiguchi, M., Sergey, G., Shimasaku, K., Siegmund, W. A., Smee, S., Smith, J. A., Snedden, S., Stone, R., Stoughton, C., Strauss, M. A., Stubbs, C., SubbaRao, M., Szalay, A. S., Szapudi, I., Szokoly, G. P., Thakar, A. R., Tremonti, C., Tucker, D. L., Uomoto, A., Vanden Berk, D., Vogeley, M. S., Waddell, P., Wang, S.-i., Watanabe, M., Weinberg, D. H., Yanny, B., Yasuda, N., and SDSS Collaboration (2000). The Sloan Digital Sky Survey: Technical Summary. *aj*, 120:1579–1587.

Young, J. S. and Scoville, N. Z. (1991). Molecular gas in galaxies. *araa*, 29:581–625.

Young, L. M., Bureau, M., Davis, T. A., Combes, F., McDermid, R. M., Alatalo, K., Blitz, L., Bois, M., Bournaud, F., Cappellari, M., Davies, R. L., de Zeeuw, P. T., Emsellem, E.,

Khochfar, S., Krajnović, D., Kuntschner, H., Lablanche, P.-Y., Morganti, R., Naab, T., Oosterloo, T., Sarzi, M., Scott, N., Serra, P., and Weijmans, A.-M. (2011). The ATLAS^{3D} project - IV. The molecular gas content of early-type galaxies. *mnras*, 414:940–967.

APPENDICES

Appendix A

Tables

Table A.1: Data Sample

		X-Ray Core (J2000.0)			BCG Core (J2000.0)	
System	z	α	δ	BCG Name	α	δ
A85	0.055	00:41:50.567	-9:18:10.86	MCG-02-02-086	00:41:50.524	-09:18:10.94
A262	0.017	01:52:46.299	+36:09:11.80	NGC708	01:52:46.482	+36:09:06.53
A478	0.088	04:13:25.345	+10:27:55.15	2MASXJ04132526+1027551	04:13:25.266	+10:27:55.14
A496	0.033	04:33:38.038	-13:15:39.65	MCG-02-12-039	04:33:37.841	-13:15:43.04
A1060	0.013	10:36:42.830	-27:31:39.62	NGC3311	10:36:42.821	-27:31:42.02
A1068	0.138	10:40:44.520	+39:57:10.28	2MASXJ10404446+3957117	10:40:44.504	+39:57:11.26
A1664	0.128	13:03:42.622	-24:14:41.59	2MASXJ13034252-2414428	13:03:42.521	-24:14:42.81
A1835	0.253	14:01:01.951	+02:52:43.18	2MASXJ14010204+0252423	14:01:02.043	+02:52:42.34
A1991	0.059	14:54:31.553	+18:38:39.79	NGC5778	14:54:31.465	+18:38:32.57
A2052	0.035	15:16:44.443	+7:01:17.32	UGC9799	15:16:44.487	+07:01:18.00
A2204	0.152	16:32:46.920	+05:34:32.86	VLSSJ1632.7+0534	16:32:46.94	+05:34:32.6
A2597	0.085	23:25:19.779	-12:07:27.63	PKS2322-12	23:25:19.731	-12:07:27.51
A3581	0.023	14:07:29.791	-27:01:04.06	IC4374	14:07:29.780	-27:01:04.39
A3880	0.058	22:27:54.455	-30:34:32.88	PKS2225-308	22:27:54.463	-30:34:32.12
Cygnus-A	0.056	19:59:28.259	+40:44:02.10	CygnusA	19:59:28.357	+40:44:02.10
H1821+643	0.297	18:21:57.191	+64:20:36.56	H1821+643	18:21:57.237	+64:20:36.23
Hydra-A	0.055	9:18:05.673	-12:05:43.65	Hydra-A	09:18:05.651	-12:05:43.99
MACS1532.9+3021	0.345	15:32:53.820	+30:20:59.75	SDSSJ153253.78+302059.3	15:32:53.778	+30:20:59.42
NGC4325	0.026	12:23:06.659	+10:37:15.53	NGC4325	12:23:06.672	+10:37:17.05
NGC5044	0.009	13:15:23.904	-16:23:07.53	NGC5044	13:15:23.969	-16:23:08.00
PKS0745-191	0.103	7:47:31.228	-19:17:41.01	PKS0745-191	07:47:31.296	-19:17:40.34
RXCJ0338.6+0958	0.036	3:38:41.055	+9:58:02.26	2MASXJ03384056+0958119	3:38:40.579	+9:58:11.78
RXCJ0352.9+1941	0.109	3:52:59.001	+19:40:59.81	2MASXJ03525901+1940595	3:52:59.016	+19:40:59.59
RXJ0821.0+0752	0.110	8:21:02.018	+7:51:47.58	2MASXJ08210226+0751479	08:21:02.265	+07:51:47.95
RXJ1504.1-0248	0.215	15:04:07.529	-2:48:16.75	2MASXJ15040752-0248161	15:04:07.519	-02:48:16.65
RXCJ1524.2-3154	0.103	15:24:12.861	-31:54:23.52	2MASXJ15241295-3154224	15:24:12.957	-31:54:22.45
RXCJ1558.3-1410	0.097	15:58:21.948	-14:09:58.43	PKS1555-140	15:58:21.948	-14:09:59.05
RXJ1350.3+0940	0.090	13:50:21.891	+9:40:10.84	2MASXJ13502209+0940109	13:50:22.136	+09:40:10.66
RXCJ1459.4-1811	0.236	14:59:28.713	-18:10:45.01	2MASXJ14592875-1810453	14:59:28.763	-18:10:45.19
ZwCl1883	0.194	8:42:55.952	+29:27:25.61	2MASXJ08425596+2927272	08:42:55.972	+29:27:26.91
ZwCl3146	0.291	10:23:39.741	+4:11:10.64	2MASXJ10233960+0411116	10:23:39.609	+04:11:11.68

ZwCl7160	0.258	14:57:15.073	+22:20:35.18	2MASXJ14571507+2220341	14:57:15.077	+22:20:34.16
ZwCl8276	0.076	17:44:14.448	+32:59:29.38	2MASXJ17441450+3259292	17:44:14.5	+32:59:29
4C+55.16	0.242	8:34:54.917	+55:34:21.44	2MFGC06756	08:34:54.903	+55:34:21.09
A1668	0.063	13:03:46.602	13:03:46.602	IC4130	13:03:46.586	+19:16:17.06
A2029	0.077	15:10:56.104	+5:44:41.14	IC1101	15:10:56.104	+05:44:41.69
A2142	0.091	15:58:20.880	+27:13:44.21	2MASXJ15582002+2714000	15:58:20.028	+27:14:00.06
A2151	0.037	16:04:35.758	+17:43:18.54	NGC6041	16:04:35.757	+17:43:17.20
A2199	0.030	16:28:38.249	+39:33:04.28	NGC6166	16:28:38.276	+39:33:04.97
A2261	0.224	17:22:27.140	+32:07:57.43	2MASXJ17222717+3207571	17:22:27.173	+32:07:57.18
A2319	0.056	19:21:09.638	+43:57:21.53	MCG+07-40-004	19:21:10.049	+43:56:44.32
A2390	0.228	21:53:36.768	+17:41:42.17	2MASXJ21533687+1741439	21:53:36.827	+17:41:43.73
A2462	0.073	22:39:11.367	-17:20:28.33	2MASXJ22391136-1720284	22:39:11.367	-17:20:28.49
A2634	0.031	23:38:29.426	+27:01:53.86	NGC7720	23:38:29.390	+27:01:53.53
A2657	0.040	23:44:57.253	+09:11:30.74	2MASXJ23445742+0911349	23:44:57.422	+09:11:34.96
A2626	0.055	23:36:30.375	+21:08:48.21	IC5338	23:36:30.482	+21:08:47.46
A2665	0.056	23:50:50.557	+6:09:03.00	MCG+01-60-039	23:50:50.537	+06:08:58.35
A2734	0.063	0:11:21.665	-28:51:15.05	ESO409-25	00:11:21.667	-28:51:15.85
A3526	0.011	12:48:48.949	-41:18:43.92	NGC4696	12:48:49.277	-41:18:39.92
AWM7	0.017	12:30:49.361	+12:23:28.10	NGC1129	02:54:27.400	+41:34:46.70
M87	0.004	12:30:49.368	+12:23:28.50	M87	12:30:49.423	+12:23:28.04
RXJ0439.0+0520	0.208	4:39:02.180	+5:20:43.33	2MASXJ04390223+0520443	04:39:02.263	+05:20:43.70
RXJ1347.5-1145	0.451	13:47:30.641	-11:45:08.51	GALEXJ134730.7-114509	13:47:31.00	-11:45:09.0
ZwCl235	0.083	0:43:52.184	+24:24:20.09	2MASXJ00435213+2424213	00:43:52.140	+24:24:21.31
ZwCl2089	0.230	9:00:36.887	+20:53:40.79	2MASXJ09003684+2053402	09:00:36.848	+20:53:40.24

Table A.2: Molecular Gas Mass Compilation

System		$S_{CO(1-0)}\Delta\nu$ [a] (Jy km s^{-1})	$M_{\rm mol}$ [b] ($M_\odot$)	Reference
A85	CO(2-1)	0.74903 ± 0.35	$4.5 \pm 2.5 \times 10^8$	Edge (priv. comm,2016)
A262	CO(1-0)	6.81 ± 0.98	$4.0 \pm 1.3 \times 10^8$	Edge (2001)
	CO(1-0)	3.90 ± 0.51	$2.3 \pm 0.3 \times 10^8$	Salomé and Combes (2003)
A478	CO(1-0)	1.20 ± 0.69	$1.9 \pm 1.2 \times 10^9$	Edge (2001)
A496	CO(1-0)	1.07 ± 0.28	$2.8 \pm 0.9 \times 10^8$	Edge (priv. comm,2016)
	CO(1-0)	2.03 ± 0.47	$4.3 \pm 1.0 \times 10^8$	Salomé and Combes (2003)
	CO(2-1)	0.35 ± 0.18	$7.5 \pm 4.4 \times 10^7$	Edge (priv. comm,2016)
A1060	CO(1-0)	3.76 ± 0.51	$1.2 \pm 0.4 \times 10^8$	Edge (priv. comm,2016)
	CO(2-1)	1.85 ± 0.27	$5.7 \pm 1.9 \times 10^7$	Edge (priv. comm,2016)
A1068	CO(1-0)	8.74 ± 0.62	$3.4 \pm 1.0 \times 10^{10}$	Edge (2001)
	CO(1-0)	10.82 ± 0.52	$4.2 \pm 0.2 \times 10^{10}$	Salomé and Combes (2003)
A1664	CO(1-0)	5.25 ± 0.84	$1.8 \pm 0.6 \times 10^{10}$	Edge (2001)
	CO(1-0)	8.19 ± 1.08	$2.8 \pm 0.9 \times 10^{10}$	Edge (priv. comm,2016)
A1835	CO(1-0)	4.76 ± 0.53	$6.5 \pm 2.1 \times 10^{10}$	Edge (2001)
A1991	CO(2-1)	0.90 ± 0.28	$6.2 \pm 2.7 \times 10^8$	Edge (priv. comm,2016)
A2052	CO(1-0)	3.66 ± 0.96	$9.0 \pm 3.6 \times 10^8$	Edge (priv. comm,2016)
	CO(2-1)	1.39 ± 0.37	$3.4 \pm 1.4 \times 10^8$	Edge (priv. comm,2016)
A2204	CO(1-0)	1.90 ± 0.49	$9.1 \pm 3.6 \times 10^9$	Edge (2001)
	CO(1-0)	2.19 ± 0.59	$1.0 \pm 0.4 \times 10^{10}$	Edge (priv. comm,2016)
A2597	CO(1-0)	2.32 ± 0.95	$3.4 \pm 1.7 \times 10^9$	Edge (2001)
	CO(1-0)	1.76 ± 0.71	$2.6 \pm 1.3 \times 10^9$	Edge (priv. comm,2016)
	CO(2-1)	0.96 ± 0.14	$1.4 \pm 0.5 \times 10^9$	Edge (priv. comm,2016)
A3581	CO(1-0)	3.17 ± 1.08	$3.3 \pm 1.5 \times 10^8$	Edge (priv. comm,2016)
	CO(2-1)	0.80 ± 0.19	$8.2 \pm 3.1 \times 10^7$	Edge (priv. comm,2016)
A3880	CO(1-0)	3.56 ± 0.95	$2.4 \pm 1.0 \times 10^9$	Edge (priv. comm,2016)
Cygnus-A	CO(2-1)	1.71 ± 0.31	$1.0 \pm 0.4 \times 10^9$	Edge (priv. comm,2016)
H1821+643	CO(1-0)	0.75 ± 0.25	$1.4 \pm 0.6 \times 10^{10}$	Edge (priv. comm,2016)
Hydra-A	CO(1-0)	6.58 ± 1.78	$3.9 \pm 1.6 \times 10^9$	Edge (priv. comm,2016)
	CO(1-0)	3.48 ± 0.52	$2.0 \pm 0.3 \times 10^9$	Salomé and Combes (2003)
MACS1532.9+3021	CO(1-0)	3.24 ± 0.52	$8.4 \pm 2.9 \times 10^{10}$	Edge (2001)
	CO(1-0)	3.60 ± 0.54	$9.4 \pm 3.1 \times 10^{10}$	Edge (priv. comm,2016)
NGC4325	CO(1-0)	1.92 ± 0.45	$2.5 \pm 0.9 \times 10^8$	Edge (priv. comm,2016)
NGC5044	CO(1-0)	14.08 ± 2.62	$2.3 \pm 0.8 \times 10^8$	Edge (priv. comm,2016)
	CO(2-1)	3.65 ± 0.50	$6.1 \pm 2.0 \times 10^7$	Edge (priv. comm,2016)
PKS0745-191	CO(1-0)	1.87 ± 0.42	$4.0 \pm 0.9 \times 10^9$	Salomé and Combes (2003)
RXCJ0338.6+0958	CO(1-0)	6.59 ± 0.68	$1.7 \pm 0.5 \times 10^9$	Edge (2001)
RXCJ0352.9+1941	CO(1-0)	2.04 ± 0.51	$4.9 \pm 1.9 \times 10^9$	Edge (2001)
RXJ0821.0+0752	CO(1-0)	6.49 ± 0.67	$1.6 \pm 0.5 \times 10^{10}$	Edge (2001)
	CO(1-0)	5.29 ± 0.81	$1.3 \pm 0.2 \times 10^{10}$	Salomé and Combes (2003)
RXJ1504.1-0248	CO(1-0)	3.84 ± 0.62	$3.8 \pm 1.3 \times 10^{10}$	Edge (priv. comm,2016)
RXCJ1524.2-3154	CO(1-0)	1.36 ± 0.54	$2.9 \pm 1.6 \times 10^9$	Edge (priv. comm,2016)
	CO(2-1)	2.16 ± 0.46	$4.6 \pm 1.7 \times 10^9$	Edge (priv. comm,2016)
RXCJ1558.3-1410	CO(1-0)	2.79 ± 0.55	$5.3 \pm 1.9 \times 10^9$	Edge (priv. comm,2016)
RXJ1350.3+0940	CO(1-0)	6.14 ± 1.32	$1.0 \pm 0.4 \times 10^{10}$	Edge (priv. comm,2016)
	CO(2-1)	3.86 ± 1.15	$6.3 \pm 2.7 \times 10^9$	Edge (priv. comm,2016)
RXCJ1459.4-1811	CO(1-0)	1.91 ± 0.77	$2.2 \pm 1.1 \times 10^{10}$	Edge (priv. comm,2016)
ZwCl1883	CO(1-0)	0.76 ± 0.52	$6.2 \pm 4.5 \times 10^9$	Edge (priv. comm,2016)
ZwCl3146	CO(1-0)	3.09 ± 0.58	$5.6 \pm 2.0 \times 10^{10}$	Edge (2001)
ZwCl7160	CO(1-0)	1.55 ± 0.61	$2.2 \pm 1.1 \times 10^{10}$	Edge (2001)
	CO(1-0)	4.08 ± 1.23	$5.8 \pm 2.5 \times 10^{10}$	Edge (priv. comm,2016)
ZwCl8276	CO(1-0)	3.02 ± 0.44	$3.5 \pm 1.2 \times 10^9$	Edge (2001)
	CO(1-0)	3.31 ± 0.50	$3.8 \pm 1.3 \times 10^9$	Edge (priv. comm,2016)

4C+55.16	CO(1-0)	1.32	$< 1.6 \times 10^{10}$	Edge (2001)
A1668	CO(1-0)	1.88	$< 1.5 \times 10^{9}$	Salomé and Combes (2003)
A2029	CO(1-0)	1.42	$< 1.7 \times 10^{9}$	Salomé and Combes (2003)
A2142	CO(1-0)	1.08	$< 1.8 \times 10^{9}$	Salomé and Combes (2003)
A2151	CO(1-0)	1.18	$< 3.1 \times 10^{8}$	Salomé and Combes (2003)
A2199	CO(1-0)	1.46	$< 2.6 \times 10^{8}$	Salomé and Combes (2003)
A2261	CO(1-0)	1.22	$< 1.3 \times 10^{10}$	Salomé and Combes (2003)
A2319	CO(1-0)	1.07	$< 6.6 \times 10^{8}$	Salomé and Combes (2003)
A2390	CO(1-0)	1.64	$< 1.8 \times 10^{10}$	Edge (2001)
A2462	CO(1-0)	1.49	$< 1.6 \times 10^{9}$	Salomé and Combes (2003)
A2634	CO(1-0)	1.66	$< 3.2 \times 10^{8}$	Salomé and Combes (2003)
A2657	CO(1-0)	0.91	$< 2.9 \times 10^{8}$	Salomé and Combes (2003)
A2626	CO(1-0)	1.25	$< 7.6 \times 10^{8}$	Salomé and Combes (2003)
A2665	CO(1-0)	1.29	$< 7.9 \times 10^{8}$	Salomé and Combes (2003)
A2734	CO(1-0)	0.83	$< 6.5 \times 10^{8}$	Edge (priv. comm,2016)
A3526	CO(1-0)	8.91	$< 2.2 \times 10^{8}$	Edge (2001) from O'Dea et al. (1994)
AWM7	CO(1-0)	2.70	$< 1.6 \times 10^{8}$	Edge (2001) from Fujita et al. (2000)
M87	CO(1-0)	16.60	$< 5.9 \times 10^{7}$	Edge (2001) from Jaffe (1987)
RXJ0439.0+0520	CO(1-0)	1.36	$< 1.2 \times 10^{10}$	Edge (2001)
	CO(1-0)	1.08	$< 9.8 \times 10^{9}$	Salomé and Combes (2003)
RXJ1347.5-1145	CO(3-2)	0.47	$< 2.1 \times 10^{10}$	Edge (2001)
ZwCl235	CO(1-0)	1.81	$< 2.5 \times 10^{9}$	Salomé and Combes (2003)
ZwCl2089	CO(1-0)	1.51	$< 1.7 \times 10^{10}$	Edge (2001)

Notes: Summary of compiled molecular gas masses. The gas mass of A85,A1991,and Cygnus-A were derived from CO(2-1) measurements assuming a flux ratio of CO(2-1)/CO(1-0) of 3.2 (David et al., 2014). The upper limit for RXJ1347.5-1145 was derived from a CO(3-2) measurement using a flux ratio of CO(3-2)/CO(1-0) of 7.0 (Russell et al., 2016b). The integrated flux densities in CO(1-0) computed from these ratios are shown in the table with the symbol *.
[a] integrated flux density.
[b] molecular gas mass

Table A.3: X-ray Observation Properties

System	n_H (10^{22}cm^{-2})[a]	ObsID	Total Exposure (ks) Raw	Clean
A85	0.0278	15173,15174,16263,16264,904	195.2	193.6
A262	0.1250*	2215,7921	139.4	137.4
A478	0.3000*	1669,6102	52.4	46.8
A496	0.0378	4976,931	94.0	61.7
A1060	0.0800*	2220	31.9	29.4
A1068	0.0169	1652	26.8	23.2
A1664	0.0886	1648,17172,17173,17557,17568,7901	245.5	233.3
A1835	0.0204	6880,6881,7370	193.7	139.1
A1991	0.0246	3193	38.3	34.5
A2052	0.0270	10477,10478,10479,10480,10879,10914,10915,10916,10917,5807,890	654.0	640.4
A2204	0.0567	6104,7940	86.8	80.1
A2597	0.0248	6934,7329,922	151.6	137.6
A3581	0.0436	12884,1650	91.7	90.6
A3880	0.0117	5798	22.3	18.6
Cygnus-A	0.2720	5830,5831,6225,6226,6228,6229,6250,6252	198.1	193.6
H1821+643	0.0344	9398,9845,9846,9848	87.0	83.2
Hydra-A	0.0468	4969,4970,576	215.3	186.4
MACS1532.9+3021	0.0230	14009,1649,1665	108.2	102.4
NGC4325	0.0232	3232	30.1	25.7
NGC5044	0.0487	9399	82.7	82.5
PKS0745-191	0.4180	12881,1509,2427,510	220.6	210.1
RXCJ0338.6+0958	0.2218*	7939,9792	83.3	81.2
RXCJ0352.9+1941	0.1220	10466	27.2	27.2
RXJ0821.0+0752	0.0195	17194,17563	66.6	63.5
RXJ1504.1-0248	0.0597	17197,17669,17670,4935,5793	161.7	135.3
RXCJ1524.2-3154	0.0853	9401	40.9	40.9
RXCJ1558.3-1410	0.1060	9402	40.1	35.8
RXJ1350.3+0940	0.0241	14021	19.8	19.4
RXCJ1459.4-1811	0.0737	9428	39.6	39.5
ZwCl1883	0.0411	2224	29.8	26.3
ZwCl3146	0.0246	1651,9371	206.0	189.6
ZwCl7160	0.0318	4192,543	101.7	80.0
ZwCl8276	0.0383	11708,8267	53.5	53.2
4C+55.16	0.0429	4940	96.0	65.5
A1668	0.0220	12877	10.0	10.0
A2029	0.0327	4977,6101,891	107.6	103.3
A2142	0.0379	15186,16564,16565,5005	199.7	184.6
A2151	0.0334	4996	21.8	14.4
A2199	0.0089	10748,10803,10804,10805,497,498	158.2	155.8
A2261	0.0319	5007	24.3	22.1
A2319	0.0810	15187,3231	89.6	86.8
A2390	0.0621	4193,500,501	113.9	88.2
A2462	0.0299	4159	39.2	37.6
A2626	0.0383	16136,3192	135.6	132.5
A2634	0.0481	4816	49.5	47.5
A2657	0.0950	4941	16.1	15.9
A2665	0.0581	12280	9.9	9.4
A2734	0.0139	5797	19.9	18.9
A3526	0.0856	16223,16224,16225,16534,16607,16608,16609,16610	486.3	478.5
AWM7	0.0869	11717,12016,12017,12018	133.8	133.5
M87	0.0194	5826,5827	283.0	283.0
RXJ0439.0+0520	0.0892	9369,9761	28.5	25.9
RXJ1347.5-1145	0.0460	13516,13999,14407,2222,3592,506,507	326.5	286.4
ZwCl2089	0.0287	10463,7897	49.7	46.9
ZwCl235	0.0371	11735	19.8	19.4

[a] The hydrogen column density was frozen to these values (taken from Kalberla et al. (2005)) when fitting in XSPEC with the MEKAL model unless the best fit value was found to be significantly different (these are marked with the asterisk (*) symbol).

Table A.4: Mass Parameters

System	σ_* (km s^{-1})	r_s (kpc)	ρ_0 (keV)	M_{2500} (10^{13} M$_\odot$)
A85	270 ± 6	$376.2^{+37.0}_{-25.4}$	$49.1^{+4.0}_{-2.7}$	$22.2^{+1.1}_{-1.2}$
A262	189 ± 3	$185.8^{+3.7}_{-0.4}$	$12.9^{+0.3}_{-0.0}$	$3.4^{+0.1}_{-0.1}$
A478	271 ± 7	$588.2^{+206.8}_{-130.7}$	$71.4^{+18.2}_{-12.4}$	$33.3^{+5.4}_{-6.0}$
A496	228 ± 5	$190.1^{+68.1}_{-38.3}$	$32.8^{+2.5}_{-1.5}$	$12.9^{+1.1}_{-1.1}$
A1060	208 ± 12	$191.7^{+0.0}_{0.0}$	$36.9^{+0.0}_{0.0}$	$15.0^{+0.0}_{0.0}$
A1068	311 ± 12	$519.4^{+122.2}_{-79.8}$	$47.3^{+8.4}_{-5.0}$	$18.5^{+1.8}_{-1.7}$
A1664	267 ± 12	$300.2^{+31.4}_{-29.5}$	$25.7^{+2.3}_{-1.1}$	$8.8^{+0.5}_{-0.5}$
A1835	486 ± 24	$550.3^{+45.3}_{-61.8}$	$94.3^{+5.7}_{-7.7}$	$55.8^{+3.3}_{-3.2}$
A1991	222 ± 8	$266.4^{+93.5}_{-98.9}$	$25.1^{+5.0}_{-6.7}$	$8.5^{+1.5}_{-1.4}$
A2052	221 ± 5	$170.6^{+55.9}_{-39.6}$	$24.8^{+4.1}_{-3.3}$	$8.7^{+1.4}_{-1.4}$
A2204	343 ± 13	$409.6^{+40.6}_{-36.0}$	$80.9^{+5.0}_{-4.3}$	$45.7^{+2.2}_{-2.4}$
A2597	218 ± 10	$257.4^{+52.5}_{-16.9}$	$37.9^{+5.5}_{-2.0}$	$15.1^{+1.6}_{-1.6}$
A3581	195 ± 3	$80.7^{+14.5}_{-13.6}$	$8.4^{+0.5}_{-0.5}$	$2.0^{+0.1}_{-0.1}$
A3880	236 ± 7	$122.1^{+95.3}_{-47.4}$	$21.7^{+4.9}_{-2.8}$	$7.2^{+1.6}_{-1.6}$
Cygnus-A	268 ± 8	$145.0^{+69.9}_{-43.1}$	$45.2^{+4.5}_{-2.1}$	$19.6^{+0.1}_{-0.1}$
H1821+643	250 ± 15	$171.5^{+216.7}_{-15.9}$	$23.1^{+13.6}_{-3.7}$	$7.2^{+2.8}_{-2.7}$
Hydra-A	237 ± 8	$551.8^{+22.7}_{-36.7}$	$37.8^{+0.9}_{-1.4}$	$12.2^{+0.2}_{-0.2}$
MACS1532.9+3021	250 ± 15	$769.0^{+535.9}_{-144.0}$	$105.2^{+50.0}_{-14.8}$	$43.7^{+7.3}_{-7.5}$
NGC4325	174 ± 5	$66.2^{+12.4}_{-7.6}$	$4.9^{+0.5}_{-0.3}$	$1.0^{+0.1}_{-0.1}$
NGC5044	196 ± 11	$45.1^{+5.4}_{-4.7}$	$7.0^{+0.2}_{-0.2}$	$1.5^{+0.1}_{-0.1}$
PKS0745-191	290 ± 14	$437.9^{+186.1}_{-115.8}$	$67.4^{+18.7}_{-12.5}$	$33.9^{+5.8}_{-5.5}$
RXCJ0338.6+0958	220 ± 5	$153.2^{+62.5}_{-59.2}$	$21.3^{+4.6}_{-3.8}$	$7.1^{+1.6}_{-1.5}$
RXCJ0352.9+1941	239 ± 10	$223.3^{+37.6}_{-15.0}$	$22.6^{+2.0}_{-0.9}$	$7.5^{+0.4}_{-0.4}$
RXJ0821.0+0752	247 ± 9	$268.8^{+453.5}_{-159.1}$	$20.7^{+22.2}_{-7.9}$	$6.5^{+2.8}_{-2.6}$
RXJ1504.1-0248	386 ± 22	$787.8^{+142.3}_{-107.2}$	$111.4^{+15.3}_{-12.0}$	$58.6^{+4.6}_{-4.5}$
RXCJ1524.2-3154	265 ± 12	$450.5^{+104.3}_{-53.7}$	$64.5^{+11.1}_{-5.3}$	$30.9^{+3.0}_{-2.7}$
RXCJ1558.3-1410	280 ± 14	$451.5^{+86.3}_{-89.4}$	$47.5^{+6.3}_{-6.4}$	$19.6^{+1.8}_{-1.8}$
RXJ1350.3+0940	188 ± 13	$111.4^{+22.1}_{-59.2}$	$29.3^{+2.2}_{-9.3}$	$9.7^{+1.7}_{-1.8}$
RXCJ1459.4-1811	439 ± 22	$421.1^{+128.7}_{-82.1}$	$46.1^{+8.3}_{-6.0}$	$21.6^{+2.1}_{-2.3}$
ZwCl1883	335 ± 12	$315.6^{+196.8}_{-82.1}$	$27.7^{+9.6}_{-4.8}$	$10.3^{+1.4}_{-1.5}$
ZwCl3146	372 ± 33	$719.6^{+104.5}_{-121.6}$	$87.1^{+10.0}_{-11.0}$	$38.2^{+2.9}_{-2.7}$
ZwCl7160	428 ± 21	$455.3^{+102.0}_{-64.2}$	$67.3^{+10.4}_{-7.4}$	$34.4^{+3.3}_{-3.3}$
ZwCl8276	219 ± 7	$531.6^{+59.4}_{-58.5}$	$54.3^{+4.8}_{-4.6}$	$21.5^{+1.2}_{-1.3}$
4C+55.16	274 ± 24	$452.5^{+35.4}_{-27.3}$	$49.4^{+1.8}_{-1.8}$	$18.6^{+1.2}_{-1.1}$
A1668	226 ± 7	$93.7^{+149.9}_{-14.4}$	$13.7^{+15.1}_{-1.2}$	$3.9^{+0.8}_{-0.7}$
A2029	336 ± 10	$511.4^{+50.4}_{-30.9}$	$79.8^{+5.1}_{-3.1}$	$44.8^{+1.8}_{-1.9}$
A2142	241 ± 11	$345.5^{+37.4}_{-21.3}$	$46.8^{+3.0}_{-1.5}$	$20.0^{+0.9}_{-0.8}$
A2151	219 ± 4	$196.0^{+38.7}_{-55.3}$	$15.4^{+1.4}_{-2.3}$	$4.6^{+0.4}_{-0.4}$
A2199	246 ± 4	$364.3^{+181.3}_{-119.4}$	$48.3^{+16.7}_{-11.0}$	$21.6^{+5.3}_{-5.6}$

A2261	460 ± 17	$396.6^{+114.4}_{-98.9}$	$77.0^{+13.1}_{-7.4}$	$45.1^{+5.2}_{-4.8}$
A2319	249 ± 7	$397.8^{+110.7}_{-316.9}$	$54.6^{+11.9}_{-41.6}$	$25.2^{+5.0}_{-4.6}$
A2390	348 ± 22	$799.1^{+183.0}_{-79.7}$	$101.3^{+17.8}_{-7.4}$	$47.6^{+3.9}_{-4.0}$
A2462	260 ± 8	$458.7^{+368.9}_{-207.7}$	$28.7^{+14.7}_{-8.5}$	$8.8^{+1.8}_{-1.8}$
A2634	269 ± 3	$133.9^{+63.2}_{-62.7}$	$38.4^{+10.3}_{-13.7}$	$15.9^{+5.5}_{-5.9}$
A2626	243 ± 7	$248.9^{+25.5}_{-25.6}$	$22.1^{+1.3}_{-1.3}$	$7.4^{+0.3}_{-0.3}$
A2657	172 ± 6	$103.8^{+98.6}_{-64.1}$	$8.8^{+2.0}_{-2.8}$	$2.1^{+0.6}_{-0.6}$
A2665	248 ± 7	$613.7^{+464.7}_{-203.9}$	$35.1^{+19.3}_{-8.7}$	$10.0^{+0.0}_{-0.0}$
A2734	231 ± 8	$379.3^{+827.8}_{-110.3}$	$21.1^{+27.0}_{-4.0}$	$5.8^{+1.2}_{-1.2}$
RXJ0439.0+0520	389 ± 21	$706.1^{+387.0}_{-237.1}$	$57.7^{+25.8}_{-16.0}$	$22.1^{+4.6}_{-4.3}$
RXJ1347.5-1145	250 ± 15	$308.9^{+40.9}_{-31.6}$	$153.5^{+11.7}_{-10.5}$	$94.7^{+7.1}_{-7.1}$
ZwCl235	240 ± 8	$206.1^{+63.8}_{-39.3}$	$21.4^{+2.3}_{-1.8}$	$7.2^{+0.6}_{-0.5}$
ZwCl2089	296 ± 18	$245.4^{+25.6}_{-28.3}$	$31.6^{+1.4}_{-2.0}$	$11.9^{+0.5}_{-0.6}$

σ_* denote the equivalent velocity dispersion of the central galaxy inferred from 2MASS isophotal magnitude if the galaxy consisted only of its stars.
r_s and ρ_0 denote the characteristic scale radius and density of the NFW profile obtained from the ISONFWMASS model (See Section 2.4.3).
M_{2500} denote the total cluster mass

Table A.5: Cavity Power and Star Formation Rate

System	Cavity Power			Star Formation			Ref.
	L_{radio} (10^{37} erg s^{-1})	P_{mech} (10^{42} erg s^{-1})	P_{cav} (10^{42} erg s^{-1})	$L_{H\alpha}$ (10^{40} erg s^{-1})	$\mathrm{SFR_{H\alpha}}$ ($\mathrm{M_\odot yr^{-1}}$)	$\mathrm{SFR_{IR}}$ ($\mathrm{M_\odot yr^{-1}}$)	
A85	2547.0 ± 109.6	35.9 ± 1.7	$37.0^{+37.0}_{-11.0}$	0.43	0.033 ± 0.010	1.57	[1],[2]
A262	277.3 ± 10.0	12.4 ± 2.3	$9.7^{+7.5}_{-2.6}$	0.43	0.033 ± 0.010	0.55	[1],[3]
A478	4419.3 ± 176.3	46.7 ± 0.5	$100.0^{+80.0}_{-20.0}$	7.86	1.453 ± 0.186	-	[1],[3]
A496	1836.9 ± 65.2	30.7 ± 2.1	0.261	0.72	0.065 ± 0.017	-	[14],[2]
A1060	1.7 ± 1.1	1.1 ± 0.5	172.0	-	-	-	[14],-
A1068	6813.7 ± 213.9	57.5 ± 1.1	20.0	121.43	51.039 ± 2.878	187.45	[1],[3]
A1664	9677.6 ± 315.6	68.1 ± 3.0	$95.2^{+74.0}_{-74.0}$	78.57	28.982 ± 1.862	14.54	[4],[3]
A1835	37100.5 ± 0.0	129.8 ± 19.2	$1800.0^{+1900.0}_{-600.0}$	100.00	39.654 ± 2.370	-	[1],[3]
A1991	1973.3 ± 65.1	31.7 ± 2.1	86.4	0.60	0.051 ± 0.014	1.66	[11],[2]
A2052	97379.6 ± 3703.8	206.3 ± 47.0	$150.0^{+200.0}_{-70.0}$	1.38	0.151 ± 0.033	1.37	[1],[2]
A2204	26717.6 ± 991.0	110.9 ± 13.5	$775.0^{+395.0}_{-385.0}$	114.29	47.171 ± 2.709	14.62	[5],[3]
A2597	205280.0 ± 6164.2	295.1 ± 86.7	$67.0^{+87.0}_{-29.0}$	37.14	10.943 ± 0.880	-	[1],[3]
A3581	4716.4 ± 166.4	48.2 ± 0.3	3.1	21.30	5.311 ± 0.505	-	[9],[2]
A3880	11302.9 ± 341.9	73.4 ± 4.1	$29.0^{+36.2}_{-23.8}$	-	-	-	[5],-
Cygnus-A	72764000.0 ± 1866910.0	4939.9 ± 4699.6	$1300.0^{+1100.0}_{-200.0}$	21.30	5.311 ± 0.505	-	[1],[2]
H1821+643	$<5988.1 \pm 0.0$	$<54.1 \pm 0.6$	No Cavity	-	-	-	[12],-
Hydra-A	1711150.0 ± 54522.0	816.5 ± 408.9	$430.0^{+200.0}_{-50.0}$	11.43	2.364 ± 0.271	-	[1],[3]
MACS1532.9+3021	56424.0 ± 1937.3	158.7 ± 28.9	$2220.0^{+860.0}_{-860.0}$	300.01	165.407 ± 7.110	96.15	[10],[3]
NGC4325	$<32.1 \pm 0.0$	$<4.4 \pm 1.3$	-	0.36	0.026 ± 0.008	0.66	-,[7]
NGC5044	42.0 ± 1.7	5.0 ± 1.4	$4.2^{+1.2}_{-2.0}$	-	-	-	[8],-
PKS0745-191	387291.0 ± 13662.8	400.2 ± 141.1	$1700.0^{+1400.0}_{-300.0}$	140.00	61.411 ± 3.318	17.07	[1],[6]
RXCJ0338.6+0958	706.2 ± 35.3	19.4 ± 2.5	$24.0^{+23.0}_{-6.0}$	7.14	1.283 ± 0.169	2.09	[1],[3]
RXCJ0352.9+1941	$<647.6 \pm 0.0$	$<18.6 \pm 2.5$	No Cavity	41.43	12.612 ± 0.982	11.04	[12],[3]
RXJ0821.0+0752	728.4 ± 0.0	19.7 ± 2.5	-	30.00	8.290 ± 0.711	36.91	-,[6]
RXJ1504.1-0248	50770.9 ± 2139.5	150.9 ± 26.1	-	-	-	-	-,-
RXCJ1524.2-3154	8178.1 ± 261.2	62.8 ± 2.0	$239.0^{+122.0}_{-122.0}$	-	-	-	[5],-
RXCJ1558.3-1410	66509.2 ± 2350.6	171.8 ± 33.6	$44.5^{+26.7}_{-26.7}$	-	-	-	[5],-
RXJ1350.3+0940	36019.6 ± 1082.2	128.0 ± 18.6	-	-	-	-	-,-
RXCJ1459.4-1811	106668.0 ± 3229.3	215.5 ± 50.8	No Cavity	-	-	-	[12],-
ZwCl1883	16425.2 ± 586.6	87.8 ± 7.4	-	-	-	-	-,-
ZwCl3146	12041.0 ± 813.6	75.6 ± 4.6	$5800.0^{+6800.0}_{-1500.0}$	500.01	321.332 ± 11.850	-	[1],[3]
ZwCl7160	19666.7 ± 123.7	95.7 ± 9.4	-	35.72	10.399 ± 0.846	-	-,[3]
ZwCl8276	7848.4 ± 281.5	61.6 ± 1.8	-	9.29	1.805 ± 0.220	3.71	-,[3]
4C+55.16	8874060.0 ± 266213.0	1799.3 ± 1230.9	$420.0^{+440.0}_{-160.0}$	71.43	25.605 ± 1.693	-	[1],[3]
A1668	4628.9 ± 141.2	47.8 ± 0.4	-	12.00	2.519 ± 0.284	1.66	-,[6]
A2029	48195.2 ± 1853.3	147.2 ± 24.9	$87.0^{+49.0}_{-4.0}$	0.80	0.075 ± 0.019	-	[1],[6]
A2142	$<439.6 \pm 0.0$	$<15.4 \pm 2.4$	No Cavity	-	-	-	[12],-
A2151	207.4 ± 0.0	10.8 ± 2.2	-	5.80	0.979 ± 0.137	-	-,[6]
A2199	46658.5 ± 1563.1	144.9 ± 24.1	$270.0^{+250.0}_{-60.0}$	3.50	0.508 ± 0.083	-	[1],[6]
A2261	3058.5 ± 0.0	39.2 ± 1.4	-	-	-	-	-,-
A2319	$<157.2 \pm 0.0$	$<9.4 \pm 2.0$	-	10.00	1.987 ± 0.237	-	-,[6]
A2390	220943.0 ± 7770.4	305.7 ± 91.8	No Cavity	44.29	13.754 ± 1.050	-	[12],[7]
A2462	$<279.0 \pm 0.0$	$<12.4 \pm 2.3$	-	5.80	0.979 ± 0.137	-	-,[6]
A2634	102659.0 ± 0.0	211.6 ± 49.2	-	3.70	0.546 ± 0.088	-	-,[6]
A2657	$<80.1 \pm 0.0$	$<6.8 \pm 1.7$	-	0.17	0.010 ± 0.004	-	-,[2]
A2626	2481.6 ± 110.6	35.4 ± 1.8	$10.7^{+6.6}_{-6.6}$	3.30	0.470 ± 0.078	1.66	[5],[6]
A2665	2518.6 ± 93.9	35.7 ± 1.8	-	0.60	0.051 ± 0.014	1.66	-,[6]
A2734	650.8 ± 34.3	18.6 ± 2.5	-	-	-	-	-,-
A3526	7012.5 ± 193.8	58.3 ± 1.3	No Cavity	0.36	0.026 ± 0.008	-	[13],[3]
AWM7	$<14.2 \pm 0.0$	$<3.0 \pm 1.0$	-	0.36	0.026 ± 0.008	-	-,[3]
M87	34071.4 ± 1205.4	124.6 ± 17.6	-	0.79	0.073 ± 0.019	-	-,[3]
RXJ0439.0+0520	85002.4 ± 2991.6	193.3 ± 41.8	-	78.57	28.982 ± 1.862	18.66	-,[3]
RXJ1347.5-1145	216807.0 ± 8654.1	302.9 ± 90.5	No Cavity	214.29	106.805 ± 5.079	-	[12],[3]
ZwCl235	5169.3 ± 165.8	50.4 ± 0.0	-	2.93	0.403 ± 0.069	1.66	-,[7]
ZwCl2089	8975.5 ± 572.9	65.7 ± 2.6	-	71.43	25.605 ± 1.693	270.47	-,[3]

References for cavity power or Hα luminosity – [1] Rafferty et al. (2006), [2] ACCEPT Database Cavagnolo et al. (2009), [3] Edge (2001), [4] Kirkpatrick et al. (2009), [5] Hlavacek-Larrondo (priv. comm, 2014), [6] Salomé and Combes (2003), [7] Crawford et al. (1999), [8] Cavagnolo et al. (2010), [9] Canning et al. (2013), [10] Hlavacek-Larrondo et al. (2013), [11] Pandge et al. (2013), [12] Shin et al. (2016), [13] Panagoulia et al. (2014b), [14] Birzan et al. (2012)

Appendix B

Other Contributions

During my M.Sc. I have had the opportunity to be involved in a few publications: *Mass Distribution in Galaxy Cluster Cores* by Hogan et al. (2016) and *A Mechanism For Stimulating AGN Feedback By Lifting Gas in Massive Galaxies* by McNamara et al. (2016). In both of these publications, my contribution was to use 2MASS K-band (2.17 μm) isophotal magnitudes to estimate the stellar velocity dispersions of central dominant galaxies in clusters. This is an essential parameter for the model fitting used to produce mass profiles of the sample of galaxy clusters in those publications. Furthermore, I was also involved in the analysis of X-ray data including the implementation of wrapper scripts that allowed the data reduction scripts to be executed in parallel computing.